

MODELING OF THE CATHODOLUMINESCENCE PROPERTIES OF THE THIN
FILM PHOSPHORS FOR FIELD EMISSION FLAT PANEL DISPLAYS

By

KYU-GONG CHO

A DISSERTATION PRESENTED TO THE GRADUATE SCHOOL
OF THE UNIVERSITY OF FLORIDA IN PARTIAL FULFILLMENT
OF THE REQUIREMENTS FOR THE DEGREE OF
DOCTOR OF PHILOSOPHY

UNIVERSITY OF FLORIDA

2000

I would like to dedicate this dissertation to my wife,
Mi-Ree, and our lovely daughters, Ha-Young and Ye-Young.

ACKNOWLEDGMENTS

I would like to acknowledge many people who have made this journey possible. I would like to express my grateful thanks to my advisor, Dr. Singh, for his guidance, support, and encouragement of this work over the last four years. Many ideas that he suggested have opened my eyes more widely to various research approaches. I would like thank Dr. Holloway not only for serving as a committee member but also for his guidance throughout numerous discussions. I would like thank Dr. Tanner, Dr. Jones, and Dr. Wachsman for serving as the members of my supervisory committee as well as for their warm guidance and interest through timely discussions of this work.

I specially want to thank Dr. Kumar for his help with pulsed laser deposition and discussions throughout my research. I also thank my colleague, Mr. Chen, who helped me to derive the mathematical expressions for the modeling work. I would also like to thank Mr. Russell and Dr. Wagner, of the Phosphor Technology Center of Excellence (PTCOE) at the Georgia Institute of Technology, for measuring cathodoluminescent efficiency, and Dr. Gao, of the Solid

State Division at Oak Ridge National Laboratory, for the transmission electron microscopy work.

It is a pleasure to thank all the staffs in the Headquarters of the Korean Army and the faculty, staff, and the administration of the Department of Materials Science and Engineering for giving me an opportunity to study in Gainesville, Florida, and all the support during my study.

I would like to acknowledge the friends and coworkers who shared warm friendship and memorable time in this department: Yong-Jin, Keunyoung, Dong-Gu, Jewon, Jin, Jongjin, Keebum, Kang-Nyung, Jongpyo, Kyupil, Hyun, John, Sean, Jenfon, Jim, Don, Valentin, Ali, Uday, Seung-Mahn, Kyo-se, Jaeyoung, Wonseop, Wonseok, Hyungjin, Sanghyun, Anu, Srini, Mike, Hui, Josh, Frank, Nabil, Anupam, and others provided constant support and a wonderful life in Gainesville. Finally, I must express my deepest appreciation to my wonderful wife, Mi-Ree, my lovely daughters, Ha-Young and Ye-Young, my parents, and my brothers and their families for their endless love, support, and encouragement.

This research was supported by an AFOSR Grant F49620-96-1-0026 and through the PTCOE by DARPA Grant No.MDA972-93-1-0030. I would also like to thank the U.S. Department of Energy (Grant No. DE-FG 05-95ER45533) for partial support to this research.

TABLE OF CONTENTS

	<u>page</u>
ACKNOWLEDGMENTS	iii
ABSTRACT	vii
CHAPTERS	
1 INTRODUCTION	1
2 LITERATURE REVIEW	5
Field Emission Display (FED)	5
Cathodoluminescence (CL)	8
Europium-Activated Yttrium Oxide ($Y_2O_3:Eu$)	16
Thin Film Phosphor (TFP)	23
Light Scattering	27
Pulsed Laser Deposition (PLD)	30
3 EXPERIMENTAL APPROACH	50
Target Preparation	51
Substrate Materials	52
TFP Fabrication Using PLD	53
Characterizations	54
X-Ray Diffraction (XRD)	54
Scanning Electron Microscopy (SEM)	55
Atomic Force Microscopy (AFM)	56
Auger Electron Spectroscopy (AES)	57
Transmission Electron Microscopy (TEM)	58
Variable Angle Spectroscopic Ellipsometry (VASE)	59
UV-VIS-NIR Spectrometer (UVNS)	60
Photoluminescence (PL)	60
Cathodoluminescence (CL)	61
4 RESULTS AND DISCUSSION	66
Target and Diamond Buffer Layer	66
$Y_2O_3:Eu$ TFPs on Diamond Buffer Layer	67
Brief Overview of Microstructural Investigations	73

	Optical Properties	78
	Photoluminescence	79
	Cathodoluminescence	80
	Summary	82
5	Modeling	109
	Assumptions for Modeling	111
	Surface Roughness of Film	113
	Intensity Change by an Angle Change	113
	Scattering of Light at Interface	114
	Modeling of Specular Component of Light	118
	Light Propagating in Upward Direction	119
	Light Propagating in Downward Direction	119
	Light Transmitted from Film into Substrate	120
	Light Transmitted Back from Substrate into Film	121
	Summation of Intensities	122
	Integration of Specular Component	124
	Modeling of Diffuse Component of Light	125
	Light Propagating in Upward Direction (Diffuse)	125
	Light Propagating in Downward Direction (Diffuse)	126
	Summation of Intensities (Diffuse)	128
	Integration of Diffuse Component	130
	Summation of Specular and Diffuse	130
	Charge Carrier Diffusion and Concentration	131
	Predicted TFP Properties by Model	134
	Optical Properties	135
	Electron Beam-Solid Interactions	137
	Number of E-H Pairs in TFP	138
	Predicted CL Properties	139
	Predicted and Experimental Results	143
	Summary	145
6	CONCLUSIONS	175
APPENDICES		
A	DERIVATIONS FOR SPECULAR AND DIFFUSE PARTS	179
B	SOLUTIONS FOR CONSTANTS C_1 , C_2 , C_3 , AND C_4	186
C	MODEL CALCULATION FOR A $Y_2O_3:Eu$ TFP ON QUARTZ	187
REFERENCES		195
BIOGRAPHICAL SKETCH		205

Abstract of Dissertation Presented to the Graduate School
of the University of Florida in Partial Fulfillment of the
Requirements for the Degree of Doctor of Philosophy

MODELING OF THE CATHODOLUMINESCENCE PROPERTIES OF THE THIN
FILM PHOSPHORS FOR FIELD EMISSION FLAT PANEL DISPLAYS

By

Kyu-Gong Cho

May 2000

Chairperson: Rajiv K. Singh
Major Department: Materials Science and Engineering

In order to investigate the effects of the film roughness with the fundamental luminance parameters of thin film phosphors, $Y_2O_3:Eu$ films with different thickness and roughness values were deposited on various substrate materials using a pulsed laser deposition technique under a controlled experimental procedure. The best luminous efficiency was observed from the $Y_2O_3:Eu$ films on quartz substrates due to the smaller refractive index and low absorption characteristics of the quartz substrates which produce a larger amount of total internal reflection in the film and low loss of light intensity during the multiple internal reflections. The trapped light inside the film can escape the film more easily due to rougher film surface. The

better epitaxial growth capability of the $Y_2O_3:Eu$ films with the $LaAlO_3$ substrates resulted in higher luminous efficiency in the small surface roughness region. Higher luminous efficiency was observed in reflection mode than in transmission mode due to the contribution of diffusely scattered light at the air-film interface.

A new theoretical model based on the diffraction scattering theory of light, the steady-state diffusion condition of carriers and the Kanaya-Okayama's electron-beam-solid interaction range satisfactorily explains all the experimental results mentioned above. The model also provides solid understandings on the cathodoluminescence properties of the thin film phosphors with the effects of other single or multiple luminance parameters. The parameters encountered for the model are surface roughness, electron-beam-solid interaction, surface recombination rate of carriers, charge carrier diffusion properties, multiple scattering at the interfaces (air-film, film-substrate, and substrate-air), optical properties of the material, film thickness, and substrate type. The model supplies a general solution in both qualitative and quantitative ways to estimate the luminance properties of the thin film phosphors and it can be utilized to optimize the thin film phosphor properties for the application of field emission flat panel displays.

CHAPTER 1 INTRODUCTION

There has been significant interest in the development of thin film phosphors (TFPs) for field emission displays (FEDs). Since the distance between the field emitter tips and the phosphor screen is very small in FEDs, there exist two major concerns using powder phosphors which are debonding and outgassing. Any failure of adhesion may cause debonding of powder particles from the bulk phosphor screen. The free particles debonded from bulk powder layer will block the gates of the field emitter tips. This blocking of emitter tips will eventually cause no light output from certain areas of the screen. Outgassing is another major concern of powder phosphors. The residual gases coming out from the binding materials for powder particles and the relatively porous structure of the powder layer itself will increase the gas pressure of the vacuum sealed device under energetic electron bombardments. Ionization, formation of plasmas, and arcing effects due to these gas phases with the electron beam (e-beam) will be detrimental to the emitter tips and phosphor dots. Therefore, TFPs are believed to be the only solution to solve these problems. However, the

relatively low efficiency of the TFPs has kept them behind the powder phosphors in FEDs so far.

The relatively low brightness of the TFPs compared to powder phosphors, can be significantly enhanced by tailoring the surface roughness of the TFPs using various methodologies including variation in processing conditions [Jon97a,b], modifying TFP's surface [Lee98b, Sch93], and addition of a buffer layer between TFP and the substrate [Cho97a,b]. It has been experimentally shown that the light trapping due to internal reflection from a smooth surface is reduced as the surface becomes progressively rougher [Cho99, Jon97a, Lee98b, Sch93]. Although this phenomenon is qualitatively understood, there has been a lack of detailed analysis of the scattering phenomenon which affects the light emission from TFPs. Factors which affect the cathodoluminescence (CL) brightness of TFPs are thickness, interface, microstructure, roughness, substrate, and e-beam-solid interaction. In general, these factors are correlated and cannot be varied independently, thus making it difficult to quantitatively interpret the solutions. Furthermore, as the wavelength of the surface roughness becomes smaller or has the same dimensions of the wavelength of the emitted radiation, classical theories based on rectilinear propagation of the light cannot be used without gross simplifications. Some simplified models have been suggested

to predict the brightness of the TFPs as a function of the effect of bulk and surface structure [Cho99, Jon99, Lee98b, Sch93], however they do not take into account complex surface scattering-based effects.

In order to overcome the deficiencies of the earlier work, a new model which incorporates diffraction-related multiple light scattering at the different optical interfaces including absorptions and reflections by the materials, TFPs on various substrates with different film thickness and roughness values as well as e-beam-TFP interactions, is in great demand. Therefore, the objective of this research is to understand the effects of the fundamental parameters controlling the luminance properties of TFPs with a computer-based theoretical model developed for this study. This understanding and the development of a predictable theoretical model is expected to eventually lead to fabricate TFPs for FEDs with optimum CL properties.

In this dissertation, chapter 2 presents an overview of the literature survey on the related subjects to this research. This includes a brief review of FEDs, an understanding of CL, an outline of $Y_2O_3:Eu$ phosphor, critical issues in TFP technology, and diffraction-based light scattering at the rough surfaces. Pulsed laser deposition (PLD) is also briefly introduced. Chapter 3 discusses the experimental procedures and characterization

techniques that were used for investigating process parameters of $\text{Y}_2\text{O}_3:\text{Eu}$ TFPs in PLD and for understanding the phosphor properties. Chapter 4 presents and discusses the results of the experiments including surface chemistry of targets and films, microstructural, optical properties, photoluminescent (PL), and CL studies. Chapter 5 explains the modeling procedures of the fundamental parameters controlling the luminance of TFPs followed by comparisons between the experimental results and the theoretical model. Finally, all the conclusions of the study are summarized in chapter 6.

CHAPTER 2 LITERATURE REVIEW

Field Emission Display (FED)

FED is one of the emitter-based direct view flat panel displays (FPDs) which projects pictures using CL as summarized in the electronic information displays shown in Figure 2.1. Since the FED offers a thinner, compared to thin film transistor (TFT) LCD, wider viewing angle, more portable package, wider range of operating temperature, lower power consumption, much faster response speed, higher resolution, and video capability, the FED appears to be more hopeful and promising technology of the FPDs for the next millennium [She98, Kor99, Off95].

A detailed cross-sectional representation and array of a FED are illustrated in Figure 2.2. The FED consists of an electrically addressable matrix of field emitters which act as cold cathodes in cathode-ray tubes (CRTs), opposing a phosphor-coated transparent plate where the volume of space between the emitters and the phosphor-coated plate is evacuated and separated by spacers [Mor98, Off95, Smi98].

Field emission occurs when an externally applied electric field at the material surface thins the potential barrier to the point where electron tunneling occurs [Smi98]. Electrons emitted from the addressed emitter tips are accelerated towards the phosphor-coated transparent plate which serves as an anode and has a positive voltage relative to the emitter arrays [Chi94, Kor99, Kuo97, Mor98]. The bombarding electrons (cathode rays) arriving at the phosphor surface cause CL through the same mechanism that is observed in the conventional CRTs and serve as the emissive light source seen by a viewer [She98].

The primary interests of the FED technology include the emitter tips, phosphors, and electronic packing [Kim98]. The Spindt type structure of the emitter tips is well known to be the most stable structure for the emission source to date, even though other strong candidates such as diamond [Wei98], nanotube [Rin95, Uem98], surface conduction electron source [Oku98], and modified Spindt [Kim99] are under development. The emitter tips are arrayed as many as $10^7/\text{cm}^2$ which allow thousands of emitters to excite one pixel, providing a large amount of redundancy and preventing single point failure [Pet95, She98, Tan85].

Low-voltage operation is desirable for portable FEDs due to its relatively low power consumption and easy switching method on the anode, whereas high voltage operation requires

thicker spacers to remove the arcing effects between the cathode and anode and also have difficulty in anode switching [Cou96, Kim97, Vec99]. However, currently available phosphors do not have high enough CL efficiencies at low voltages [She98]. The use of less efficient phosphors at low voltages requires high current operation which increases phosphor degradation rate as well as the number of tips required, which results in additional switching capacitances of the device as well as handling of high current-capable drivers [Vec99].

The sulfur-based phosphors such as ZnS:Ag , ZnS:Cu , and $\text{Y}_2\text{O}_2\text{S:Eu}$ used in CRTs, have been applied for FEDs since they exhibit the highest luminous efficiencies among all the currently available commercial phosphors. However, the CL brightness of these sulfur-based phosphors are more sensitive to gas pressure and gas ambient, which eventually results in faster CL degradation after initial gains of high luminous efficiency. Since, unlike the CRTs, the field emitter tips are very closely spaced to the phosphor screen in FEDs, the sulfur out-products evaporated from the sulfur-based phosphors will also accelerate the degradation of the field emitter tips [Hol99, She98]. Therefore, relatively stable oxide- and silicate-based red, green, and blue (RGB) phosphors are under strong development to enhance low voltage performance for FEDs [Hol99]. Recently, there is

another trend for many FEDs to be designed for operation in the 5-10 kV range [She98].

The packing of FEDs includes frit seals, spacers to maintain space between anode and cathode plates, and getters. The existence of residual gases inside the space because of an insufficient exhaustion may result in critical failure on the reliability of the device. To ensure the reliability of FED devices sealed in 10^{-6} to 10^{-9} Torr vacuum, getters are inevitably employed throughout the inside of the device to maintain the panel pressure as low as possible by capturing any outgassed contaminants which would otherwise degrade either emitter tips or phosphor dots [Kim99, Kor99, Smi98]. Therefore, the packing of the FED is a more difficult process compared to that of other FPDs.

Cathodoluminescence (CL)

CL is an important technological phenomenon that is the most widely used in modern CRT-based instruments, electron microscopes, and FEDs. CL is defined as the emission of light, with a possible afterglow, as a result of e-beam-solid interaction [Wal88, Yac90].

Figures 2.3(a)-(b) illustrate the changes of interaction volume from A to C with increase in electron energy from several keV to tens of keV [Yam98], and

qualitatively the generation of CL resulting from the interaction of an e-beam with a solid [Mar88], respectively. When an incident e-beam enters a solid with the original probe diameter (d), the charges in the host lattice redistribute to oppose the sudden change in electric field, and many secondary electrons are created in cascade throughout the volume as each incident electron is inelastically scattered within the host [Pin64]. Only the secondary electrons created very near the surface in Figure 2.3(b) are able to escape from the surface. Further interactions with electron energies above 1 keV produce characteristic X-rays over the entire region until electrons are slowed down by Coulombic interaction with the host atoms [Myh98]. This deceleration results in bremsstrahlung (continuum radiation) designated by D_1 . These cumulative interactions of multiple scattering and subsequent diffusion with zigzag trajectories broaden the original probe diameter and produce a pear-shaped CL generation volume where the electrons retain greater than a few eV energy and represented by the depth (L) and the diameter (D_2) [Mar88]. The depth (L) of this CL generation volume includes the depth of the charge carrier diffusion, in addition to the incident e-beam-solid interaction range (R) which can be estimated using the Kanaya-Okayama's equation,

$$R = \frac{27.6 M E_0^{1.67}}{Z^{0.89} \rho} \text{ } (\mu\text{m}) \quad (2.1)$$

where M , E_0 , Z , and ρ represent atomic weight of solid (g/mol), incident electron energy (keV), atomic number of solid, and density of solid (g/cm³), respectively [Gol92, Yac90]. The secondary cascade is one of the main difference between CL and PL. PL primarily excites the activator, whereas CL excites with gain, the host as well as the activator. Gain is possible in CL because a single electron can generate, via avalanche process (or impact ionization), multiple secondary electrons which can correspondingly produce photons [Yac90].

CL is also a part of the diffusion process of the electrons in the phosphor since electrons diffuse further into the matrix than the interaction range creating new e-h pairs. The diffusivity (or diffusion coefficient) of an electron is defined as [Ben91, Sze81]

$$D = \frac{kT\mu_e}{e} \quad (2.2)$$

where k is the Boltzmann's constant, T is the temperature in Kelvin, μ_e is the electron mobility, and e is electron charge. The kT/e is 0.026 V at room temperature [May90], and the μ_e is defined as [Sze81]

$$\mu_e = \frac{1}{Ne\rho} \quad (2.3)$$

where N is the number of e-h pairs and ρ is the resistivity of the phosphor material. Therefore, the electron diffusivity is inversely proportional to the number of e-h pairs and resistivity of the phosphor material.

Under the steady state condition, the number of photons emitted is equal to the number of carriers released by the incident electrons that recombine. Then, a simple diffusion equation can be applied to determine the carrier concentrations in a phosphor, as defined as [Yoo97]

$$D \frac{d^2}{dx^2} N - \frac{N}{\tau} + G = 0 \quad (2.4)$$

where x is the depth from surface, τ is the life time of the radiative recombination, and G is the generation rate of the e-h pairs by e-beam. The generation rate, G , is defined as [Yoo97]

$$G = \frac{i_0 V_0}{\Delta E R} \quad (2.5)$$

where i_0 is current density, V_0 is accelerating voltage, ΔE is average work done to create an e-h pair, and R is the interaction range of e-beam in the host matrix as defined in Equation (2.1). The number of e-h pairs (N) created in the phosphor can be obtained by solving Equation (2.4).

Therefore, the intensity (or brightness) of CL generated at point x , $I_0(x)$ is defined as [Yoo97]

$$I_0(x) = \frac{E_e}{t} \cdot N(x). \quad (2.6)$$

Luminescence efficiency is defined as the ratio of the energy (quanta) required to excite a phosphor to the energy (quanta) emitted from the sample [Yos98]. CL efficiency is then measured and obtained in terms of either photometric (lumens/watt) or radiometric units (watts/watt) by exciting the phosphor with an e-beam of a given acceleration voltage and a given current density. If the light output is measured in the photometric way, the luminous efficiency which is the ratio of luminance to the input power is given by,

$$efficiency = 100\pi \frac{L_0}{jV} (lumens / watt) \quad (2.7)$$

where L_0 is the light output in candelas/m², j is the current density in mA/cm², and V is the acceleration voltage in Volts [Jac96, She98]. The factor of π is included since the emission of the phosphor is Lambertian [She98]. Luminance is a measure of the total energy output of a light source emitted in the visible region of the spectrum [Ras96].

The luminous efficiency is used to describe the efficiency of phosphors excited by sources that produce e-h pairs in the host lattice [She98]. The luminous efficiency can be divided into intrinsic and extrinsic (or screen) efficiencies. The intrinsic efficiency concerns only the efficiency of the phosphor itself, while the extrinsic efficiency matters the efficiency of the whole screen [Pet95, She98]. The intrinsic efficiency known to be independent of j and V for high voltages (10-30kV) but dependent on low voltages (0.5-4kV), whereas the screen efficiency varies with phosphor particle size and shape, screen thickness, and presence of binders [Jac96, She98].

Most phosphors show a significant decrease in their CL efficiency at electron energies below 5 kV [Ben91, Oza90]. This decrease in CL efficiency is primarily induced by surface recombination and surface charging. Surface recombination is nonradiative recombination of e-h pairs at the surface of phosphor [Ben91], and it is expressed by the appropriate boundary condition for diffusion to the surface [Yac90],

$$[S \cdot N(x)]_{x=0} = D \left(\frac{dN}{dx} \right)_{x=0} \quad (2.8)$$

where S is the surface recombination velocity (cm/sec). Nonconductive nature of the phosphor layer causes a

cumulation of incoming electrons near surface region and this charge cloud forms a negatively charged local electric field near the surface [Has90]. This negatively charged electric field accelerates the excited electrons to slide down toward the surface through the bended band structure and thus increases the surface recombination rate of the e-h pairs generated in the phosphor, reducing the number of e-h pairs of radiative recombination [Has90, Yam98]. The negatively charged surface layer is known as a dead layer first named by Fan [Fan40]. The dead layer lowers the electron impact energy, which restricts most of the e-beam-induced excitation to the near surface region and eventually prevents the phosphor from retaining their CL properties at the initial stage as well as after prolonged e-beam exposure [Sea97, Yac90, Yam98]. To minimize the effects of surface dead layer, an aluminizing technique is employed in CRTs. A thickness of 100 nm Al film is coated on the phosphor to ensure sufficient electrical conductivity and optical reflectivity [Yam98].

The decrease of CL efficiency is also caused by phosphor degradation after prolonged exposure to the energetic e-beams. The physical phenomena that cause degradation are related to surface volatilization and chemical transformations induced by residual gases in vacuum and e-beam dissociation of these gases [Swa96]. The

mechanisms for CL degradation have been studied in various phosphor systems. One mechanism of CL degradation was reported early in which a high degradation rate was believed to be attributed to both the creation of new non-radiative recombination sites under prolonged electron bombardment and deactivation of luminescent centers by charge compensation (Ce^{3+} to Ce^{2+}) in the $(\text{CaO})_2\text{MgO}(\text{SiO}_2)_2:\text{Ce}^{3+}$ phosphor system [Pfa61]. Other mechanisms of phosphor degradation observed later are thickening of dead layer on the phosphor surface due to increased oxygen deficient layer in $\text{ZnSiO}_4:\text{Mn}^{2+}$, changes in relative radiant efficiency with increased saturation caused by decreased energy flow to the activator in $\text{Y}_2\text{SiO}_5:\text{Ce}^{3+}$, and a decreased photon escape probability induced by color centers in the aluminate host in $\text{Sr}_2\text{Al}_6\text{O}_{11}:\text{Eu}^{2+}$ [Kla87]. For $\text{LaOBr}:\text{Tb}^{3+}$ phosphor, increases in optical absorption and ion desorption (bromine) was reported as a major degradation mechanism over 400 C/cm^2 coulomb load with 1~4 keV energy [Ron94]. For sulfur-based phosphors ($\text{Y}_2\text{O}_2\text{S}:\text{Eu}$, $\text{ZnS}:\text{Ag,Cl}$, or $\text{ZnS}:\text{Al,Au,Cu}$), the degradation was commonly attributed to the depletion of sulfur converting the surface layer to a non-activated Y_2O_3 or ZnO layer [Tro96, Swa99].

In brief, the possible mechanisms for CL degradation in phosphors can be summarized by introduction or diffusion of defects in crystals, increases in optical absorption, and

the desorption of surface species which converts the surface to a non-luminescent layer [Tro97]. In order for phosphors to be useful in FEDs, a method of reducing the degradation rate must be introduced and utilized. Coatings on phosphor surface is recently focused to improve thermal dissipation, electrical conductivity, and less outgassing without detrimental effects on efficiency and chromaticity. Wet chemical surface coatings on powder CRT phosphors have been shown to be useful to enhance low voltage efficiency with increased electrical conductivity [Kom96]. Aluminum coating on ZnO phosphor reduced degradation rate significantly over the bare ZnO phosphor due to increased thermal and electrical conductivity [Pfa61]. More recently, Fitz-Gerald et al. [Fit98] reduced the CL degradation rate of the $\text{Y}_2\text{O}_3\text{:Eu}$ powder phosphor with TaSi_2 coatings using PLD from 52 to 15% without reducing efficiency. The TaSi_2 coating prevented chemical transformation of the oxysulfide surface into an oxide layer and reduced surface charging effects.

Europium-Activated Yttrium Oxide ($\text{Y}_2\text{O}_3\text{:Eu}$)

Rare earth-activated oxide phosphors are potential candidates in display technology because of their excellent light output and color rendering capabilities [Duc94, Bla94]. The chemical and thermal stability of these

phosphors combined with relatively high brightness, make them attractive for FEDs. Among the rare earth oxide phosphors, $Y_2O_3:Eu$ is a highly attractive red phosphor material for FEDs. In the $Y_2O_3:Eu$ phosphor system, Eu^{3+} acts as an activator while Y_2O_3 acts as a host matrix. The concentration of europium in Y_2O_3 is considered as an important parameter for red color emission since the ${}^5D_0-{}^7F_2$ transition is likely to occur for ~3 mole % of europium in Y_2O_3 [Bla94, Kam98, Oza90]. When the concentration of the europium falls down to below 3 mole %, the energy stored by the impurities also decreases, resulting in reducing the probability of radiative emission. When the concentration of europium is greater than the appropriate amount, optical excitation is trapped at the defects or impurities, known as concentration quenching [Has90]. In this case, probability of non-radiative relaxation increases [Oza90, Bla94].

Figure 2.4(a) shows the unit cell structure of the pure Y_2O_3 host matrix representing a cubic structure with eight incomplete fluorite formula units constituted with a total of 80 atoms (yttrium: 32 and oxygen: 48) with a lattice constant of 10.60 Å [Daa94, Fuk89, Tro91, Pat65]. The incompleteness of the fluorite structure is caused by a removal of a quarter of oxygen atoms in order to maintain the charge neutrality followed by a rearrangement of the remaining six oxygen atoms from the cube corners [Oni90,

Sch92]. As a result, each yttrium atom is surrounded by only six oxygen neighbors forming two different types of distorted octahedral site (S_6 and C_2 sites in Figure 2.4(b), respectively), while each cation is surrounded by eight anions located at the eight cube corners in an ideal fluorite structure [And70, For69, Jol90]. Therefore, eight yttrium atoms (25%) occupy the S_6 sites and the other 24 atoms (75%) occupy the C_2 sites in the Y_2O_3 unit cell structure [Tro91].

$Y_2O_3:Eu$ phosphor is known to show the intra-atomic transition within europium atom in Y_2O_3 host lattice denoted by 5 in Figure 2.5. The Eu^{3+} ion occupying the Y^{3+} site creates the charge transfer band (CTB) with neighboring O^{2-} ions [Bla94, Duc94, Oza90, Pap85]. Eu^{3+} ($4f^6$) tends to capture an electron from oxygen $2p$ state in order to go toward the highly stable $4f^7$ (half-full) configuration and thus creating a lower energy CTB than the Y_2O_3 band edge [Rop67, Wes90]. The created CTB is responsible for the intense absorption at wavelengths around 265 nm, as illustrated in Figure 2.6 [Bla94, Bor63, Oza90]. The excitation of Eu^{3+} takes place from the bottom of the 7F_0 curve until it crosses the CTB. An incident electron beam or short wave ultra-violet (UV) light radiation is suitably used to excite an electron to the CTB and the excitation

process to the CTB is considered to be more efficient than energy transfer from the host to the activators [Mae92]. Excitation to the host lattice is also possible when the excitation energy is greater than the band gap of the host lattice. For this case, electron migration to the CTB is known to occur. Figure 2.7 shows the two excitation peaks which result from the strong absorption of electrons by the host lattice and the CTB [Oza90]. Relaxation along the CTB curve to 5D_3 states and radiative emission downward to 7F_3 states are then favorably followed at europium ions [Bla94, Duc94, Her70, Oza90, Pap85, Rop67]. This optical transition is more likely to occur in the C_2 site rather than in the S_6 site, since the ion in the S_6 site has low absorption strength and easy transfer of the excited electron to the C_2 site due to its more stable inversion symmetry as shown earlier in Figure 2.4(b). Therefore, only certain magnetic dipole transitions are allowed in the S_6 site, while an electric dipole transition prefers the C_2 site due to its no center of inversion symmetry [Bri89, Cha64, Dex79]. In other words, the magnetic dipole transitions occur preferentially at the S_6 sites while the electric dipole transitions is more likely at the C_2 sites. Therefore, the emission peak from the S_6 site is considerably weaker than the C_2 site in the spectra because of the fact that the S_6 site is three

times less in number, in addition to, its low absorption strength and easy transfer of the excited electron to the C_2 site [Dex79].

$Y_2O_3:Eu$ phosphor emits highly saturated red light mostly from the C_2 sites due to its preferential $^5D_0-^7F_2$ transition at a wavelength of 611 nm within the $4f^6$ configuration of the europium shielded by the filled $5s^2$ and $5p^6$ outer shells [Bla94, Jon97a, Mar88]. Shown in Figure 2.8 is the proposed model of the CL process of the $Y_2O_3:Eu$ phosphor [Oza90]. When an incident electron beam strikes the host lattice, Y^{3+} converts to Y^{2+} . The Y^{2+} now releases the electron to the next yttrium, converting back to Y^{3+} . The electron migrates along the Y^{3+} until it reaches an activator, Eu^{3+} . The Eu^{3+} is now converted to Eu^{2+} due to having trapped the electron from Y^{3+} . This results in a negatively charged local field. The hole which is transported to the O^{2-} , converting it to O^{1-} , is attracted to this local negative field. Once the hole is captured by the Eu^{2+} , the Eu^{2+} goes into the excited Eu^{3+} state. Then it relaxes and returns to the ground state of Eu^{3+} emitting visible light [Oza90].

A typical CL spectrum recorded from the $Y_2O_3:Eu$ phosphor is shown in Figure 2.9 [Cho97b]. The set of three closely spaced peaks at 587, 593 and 596 nm wavelengths is

associated with magnetic dipole transitions ($^5D_0-^7F_1$) which is insensitive to the site symmetry, whereas the peaks at 579, 610-630 and 680-710 nm are associated with electric dipole transitions ($^5D_0-^7F_0$, $^5D_0-^7F_2$, and $^5D_0-^7F_4$, respectively) preferred by lack of inversion symmetry [For69, Rie70, Tan98]. The origin of these transitions can be understood by considering the energy level diagrams for an Eu^{3+} ion in a Y_2O_3 lattice, as schematically shown in Figure 2.10. The 7F_J ground states and 5D_J first excited states arise from different configurations of the $4f^6$ electrons. Due to spin-orbit interactions, the 7F and 5D states split into the individual J levels. Each degenerate J level ($J > 0$) can be further split by interactions with the crystal field. However, due to strong shielding of $4f$ electrons of an Eu^{3+} ion by the $5s$ and $5p$ orbitals, the crystal field splittings are very weak [Cha64]. The preference from the two different transitions (electric dipole or magnetic dipole) is determined by the selection rules. According to the selection rules, the allowed electric dipole transitions in system are those for which $\Delta J \leq 6$. The transitions arising from magnetic dipole transitions are those for which $\Delta J = 0, 1$ but the transition $0 \leftrightarrow 0$ is forbidden. Based on these selection rules the nature of transitions taking place are listed in Table 2.1 [Kum99a], and Table 2.2 [Pol93] shows

the electronic configurations and spectroscopic notations of selected rare earth elements in ground state as a reference.

Table 2.1. Nature of transitions occurred in $Y_2O_3:Eu$ phosphor.

Regime	Transition (from \rightarrow to)	ΔJ	Nature of transition
533 - 545 nm	$^5D_1 \rightarrow ^7F_1$	0	Magnetic dipole
579 nm	$^5D_0 \rightarrow ^7F_0$	0 \leftrightarrow 0	Electric dipole
587 - 596 nm	$^5D_0 \rightarrow ^7F_1$	1	Magnetic dipole
610 - 630 nm	$^5D_0 \rightarrow ^7F_2$	2	Electric dipole
650 - 670 nm	$^5D_0 \rightarrow ^7F_3$	3	Electric dipole
680 - 710 nm	$^5D_0 \rightarrow ^7F_4$	4	Electric dipole

Table 2.2. Electronic configurations and spectroscopic notations of selected rare earth elements in ground state.

Atom #	Ion	4f ($\ell=3$) # of $\bar{e}s$	m_ℓ	S	L	J	$^{2S+1}L_J$
			+3+2+1 0-1-2-3	Σs	Σm_ℓ	$\Sigma (L \mp S)$	
57	La ³⁺	(Xe) 4f ⁰		0	0	0	¹ S ₀
58	Ce ³⁺	(Xe) 4f ¹	\uparrow	1/2	3	5/2	² F _{5/2}
63	Eu ³⁺	(Xe) 4f ⁶	$\uparrow \uparrow \uparrow \uparrow \uparrow \uparrow$	3	3	0	⁷ F ₀
64	Gd ³⁺	(Xe) 4f ⁷	$\uparrow \uparrow \uparrow \uparrow \uparrow \uparrow \uparrow$	7/2	0	7/2	⁸ S _{7/2}
65	Tb ³⁺	(Xe) 4f ⁸	$\uparrow \downarrow \uparrow \uparrow \uparrow \uparrow \uparrow \uparrow$	3	3	6	⁷ F ₆
68	Er ³⁺	(Xe) 4f ¹¹	$\uparrow \downarrow \uparrow \downarrow \uparrow \downarrow \uparrow \downarrow \uparrow \uparrow \uparrow \uparrow$	3/2	6	15/2	⁴ I _{15/2}
71	Lu ³⁺	(Xe) 4f ¹⁴	$\uparrow \downarrow \uparrow \downarrow \uparrow \downarrow \uparrow \downarrow \uparrow \downarrow \uparrow \downarrow \uparrow \uparrow$	0	0	0	¹ S ₀

In Table 2.2, ℓ is orbital quantum number ($s=0$, $p=1$, $d=2$, $f=3$, $g=4$, $h=5$, $i=6$, ...), s is spin quantum number ($\uparrow: +1/2$, $\downarrow: -1/2$), m_ℓ is magnetic quantum number (integers from $-\ell$ to $+\ell$), S is spin angular momentum (Σs), L is orbital angular

momentum (Σm_l : $S=0$, $P=1$, $D=2$, $F=3$, $G=4$, $H=5$, $I=6$, $K=7$, $L=8$, ...), J is total angular momentum quantum number [$\Sigma(L+S)$: $J=L-S$ when the 4f-shell is less than half-full, $J=L+S$ when the 4f-shell is more than half-full), and $^{2S+1}L_J$ is spectroscopic notation of the ground state. Therefore, the excited state of Eu^{3+} (5D_0) is expected to be $S=2$, $L=2$, and $J=0$ with m_l configuration of $\uparrow\downarrow$, \uparrow , \uparrow , \uparrow , \uparrow from $+3$, $+2$, $+1$, 0 , -1 , respectively.

Thin Film Phosphor (TFP)

TFPs have been a strong candidate in the development of FEDs to date. TFPs have several advantages over powders due to their higher lateral resolution with smaller grains, better thermal stability, reduced outgassing, and better adhesion to the solid surface [Has90, Hir97]. If the amount of the gaseous phases evaporated from the phosphor material are significant, the degradation of the field emitter tips will be accelerated due to their (evaporated materials) chemically aggressive reaction with the tip material since the distance between field emitter tips and phosphor screen is very close in FEDs. Debonding of powder particles from the bulk phosphor screen is also another major concern in the powder-based phosphors. If a failure of bonding occurs among the particles in a small part of the bulk powder

phosphor screen, the debonded particles from the bulk screen will block the gates of the field emitter tips. This blocking of the field emitter tips, in conjunction with the phosphor-lost area in the bulk layer, will eventually cause no light output from a certain area of the screen.

Therefore, a screen of phosphor in a thin film form with less outgassing is preferred in the FED applications.

However, the biggest hindrance in the application of TFPs is their low brightness and efficiency in comparison to those of bulk powder phosphors. Their lower brightness and efficiency are associated with (i) the internal reflection (or light piping) of the emitted light which channels out along the transverse axes under the film surface instead of vertical emission from the surface, and (ii) inferior crystallinity due to lower processing temperature (firing is carried out over 1300°C for several hours to make $Y_2O_3:Eu$ powder phosphor, whereas thin film phosphors are usually synthesized below 900°C [Cho98c, Hir97, Kam98]). Figure 2.11 shows how internal reflection affects differently on powder and thin film phosphors [Jon99, Ura80]. The generated light eventually escapes through multiple internal reflections in the powder phosphor while only the light at $\theta < \theta_c$ escapes the surface and all other rays are internally reflected in the TFP.

A very useful factorization of the efficiency (η) of TFP related to the internal reflection was suggested by Mach and Muller [Mac84], and reviewed by Theis and Wengert [The85]:

$$\eta = \eta_{exc} \cdot \eta_{lum} \cdot \eta_{opt} \quad (2.9)$$

where η_{exc} is the ratio of emitted centers to transferred electrons, η_{lum} is the ratio of radiatively decaying centers to excited centers, and η_{opt} is the ratio of emitted photons through surface to generated photons. η_{opt} is also factorized into

$$\eta_{opt} = \eta_A \cdot \eta_{Fr} \cdot \eta_{CAL} \quad (2.10)$$

where η_A is absorption loss, η_{Fr} is Fresnel loss defined as

$$\eta_{Fr} = \frac{4}{2 + \frac{n_2}{n_1} + \frac{n_1}{n_2}} \quad (2.11)$$

where n_1 is the refractive index of air and n_2 is that of phosphor, and η_{CAL} is critical angle loss (or internal reflection loss) defined as

$$\eta_{CAL} = \left(\frac{n_1}{n_2} \right)^2. \quad (2.12)$$

Accordingly the internal reflection loss is a major contributor to reduced efficiency of TFPs. Figure 2.12 shows that escape cones and photon trajectories inside the material for an ideal flat surface and a rough surface [Lee98b]. All the light emitted outside the escape cone (or cone of emission) will be trapped and eventually absorbed by the material for the former case in Figure 2.12(a), but some of the light can escape the material through the patterned surface for the latter case in Figure 2.12(b). Figure 2.12(c) also explains that a simple geometric approximation which estimates that the fraction of emitted light (F) is only 7 % for $Y_2O_3:Eu$ with $n=1.93$ at 611 nm and $\theta_c=31.2^\circ$ according to Carr [Car66]:

$$F = 0.5(1 - \cos\theta_c) = \frac{1}{4n^2}. \quad (2.13)$$

Therefore, introducing methodologies to reduce internal reflection is critical for application of the TFPs.

Recent investigations have shown that one method to increase the brightness of TFPs is to increase the surface roughness of TFPs which is accomplished by changing the processing conditions [Cho97a, Jon97a], modifying the substrate surface [Cho99], patterning the TFP's surface [Sch93, Lee98b], or adding a rough buffer layer [Cho97a,b, Cho98a]. Other ways to enhance the brightness of TFPs have

been post-deposition annealing [Hir97, Jon97b], and control of the backfilling gas pressure during deposition [Jon97a,b] and post-deposition cooling [Cho98c] in PLD. In fact, Schnitzer et al.[Sch93] improved external efficiency of phosphor from 9 % to more than 30 % with a textured thin film surface, as shown in Figure 2.13.

Light Scattering

When propagating light scatters at the interface formed by two different optical media with a RMS roughness (σ), the light is divided into four different components such as specular reflection (R_s) and transmittance (T_s), and diffuse reflection (R_d) and transmittance (T_d) [Roo94]. If the dimensions of the facets of the crystallites are large compared with the wavelength of light (λ), the reflectance of a surface in a given direction is determined entirely by geometrical optics and is only a function of the inclinations of the facets [Ben61]. As the λ becomes longer, diffraction effects become important, and the reflectance is a function of both the inclination and the size of the facets. As the dimensions of the facets become very small compared with λ , the reflectance of the surface is determined almost entirely by diffraction effects [Ben61,

Top79]. The σ is expected to be the only important parameter [Ben61].

With the assumption that σ is small as compared with λ , Bennett and Porteus [Ben61] derived the expressions for R_s and R_d at normal incidence as

$$R_s = R_0 \exp \left[-\frac{(4\pi\sigma)^2}{\lambda^2} \right] \quad (2.14)$$

$$R_d = R_0 \left[\frac{(4\pi\sigma)^2}{\lambda^2} \right] \quad (2.15)$$

where R_0 is the specular reflection of a perfectly smooth surface. These equations have been very useful for other light scattering related work at normal incidence by Hu and Gordon [Hu 92] for ZnO thin films, Duparre [Dup95] for TiO₂ thin film, Roos and Ronnow [Roo94] for various dielectric films on dielectric substrates, and Sho et al. [Sho98] for GaN films on GaAs substrate. For a single scattering measurement, around 5% of T_d was observed at 28 nm RMS by Hu and Gordon [Hu 92]. However, the latter two authors (Roos and Ronnow, and Sho et al.) used modified expressions by introducing the refractive indices of the materials (n_i and n_{i-1}) as

$$R_{di} = R_{0i} \left[1 - \exp \left[-\left(\frac{4\pi n_i \sigma_i}{\lambda} \right)^2 \right] \right] \quad (2.16)$$

$$T_{di} = T_{0i} \left[1 - \exp \left[- \left(\frac{4\pi(n_{i-1} - n_i)\sigma_i}{\lambda} \right)^2 \right] \right] \quad (2.17)$$

where i denotes the interface being 1 (air-film) or 2 (film-substrate).

When light travels with a random angle (not normal incidence), more general expressions made by Beckmann et al. [Bec63] and reviewed by Toporetz [Top79] for the intensities of the specularly (I_s) and diffusely (I_d) scattered light:

$$I_s = \rho' I_0 \exp \left[- \left(\frac{kh^2}{\lambda^2} \cos^2 \theta \right) \right] \quad (2.18)$$

$$I_d = \rho I_0 \left(\frac{\pi^2 h^2}{\lambda^2} \cos^2 \theta \right) \quad (2.19)$$

where ρ' and ρ are reflection-related coefficients, I_0 is the intensity of the incident light, k is a constant being around $9.8 \pi^2$, h is the roughness height being around 4σ , and θ is the incident angle of the incoming light with respect to normal.

Pulsed Laser Deposition (PLD)

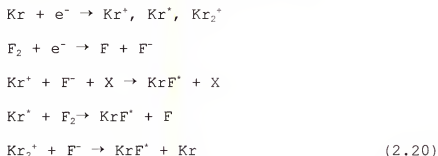
A variety of growth techniques such as evaporation, spray pyrolysis, sputtering, metal organic chemical vapor deposition (MOCVD), molecular beam epitaxy (MBE), metal organic molecular beam epitaxy (MOMBE), and PLD, are employed for the fabrication of thin films. PLD is recognized as one of the most convenient techniques to fabricate multicomponent oxide thin films and multilayered structures because it is a conceptually and experimentally simple but highly versatile technique for them. PLD offers numerous advantages for the growth of thin films of oxides and other chemically complex materials, including congruent (stoichiometric) transfer of material, low contamination level, high deposition rate, non-equilibrium processing, growth from an energetic beam, reactive deposition, simplicity for the growth of multilayered structures, atomically sharp step coverage and thickness control [Low96, Sin98]. These advantages have made the PLD one of the most popular methods to fabricate thin films for various applications.

PLD was first used more than three decades ago after the pulsed ruby laser was invented [Smi65]. However, PLD has been experimentally developed and widely applied for thin film growth as one of the most convenient and efficient

techniques after it was shown that high quality high-temperature (high- T_c) superconducting thin films could be synthesized in a low pressure oxygen ambient without any further post-deposition processes [Dij87, Low96, Sin98]. This discovery has opened, invigorated, and enriched the growth fields of oxide-based ceramics and other complex material systems with a wide variety of properties [Low96]. The complex thin films grown by PLD with high quality includes high- T_c superconductors [Sin98], dielectrics [Sri99], colossal magnetoresistant films (CMR) [Pie98], diamond-like carbons [Chr94], hard coatings [Lee98a], ferroelectrics [Chr94], compound semiconductors [Chr94], and luminescent thin films [Cho97a,b, Cho98a,b,c, Cho99, Gao99, Jon97a,b, Jon99].

KrF is the most popular excimer (excited dimer) laser in laser research since it shows the highest gain among the electrically discharged pumped excimer lasers which are the gas lasers that emit powerful UV pulses lasting from 10 to 50 nanoseconds [Gre94, Low96]. The UV wavelengths have the highest absorption and lowest reflectivity for most materials. The usual active medium is a mixture of gases of a rare gas (Kr, Ar, or Xe) and a halogen (F_2) which combine to form a short-lived rare-gas halide molecules through avalanche electric discharge excitation [Hec92]. Once the excimer is formed, it decays via spontaneous emission and

collisional deactivation processes [Hec92]. KrF laser system typically produces 248 nm wavelength and consists of ~3.5% Kr and ~0.1% F with neon and/or helium as buffer gases to mediate energy transfer with total gas pressure of ~3.6 atm. Some important reactions for the KrF system are:



the asterisk(*) represents an electronically excited state of the species and X as a buffer gas (He, Ne) [Gre94].

PLD uses a high power pulsed laser as an energy source to induce the flash evaporation (or ablation) of a very small segment of a solid or liquid target [Bou99]. When a rotating target material is hit by an UV pulsed laser beam focused with 1~5 J/cm² energy density, several physical events occur: rapid heating and vaporization of the segment; increased absorption by the vapor until breakdown occurs to form a dense plasma (or plume); and absorption of the remainder of the laser pulse to heat and accelerate the plasma which contains various species such as neutral atoms, ions, molecules, and energetic electrons, in both excited and ground states [Low96]. The species undergo collisions in the highly dense region near the target surface (Knudsen

layer, typically a few hundred micrometers thick) to create a highly directional energetic plume perpendicular to the target surface with initial velocities greater than 10^6 cm/s [Low96]. If PLD is performed in a low oxygen pressure environment, oxide molecules are also formed in the expanding plume. In this case, the plume expansion is generally governed by the background gas pressure which results in collisions between the expanding plume and the gas molecules [Low96, Sin98].

PLD shows several characteristics differentiating it from other thin film growth techniques due to its use of energetic pulsed UV laser. Firstly, under optimized condition, congruent transfer of the target material to thin film sets PLD apart from thermal evaporation or sputtering which are incongruent transfer methods [Low96]. Congruent transfer is the consequence of the vaporization of all the segment of the target in less than a nanosecond into an energetic plume of material [Bou99].

Secondly, deposition is induced by energetic plasma which contains ablated non-equilibrium species inside. The kinetic (typically, ≥ 52 eV for 100 atomic mass units) and internal excitation energies of ablated species in the plume can be used to assist film formation and to promote chemical reactions, both in gas phase and on the growing film surface [Low96]. This non-equilibrium processing enables PLD to grow

high quality thin films at 50-100°C lower temperatures than used in other thin film growth techniques [Sin90, Sin98]. Introduction of short wave-UV lamp inside the PLD chamber broadens the versatility of the non-equilibrium processing in many areas [Cra98, Sri99].

Thirdly, its capability for reactive deposition in ambient gases is attributed to not having to use electron beams or hot filaments. Energetic species in the plume react readily with gas molecules to form simple oxides, nitrides, or hydrides, which allows the growth of multicomponent ferroelectric, ferrite, and biocompatible oxide ceramics [Low96].

Fourthly, multilayered epitaxial heterostructures can be grown by PLD using a multitarget carousel for rapid target switch with a separate target for each layer. By choosing a low deposition rate ($\sim 0.1 \text{ \AA/pulse}$) with automatic controlling system, atomic layer step coverage and thickness control is possible in PLD [Low96].

Finally, the presence of particulates and spatial thickness and composition variations are commonly observed in PLD films which have limited their use for semiconductors and other electronic applications. A rotating vane velocity filter is reported as an effective remover of the particulates during deposition [Low96]. Otherwise low energy deposition is the only solution [Sin98]. Laser beam

rastering over a large area diameter target, as shown in Figure 2.14, deposited successfully over 150 mm diameter substrates with variations of $\pm 2.3\%$ in thickness and $\pm 0.5\%$ in composition [Gre95].

In order to understand the fundamental mechanisms of PLD and fabricate high quality thin films, several in-situ diagnostic techniques such as mass spectrometry, high speed photography, optical absorption, and emission spectroscopy techniques have been developed in PLD [Sin98, Xu 95]. Mass spectrometry allows the analysis of the charged part of the plume, and both absorption and emission spectroscopy techniques provide complementary information together on the nature of species present in the laser-induced plasma [Sin98]. Emission spectrometer is dependent of the presence of excited species, whereas absorption spectrometer is capable of inspecting cool species [Sin98]. The detailed information on the optical measurement techniques are published elsewhere [Bat94, Bro93, Geo94]. Information obtained from these techniques with time-resolved high speed photographs is used to investigate both the quantitative and qualitative analysis of the species in the laser-induced plasma, which can eventually lead to deposition of high-quality thin films.

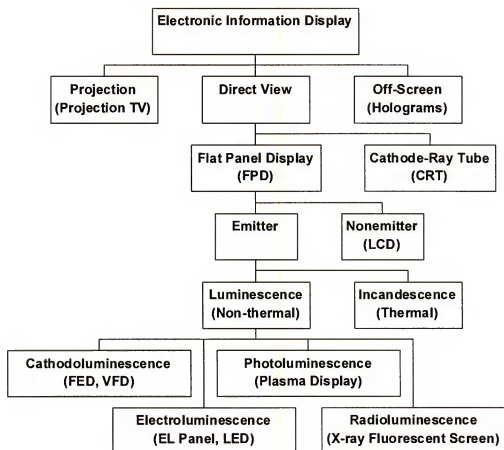
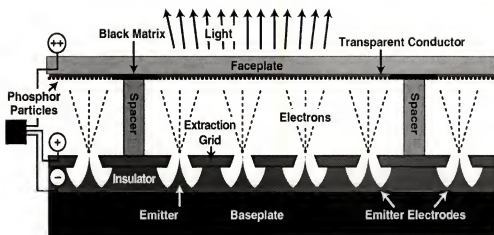
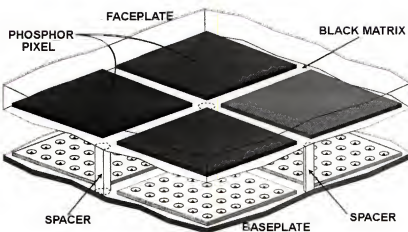


Figure 2.1. Simplified classification of electronic information displays including FED which is one of the emitter-based direct-view FPDs using CL.

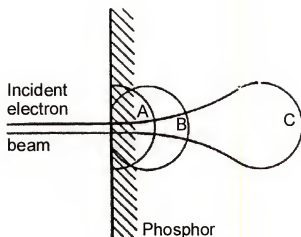


(a)

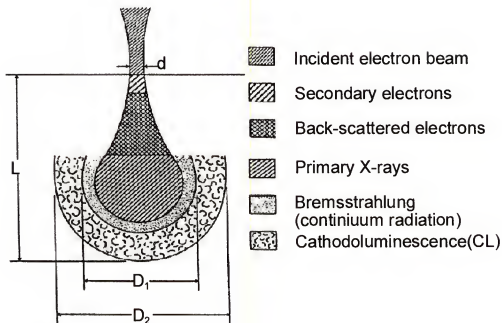


(b)

Figure 2.2. (a) Cross sectional view, and (b) structural design (lower) of field emission display (FED) called flat CRT [Micron].

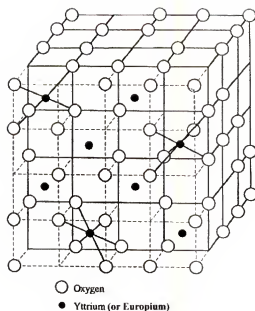


(a)

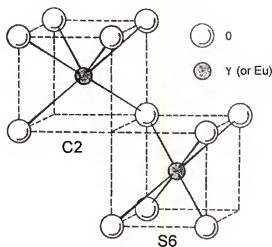


(b)

Figure 2.3. (a) Changes of interaction volume from A to C with increase of electron energy from several keV to tens of keV [Yam98] (b) Qualitative representation of an electron beam interaction with a solid. Shown are d which represents the incident beam diameter, L is the depth of CL generation volume, D_1 is the diameter of where secondary X-rays are generated, and D_2 represents the full diameter to which CL is generated [Mar88].



(a)



(b)

Figure 2.4. (a) Unit cell structure of $\text{Y}_2\text{O}_3:\text{Eu}$ phosphor which consists of eight incomplete fluorite structures with a $1/4$ of oxygen vacancies, which results in 80 atoms total (Y: $8\text{FCC} \times 4\text{atoms} = 32$ Y-atoms; O: 8 tetrahedral interstitial sites $\times 8\text{FCC} = 64$ O-atomic sites, but 16 O-vacancies allow 48 O-atoms; \therefore total: $32(\text{Y}) + 48(\text{O}) = 80$ atoms) [Bar97]. (b) Two different octahedral sites, C2 and S6, which can be occupied by yttrium or europium ion in the $\text{Y}_2\text{O}_3:\text{Eu}$ crystal structure [And70].

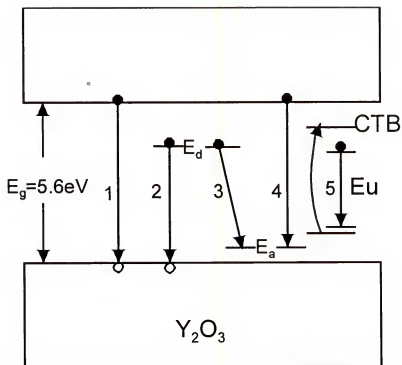


Figure 2.5. Intra-atomic transition within europium atom in Y_2O_3 host lattice designated by 5. Other transitions are also shown in the figure such as inter-band (1), donor to free hole (2), donor to acceptor, and free electron to acceptor (4).

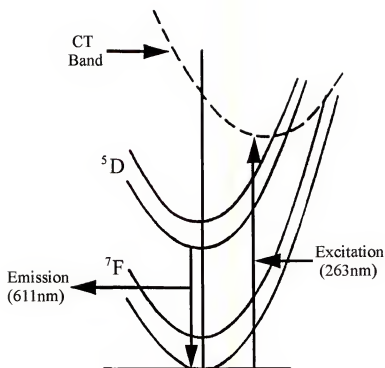


Figure 2.6. Simplified band structures of $\text{Y}_2\text{O}_3:\text{Eu}$ phosphor showing excitation to CT band at energies around 4.71 eV (=263 nm) and optical emission of 611 nm (=2.03 eV) from ^5D to ^7F band [Bla94].

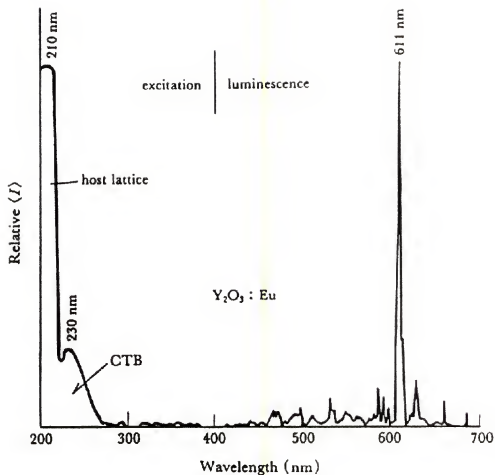


Figure 2.7. Spectrum of $\text{Y}_2\text{O}_3:\text{Eu}$ showing both excitation and luminescence regimes [Oza90]. Broad absorption peaks by host lattice and CTB are shown below 300 nm wavelength, while a sharp main emission peak is shown at 611 nm wavelength.

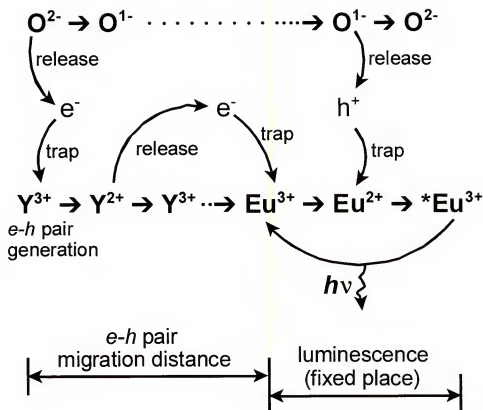


Figure 2.8. Proposed luminescence process of $\text{Y}_2\text{O}_3:\text{Eu}$ phosphor showing a charge transfer from the host matrix (Y_2O_3) to the activator (Eu) and optical transition at Eu site [Oza90].

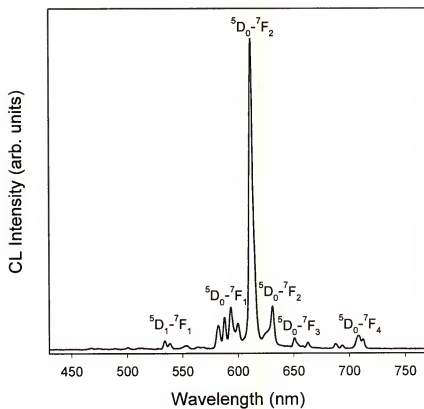


Figure 2.9. CL spectrum of $\text{Y}_2\text{O}_3:\text{Eu}$ phosphor showing different peaks and intensities induced by either magnetic ($^5\text{D}_1-^7\text{F}_1$, $^5\text{D}_0-^7\text{F}_1$) or electric ($^5\text{D}_0-^7\text{F}_{2-4}$) dipole transition [Cho98c].

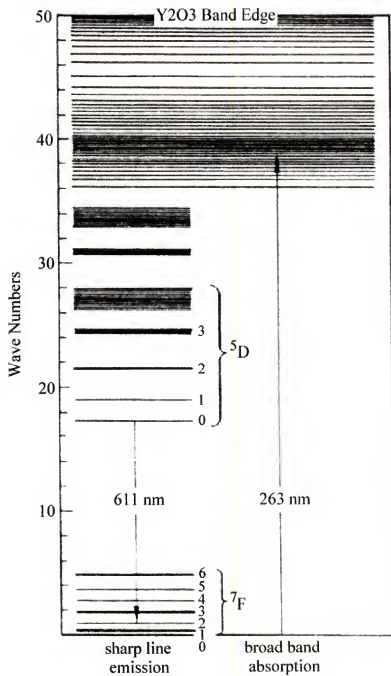


Figure 2.10. Band structures of $\text{Y}_2\text{O}_3:\text{Eu}$ phosphor showing broad band absorption to CT band at energies around 4.71 eV ($=263 \text{ nm}$) and sharp line emission of 611 nm ($=2.03 \text{ eV}$) from $^5\text{D}_0$ to $^7\text{F}_2$ band [Wic64].

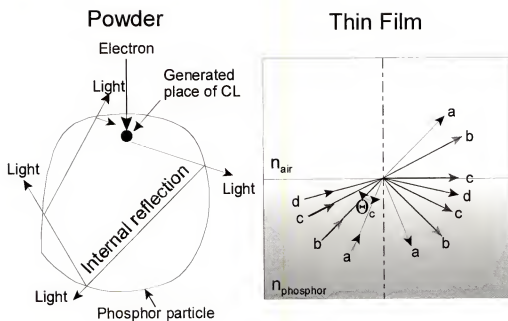


Figure 2.11. Effects of internal reflection on thin film phosphor in comparison to that of powder phosphor [powder: modified from Ura80]. Generated light eventually escapes through multiple internal reflections in the powder particle while only light at $\theta < \theta_c$ is emitted and all other rays are internally reflected in the thin film, according to Snell's law: $\theta_c = \sin^{-1}(n_{air}/n_{phosphor})$ [Jon99].

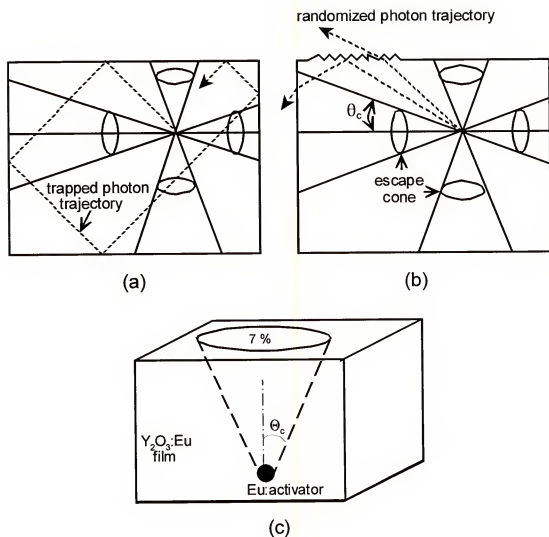


Figure 2.12. Escape cones and photon trajectories inside the material for (a) an ideal flat surface and (b) a rough surface [Lee98b]. A simple geometric approximation of the fraction of the emitted light (escape cone or cone of emission) which is expressed by, $F = 0.5(1 - \cos \theta_c) = 1/(4n^2)$ [Car66], results in (c) $F = 7\%$ only for $Y_2O_3:Eu$ TFP ($n = 1.93$ at 611 nm , $\theta_c = 31^\circ$).

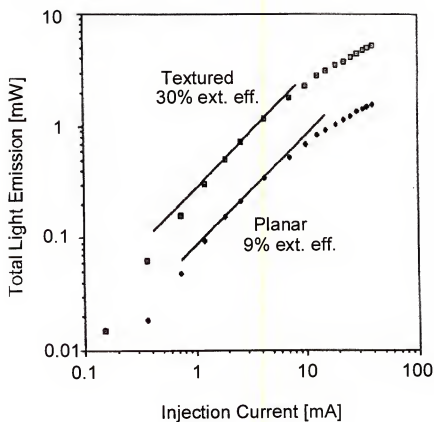


Figure 2.13. Enhanced external efficiency from 9 to 30 % by introducing a textured surface structure in a TFP [Sch93].

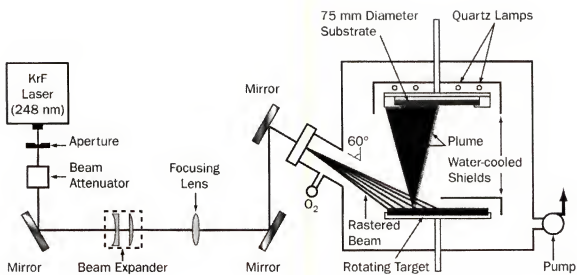


Figure 2.14. Schematic illustration of PLD experimental setup for large area processing by rastering of a large diameter target with rastered laser beam [Bou99].

CHAPTER 3 EXPERIMENTAL APPROACH

The objective of this research is to understand the effects of the fundamental parameters controlling the luminance properties of TFPs with a theoretical model developed for this study. The primary parameters considered are TFP thickness, roughness, optical interface, surface recombination rate, and e-beam-solid interaction. Since all of these parameters are inter-related, a deconvolutional model considering these parameters in TFPs should be developed. Therefore, a new theoretical model has been developed to predict the luminance properties of all kinds of TFPs. This model will eventually lead to the fabrication of TFPs for FEDs with optimum CL properties. It should be noted that most, if not all, of the earlier thin film studies have not looked into the interdependence of these parameters, and that the conclusions may typically not take into account some of the interconnected factors.

$\text{Y}_2\text{O}_3\text{:Eu}$ red phosphor was selected for this research because of its high brightness, reduced outgassing, ease of handling at room temperature, and high thermal as well as electrical stability [Ohn98]. The technique to fabricate the

TFPs for this study was PLD as it has been successfully shown to grow high quality $\text{Y}_2\text{O}_3:\text{Eu}$ TFPs [Cho97a,b, Cho98a,b,c, Jon97a,b]. Various sheet materials were used as the substrates for the $\text{Y}_2\text{O}_3:\text{Eu}$ TFPs. Microstructural and optical characterizations were conducted in the laboratories and MAIC (major analytical instrument center) in Materials Science and Engineering (MSE) Department at the University of Florida. Modeling was basically conducted using Mathcad 8 software for numerous mathematical calculations and final predictable solutions for various TFP systems.

Target Preparation

Europium-activated yttrium oxide powder phosphor with a chemical formula $(\text{Y}_{0.97}\text{Eu}_{0.03})_2\text{O}_3$, hereafter designated as $\text{Y}_2\text{O}_3:\text{Eu}$, (Osram Sylvania Inc.), was cold pressed into a 2.5 cm diameter pellet to prepare a bulk target for PLD. To obtain a dense and compact solid target, Ag_2O was added as a flux material to $\text{Y}_2\text{O}_3:\text{Eu}$ powder prior to compaction [Kum93]. The $\text{Y}_2\text{O}_3:\text{Eu}$ pellet containing Ag_2O was sintered at 1400°C for 24 hours in air. The chemical composition and homogeneity of the final target was examined by carrying out elemental analysis using Auger electron spectroscopy (AES) and energy dispersive x-ray spectrometer (EDS) on the outer as well as on the fractured surfaces of the sintered targets.

Substrate Materials

Substrate materials used for $Y_2O_3:Eu$ TFPs were amorphous quartz, (0001) sapphire, (100) lanthanum-aluminum oxide (LAO), and (100) silicon wafers. Diamond buffer layer was coated on the silicon substrate using a hot filament chemical vapor deposition (HFCVD) technique. The absorption coefficient (α) of all the materials and refractive index (n) of LAO were measured using variable angle spectroscopic ellipsometry (VASE) and a Perkin-Elmer Lambda 9 UV-VIS-NIR spectrometer (UVNS) according to the relationship of

$$I_t = I_0 \exp(-\alpha x) \quad (3.1)$$

$$\alpha = \frac{4\pi k}{\lambda} \quad (3.2)$$

where I_t is the intensity of transmitted light, I_0 is the intensity of incident light, x is the pass length, λ is the wavelength of the incident light, and k is the extinction coefficient. The critical angle (θ_c) between two different optical media was calculated using Snell's law expressed by

$$n_1 \sin \theta_1 = n_2 \sin \theta_2 \quad (3.3)$$

$$\theta_c = \sin^{-1}\left(\frac{n_1}{n_2}\right) \quad (3.4)$$

where θ is the incident angle of light to the normal.

TFP Fabrication Using PLD

Fabrication of $\text{Y}_2\text{O}_3\text{:Eu}$ TFPs were carried out in a vacuum chamber where a rotating $\text{Y}_2\text{O}_3\text{:Eu}$ solid target was ablated by an incident KrF pulsed excimer laser beam with a wavelength of 248 nm. The substrates were mounted on the face plate of a substrate heater placed parallel to the target surface. A schematic illustration shown in Figure 3.1 represents the PLD system used for fabricating $\text{Y}_2\text{O}_3\text{:Eu}$ TFPs. The processing conditions to fabricate $\text{Y}_2\text{O}_3\text{:Eu}$ TFPs are in Table 3.1. The temperatures of the substrates were controlled and monitored using a programmable thermocouple temperature controller and a pyrometer.

Table 3.1. Applied PLD conditions for $\text{Y}_2\text{O}_3\text{:Eu}$ TFPs.

energy density (J/cm^2)	repetition rate (Hz)	oxygen pressure (mTorr)	distance from target to substrate (cm)	substrate temperature ($^{\circ}\text{C}$)
1.0-1.5	10	70-400	5-9	700-750

Characterization

Microstructural analysis on the $\text{Y}_2\text{O}_3\text{:Eu}$ TFPs were characterized using X-ray diffraction (XRD), scanning electron microscopy (SEM), atomic force microscopy (AFM), and transmission electron microscopy (TEM) techniques. Film thicknesses were estimated using VASE, TENCOR Alpha-step 500 surface profilometer having a mechanical stylus, and SEM cross-sectional views of the fractured $\text{Y}_2\text{O}_3\text{:Eu}$ TFPs. Surface chemistry was analyzed using AES, and EDS attached to the SEM. Optical properties of substrates were measured using UVNS, VASE, PL spectrophotometer, and CL spectrophotometer. Some of CL efficiency in both reflection and transmission modes were conducted in the Phosphor Technology Center of Excellence (PTCOE) laboratory. Some of TEM analysis was conducted at Oak Ridge National Laboratory.

X-Ray Diffraction (XRD)

A Philips APD 3720 X-ray diffractometer was used to analyze structural changes and crystalline phases of the $\text{Y}_2\text{O}_3\text{:Eu}$ TFPs. A collimated beam of X-rays was incident on a specimen and was diffracted by the crystalline phases in the specimen according to Bragg's law ($\lambda=2d\sin\theta$, where d is the spacing between atomic planes in the crystalline phase). The intensity of the diffracted X-rays was measured as a

function of the diffraction angle 2θ and the specimen's orientation. The tube generator was operated at 40 kV and 20 mA with at a wavelength (λ) of 1.54 \AA Cu- K_α radiation. X-ray step scan was performed in the range of 10° to 140° with a step size of 0.05° and 0.25 second integration time per step. Receiving slit of 0.2 was used.

Scanning Electron Microscopy (SEM)

A JEOL JSM-6400 SEM was used to examine the surface structure of the $\text{Y}_2\text{O}_3:\text{Eu}$ TFPs and to measure film thickness from the cross-sectioned $\text{Y}_2\text{O}_3:\text{Eu}$ TFPs with different deposition conditions. Due to non-conducting nature of the $\text{Y}_2\text{O}_3:\text{Eu}$ TFPs, a conductive carbon coating layer was applied on the TFP surfaces for better SEM images and EDS analysis. SEM was operated at 15 to 25 kV with working distance of 15 mm. A focused electron beam was scanned over the specimen. Secondary and backscattered electrons were produced by the incident electrons. Detectors measure intensity versus position and display this on a CRT. The electron yield from different atomic numbers in the specimen results in the backscattered contrast. The secondary contrast is caused by the dependence of the electron yield on the topography.

The EDS attached to the SEM is based on bombarding a specimen with a focused beam of energetic electrons to induce emission of characteristic X-rays. The high energy

electron beam is used to eject core level electrons from the constituent atoms of the material. The ejected core electron leaves a vacancy which can be filled by the de-excitation of a higher level electron. As a consequence of the de-excitation process, X-rays are emitted. The emitted X-rays have an energy which is characteristic of the parent atom. The X-rays were measured by EDS.

Atomic Force Microscopy (AFM)

AFM was used to get information on the surface roughness and other morphological details of the $Y_2O_3:Eu$ TFPs. The scan area was in the range of 10×10 to $40 \times 40 \mu m^2$ and contact mode was used to scan the areas. AFM employs very sharply etched silicon nitride tip attached to a cantilever for contact mode (or silicon tip for tapping mode). As the tip is brought close to the sample surface, it experiences a weak Van der Waals attractive force. The tip is drawn closer causing the electron clouds of the tip and sample to overlap which induces a repulsive electrostatic force. This force goes to zero as the distance between the atoms reach a few angstroms. When the Van der Waals force becomes repulsive, the tip is in contact with the sample (contact mode) while the AFM is in tapping mode when the force is in the attractive regime.

In contact mode, AFM is operated by scanning across the sample surface with the tip attached to the end of the cantilever which is monitored by measuring changes in deflection of the cantilever with a split photodiode detector. A feedback loop maintains a constant deflection between the cantilever and the sample by vertically moving the scanner at each (x,y) data point to maintain a setpoint deflection. By maintaining a constant deflection, the force between the tip and the sample also remains constant. The distance that the scanner moves vertically at each (x,y) data point is stored by the computer to form the topographic image of the sample surface as well as other quantitative topographic data such as roughness, grain size, step heights, hardness, friction, and wear strengths.

Auger Electron Spectroscopy (AES)

A Perkin-Elmer PHI 660 AES was used to obtain elemental compositional details from the top three or four atomic layers of the sintered $Y_2O_3:Eu$ target and TFPs. Briefly discussing about fundamentals of AES, an energetic incident electron beam bombards the atoms on the surface to eject core electrons from a level of energy E_x . The ejected core electron leaves a vacancy which can be filled by an electron from a lower energy level, E_y , which results in the ejection of another electron from a level of energy E_z . This third

electron, Auger electron, has a final kinetic energy of $E_{\text{Auger}} = E_x + E_y - E_x$ which is characteristic of the parent atom. Due to its low kinetic energy (40-2400 eV), only the Auger electron ejected from the top few atomic layers of sample can escape from the surface without undergoing inelastic scattering in the solid. The intensity of the Auger peak is proportional to the number of atoms present, which permits semiquantitative analysis without the use of standards. All elements from Li to U are detectable by AES.

Transmission Electron Microscopy (TEM)

A Philips EM400 TEM was used to investigate crystal structure of the $\text{Y}_2\text{O}_3:\text{Eu}$ TFPs on LaAlO_3 substrate. Bright field images and electron diffraction patterns were recorded in operation at 100 kV. In order to determine the detailed atomic structure of $\text{Y}_2\text{O}_3:\text{Eu}/\text{LaAlO}_3$ interface, high-resolution Z-contrast scanning transmission electron microscopy (STEM) imaging of the samples was carried out in a VG HB603 STEM at 300 kV. The Z-contrast image is a direct image with intensity highly localized about the atomic column positions and approximately proportional to the mean square atomic number (Z).

Both plan-view and cross-section specimens were prepared for TEM and STEM observations by mechanical grinding, polishing, and dimpling, followed by Ar^+ ion

milling using a E.A. Fichione Ion Polishing System. An incident angle of 13° and a beam voltage of 3.5 kV were initially used and the voltage was reduced to 1.0 kV for the final thinning until a hole was made around interface of two surfaces. Cross-sectional slices were obtained by cutting the $\text{Y}_2\text{O}_3\text{:Eu/LaAlO}_3$ along the [100] or [010] directions (using pseudocubic indexing) and then gluing face to face using metallic bond, followed by curing for 20 minutes at 100°C .

Variable Angle Spectroscopic Ellipsometry (VASE)

J. A. Woollam VASE was used to measure the thicknesses and optical constants of $\text{Y}_2\text{O}_3\text{:Eu}$ TFPs and substrates. Three different incident angles (65° , 70° , 75°) were used to measure film thickness and optical constants in the range of wavelengths between 270 and 700 nm. Ellipsometry measures the change in polarized state of light reflected from the surface of (or transmitted through) a sample. An incident beam of light with a known polarization state is reflected from the surface (or interface). The change in the polarization state of the incident light due to the sample is measured. The measured values are expressed as the azimuth (Ψ_i) and the phase difference (Δ). These values are related to the ratio of Fresnel reflection coefficients, R_p and R_s for p- and s-polarized light, respectively, as defined as, $R_p/R_s = \tan(\Psi_i)\exp(i\Delta)$. The calculation of the

two parameters based on physical models gives information on film thickness and optical properties such as extinction coefficient (k) and refractive index (n) of the film and/or substrate.

UV-VIS-NIR Spectrometer (UVNS)

A Perkin-Elmer Lambda 9 UVNS was used to measure optical properties of $Y_2O_3:Eu$ TFPs and substrates in terms of absorption coefficient (α) and transmittance of light. A range of wavelengths from 200 to 750 nm was used with a scan speed of 60~480 nm/min. Two different light sources, a deuterium (D_2) for UV and a halogen lamp for visible (VIS) and near infrared (NIR), were used to cover the entire range of the wavelengths required. Source change is automatic during measurements.

Photoluminescence (PL)

PL brightness and Commission Internationale de l'Eclairage (CIE) chromaticity of the $Y_2O_3:Eu$ TFPs were measured at room temperature using a Photo Research (PR) 650 spectrophotometer. The PR-650 supplies a spectral range of 380-780 nm, wavelength resolution less than 3.5 nm/pixel, and brightness sensitivity between 0.1 and 3400 cd/m². PL was excited by UV radiation using a mercury discharge lamp with a dominant wavelength of 254 nm. The UV intensity induced by the mercury lamp was 2250 $\mu W/cm^2$ at a distance of

3 inches with a wavelength of 254 nm. The UV lamp and the detector were arranged at 90° apart, therefore the UV light was incident onto the sample at 45° and the emitted light from the sample was also detected at 45° by the PR-650. The geometric arrangement for PL measurement the UV lamp and PR-650 is schematically illustrated in Figure 3.2.

Cathodoluminescence (CL)

CL was excited by a primary electron beam from a EGPS-7H Kimball Physik electron gun with energies from 0.5 to 5 keV and currents from 31.4 nA to 314 nA. The spot size was 2 mm in diameter and thus the corresponding current density was in a range of 1 to 10 $\mu\text{A}/\text{cm}^2$. The sample current was determined by biasing the electrically isolated sample carousel with a 120 volts battery with an ammeter in series to ground. CL properties were measured using an Ocean Optics S2000 fiber optic spectrometer with a charge-coupled device (CCD) detector attached to the personal computer. Figure 3.3 shows a schematic illustration of the CL measurement system, and Figure 3.4 schematically illustrates a CL measurement technique simultaneously in transmission mode (T-mode) and reflection mode (R-mode) for TFPs. TFPs are excited by e-beams from the electron gun (e-gun), and the emitted light is detected by the two photo-cameras attached to the PC controller to give brightness data.

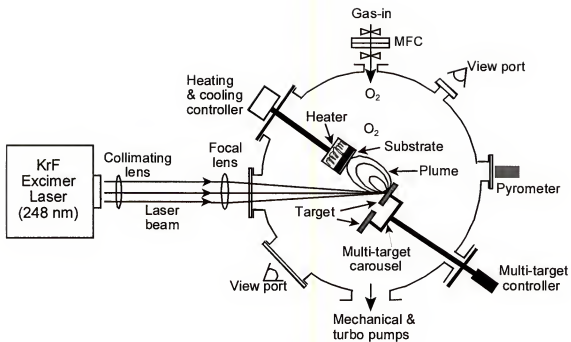


Figure 3.1. Schematic illustration of 248 nm KrF excimer PLD system equipped with a multi-target carousel and its controller, ambient gas supplier, and programmable heating and cooling controller for fabricating Y₂O₃:Eu TFPs.

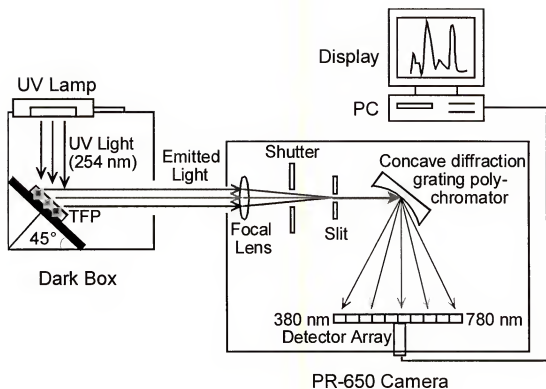


Figure 3.2. Schematic illustration of the PL measurement system for $\text{Y}_2\text{O}_3:\text{Eu}$ TFPs. The TFP is excited by 254 nm UV radiation and the emitted light is detected by PR-650 photo camera followed by display on the screen attached to personal computer.

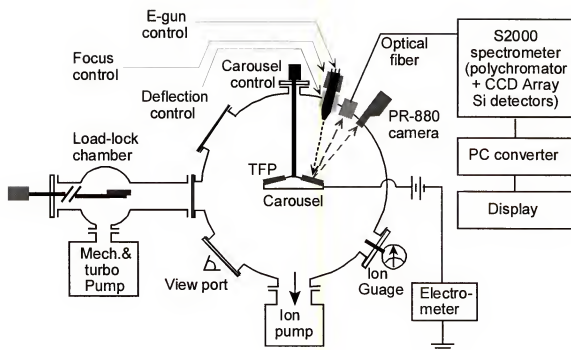


Figure 3.3. Schematic illustration of the CL measurement system for $\text{Y}_2\text{O}_3:\text{Eu}$ TFPs. The TFP is excited by an e-beam from e-gun, and the emitted light is detected by both S2000 spectrometer for spectral measurements and PR-880 photo camera for efficiency measurements.

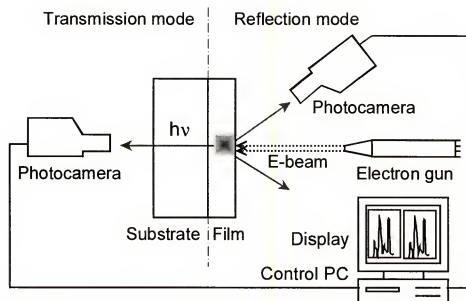


Figure 3.4. Schematic illustration of the CL measurements in two different modes (transmission and reflection) simultaneously for TFPs. TFPs are excited by e-beams from the e-gun, and the emitted light is detected by the two photocameras attached to the PC controller to give brightness data.

CHAPTER 4

RESULTS AND DISCUSSION

In order to investigate the effects of the surface roughness on the luminance properties of TFPs, novel approaches were conducted. First, a diamond buffer layer was employed between TFP and silicon substrate prior to deposition of TFP. The as-grown diamond buffer layer is inherently rough, and thus the roughness of the TFP can be suitably controlled by varying the roughness of the diamond buffer layer. For the next stage of the approach, $Y_2O_3:Eu$ TFPs were fabricated on various substrate materials with different thickness and roughness values using a controlled experimental procedure to investigate the effects of other parameters determining the luminance properties of TFPs with surface roughness. In this chapter, therefore, the correlations between microstructure and luminance characteristics of $Y_2O_3:Eu$ TFPs will be discussed, including the roles of diamond buffer layer and substrate properties.

Target and Diamond Buffer Layer

Figures 4.1(a)-(c) show SEM micrographs of bare $\text{Y}_2\text{O}_3\text{:Eu}$ powder particles with a mean particle size of $\sim 3 \mu\text{m}$, sintered $\text{Y}_2\text{O}_3\text{:Eu}$ target, and surface of diamond buffer layer grown on (100) silicon substrates at 900°C , respectively. The broken particles were commonly observed in the $\text{Y}_2\text{O}_3\text{:Eu}$ targets as shown in Figure 4.1(b), which were induced during cold compaction under high pressure. The elemental analysis using AES and EDS on powder, target, and films indicated that there was no detectable difference in chemical composition between the starting powder and the final target, from one target to another target, from the surface to the interior of the target, and from the target to the final films. Although the final targets prepared using Ag_2O were dense and compact, silver was not detected in the final targets either from the outer surface or the fractured surfaces. This suggests that all the silver-related species were evaporated during the 24 hour sintering at 1400°C and thus it acted as a flux to densify the targets. Figure 4.1(c) shows the constituent pyramidal shape grains and the rough surface structure ($\sim 400 \text{ nm}$ in RMS roughness) of (111) polycrystalline diamond buffer layer. The roughness of the diamond film was due to the inherent nature of nucleation and growth of the diamond films [Lee97, Lee98a]. Therefore,

it was of interest to investigate the role of the rough diamond buffer layer when inserting it between the TFP and the substrate in the modification of the microstructure, CL, and PL properties of the $\text{Y}_2\text{O}_3\text{:Eu}$ TFPs.

$\text{Y}_2\text{O}_3\text{:Eu}$ TFPs on Diamond Buffer Layer

Shown in Figures 4.2(a)-(d) are the SEM micrographs of the $\text{Y}_2\text{O}_3\text{:Eu}$ TFPs grown on bare silicon substrates at 500 and 700°C, and on the diamond-coated silicon substrates at 500 and 700°C, respectively. It is clear from these micrographs that the grains in the $\text{Y}_2\text{O}_3\text{:Eu}$ TFPs grown at 500°C are not only small in size but are also not well defined in shape, whereas the grains in the films grown at 700°C are larger and distinctly octahedral in shape. This octahedral shape perpendicular to the substrate surface indicates that $\text{Y}_2\text{O}_3\text{:Eu}$ crystals have a preferred [100] orientation at higher temperatures [Wil90, Wil93]. However, as shown in Figure 4.2(c) and (d), the surface morphology of the $\text{Y}_2\text{O}_3\text{:Eu}$ TFPs grown on the diamond buffer layer are significantly rougher, and the average size of the octahedral crystallites is ~2 times larger than that in the TFPs grown on the bare silicon at similar temperatures.

Figures 4.3 and 4.4 show the XRD patterns of the $\text{Y}_2\text{O}_3\text{:Eu}$ TFPs grown on bare silicon and diamond-coated

substrates at different temperatures, respectively. These figures show that at temperatures lower than 500°C, only very few diffraction peaks appear with very low intensities and are marked by large full width half maximums (FWHMs). The FWHMs of the (400) peaks decrease and the intensity increases as the deposition temperature increases from 500 to 700°C in the films on both types of substrate. This indicates that the $Y_2O_3:Eu$ crystallites are preferentially aligned in [100] direction at higher temperatures. A close examination of relative intensities of diffraction peaks shown in Figures 4.3 and 4.4 points out that the ratio of the (400)/(222) peaks of the $Y_2O_3:Eu$ TFPs grown at the temperatures of 500, 600 and 700°C on the bare silicon is much larger than those on the diamond-coated silicon substrates. Slower increase in the intensity of (400) peak as a function of temperature in the case of the $Y_2O_3:Eu$ TFPs on the diamond-coated silicon substrates may result from the smaller free energy difference between the (111) surface of the diamond and the (222) surface of $Y_2O_3:Eu$ TFP. On the other hand, in the case of the $Y_2O_3:Eu$ TFPs on the bare silicon substrates, an unfavorable interfacial energy between the (100) plane of the bare silicon and the (222) plane of $Y_2O_3:Eu$ TFPs may be responsible for the switch in orientation from (222) at 500°C to (400) at 700°C [Cho97a,b].

The film thicknesses were measured using the SEM cross-sectional views of the $\text{Y}_2\text{O}_3\text{:Eu}$ TFPs on both bare and diamond-coated silicon substrates which are shown in Figures 4.5(a) and (b), respectively. The cross-sectional views show that the $\text{Y}_2\text{O}_3\text{:Eu}$ TFPs have thicknesses of $\sim 2.5 \mu\text{m}$. The diamond buffer layer with $\sim 10 \mu\text{m}$ thickness is also shown in between the $\text{Y}_2\text{O}_3\text{:Eu}$ TFP and silicon substrate in Figure 4.5(b). The morphologies of these TFPs are shown in Figure 4.7, which displays the AFM micrographs of the $\text{Y}_2\text{O}_3\text{:Eu}$ TFPs on the bare and diamond-coated silicon substrates. The measured RMS roughness values of the $\text{Y}_2\text{O}_3\text{:Eu}$ TFPs on the bare and the diamond-coated silicon substrate at 700°C were ~ 50 and ~ 400 nm, respectively. The higher roughness of the $\text{Y}_2\text{O}_3\text{:Eu}$ TFPs grown on the diamond-coated silicon substrates resulted from the presence of the rough diamond buffer layer.

The normalized CL spectra recorded from the $\text{Y}_2\text{O}_3\text{:Eu}$ TFPs deposited on the diamond-coated and the bare silicon substrates at 700°C are shown in Figure 4.7. Interestingly, the $\text{Y}_2\text{O}_3\text{:Eu}$ TFP on the diamond-coated silicon substrate showed more than 3 times higher CL brightness than the TFP on bare silicon substrate did. This improved CL brightness from the TFPs on the diamond-coated silicon substrate is mainly associated with the insertion of the rough diamond buffer layer. The CIE chromaticity was normally distributed

around $x = 0.640$ and $y = 0.347$ for the TFPs grown at higher temperatures. These color outputs are within the coordinate range ($x=0.629\sim0.642$ and $y=0.530\sim0.346$) for the $Y_2O_3:Eu$ red phosphor [Jac96]. In the spectra, the set of three closely spaced peaks at 587, 593 and 596 nm wavelengths is associated with magnetic dipole transitions ($^5D_0-^7F_1$), whereas the peaks at 579, 610-630 and 680-710 nm are associated with electric dipole transitions ($^5D_0-^7F_0$, $^5D_0-^7F_2$, and $^5D_0-^7F_4$, respectively), as discussed earlier in Chapter 2 with the origin of magnetic and electric dipole transitions.

Figure 4.8 shows the PL spectra recorded from the $Y_2O_3:Eu$ TFPs whose CL spectra are shown in Figure 4.8. For comparison, we have also shown the PL spectrum recorded from $Y_2O_3:Eu$ powder in Figure 4.8. The PL spectra are consistent with the sharp CL peaks shown in Figure 4.7. Some broadening of the PL peaks in the spectra were caused by the lower resolution of the PR-650 photo-camera. The brightnesses in both CL and PL of the $Y_2O_3:Eu$ TFPs on diamond-coated silicon substrates were typically 2-4 times higher than those on bare silicon substrates. Figure 4.9 shows the temperature dependence of the PL brightness of $Y_2O_3:Eu$ TFPs. The PL brightness of the $Y_2O_3:Eu$ TFPs on both bare and diamond-coated silicon substrates increases with the increase in deposition temperature. A similar temperature dependence of the $Y_2O_3:Eu$ TFPs and powder phosphors was also reported by

Rao [Rao96a,b]. For comparison, the brightness values of both films have been normalized with respect to that of the $\text{Y}_2\text{O}_3\text{:Eu}$ powder phosphor used for the synthesis of the target (powder brightness = 100 %). The brightness of the $\text{Y}_2\text{O}_3\text{:Eu}$ powder phosphor was measured using an approximate monolayer coating of powder material, which is close to the thickness of the $\text{Y}_2\text{O}_3\text{:Eu}$ TFPs. The improvement in brightness with increase in temperature is associated with the improved crystallinity leading to decrease in non-radiative defects and increased probability of optical transitions. At higher growth temperatures, the higher atomic jump frequency leads to better crystal structure. On the contrary, at lower growth temperatures, atoms have fewer jumps to settle down their lattice sites resulting in films with inferior crystallinity.

It can be noticed from Figure 4.9 that the PL brightness of the $\text{Y}_2\text{O}_3\text{:Eu}$ TFPs on diamond-coated silicon substrates is higher than those on bare silicon substrates throughout the deposition temperature range. The realization of the $\text{Y}_2\text{O}_3\text{:Eu}$ TFPs with higher brightness using a diamond buffer layer, is mainly attributed to more outcoupling of light due to reduced internal reflection. The results of the work on the $\text{Y}_2\text{O}_3\text{:Eu}$ TFPs on diamond buffer layer was the motivation for driving this study further to the modeling.

Brief Overview of Microstructural Investigations

Figure 4.10 shows that the film thicknesses of $Y_2O_3:Eu$ TFPs deposited on amorphous quartz, (0001) sapphire, (100) LAO, and (100) silicon substrates, increase with deposition time. The very small differences among substrates are believed to be induced by the experimental errors during the measurements due to different film morphologies and optical properties of the substrates. The average growth rate was $\sim 140 \text{ \AA/min}$ (2.3 \AA/sec or 0.23 \AA/pulse).

Figure 4.11 shows the variations in the RMS roughness of the $Y_2O_3:Eu$ TFPs with increase in film thickness. The $Y_2O_3:Eu$ TFPs on sapphire substrates showed the highest roughness among the films while the $Y_2O_3:Eu$ TFPs on LAO substrates showed lowest roughness. The $Y_2O_3:Eu$ TFPs on quartz and silicon substrates showed some less roughness except the film on quartz substrate which shows a rapid drop from 16 to 12 nm in RMS roughness at about $0.5 \text{ }\mu\text{m}$ thickness.

The AFM micrograph studies on the surface morphologies of the $Y_2O_3:Eu$ TFPs show visually the difference in roughness. Figures 4.12 and 4.13 show two representative sets of the AFM micrographs of the $Y_2O_3:Eu$ TFPs deposited on (a) quartz, (b) sapphire, (c) silicon, and (d) LAO substrates for 6000 pulses (10 min, $\sim 0.14 \text{ }\mu\text{m}$ thick) and for

18000 pulses (30 min, $\sim 0.4 \mu\text{m}$ thick), respectively. The measured RMS roughness values were 5.30, 5.40, 0.50, and 5.50 nm from (a) to (d) in Figure 4.12, respectively, and 16.00, 17.00, 13.60, and 1.00 nm from (a) to (d) in Figure 4.13, respectively. The surface morphologies of the $\text{Y}_2\text{O}_3\text{:Eu}$ TFPs on quartz, sapphire, and silicon substrates from (a) to (c), respectively, in both figures, show little difference while that of the films on LAO substrate show very flat surface structures. The large difference in morphology between the $\text{Y}_2\text{O}_3\text{:Eu}$ TFPs on the former three substrates and the $\text{Y}_2\text{O}_3\text{:Eu}$ TFPs on LAO substrates may be attributed to the different crystal structures of the substrate materials. Only $\sim 1\%$ lattice mismatch between the $\text{Y}_2\text{O}_3\text{:Eu}$ TFP and LAO substrate allows the films to grow epitaxially [Kum99a,b, Gao99], which resulted in the very flat surface morphologies of the films. Figures 4.14 and 4.15 show the XRD patterns of the $\text{Y}_2\text{O}_3\text{:Eu}$ TFPs deposited on (a) quartz, (b) sapphire, (c) silicon, and (d) LAO substrates for 6000 pulses (10 min, $\sim 0.14 \mu\text{m}$ thick), and for 18000 pulses (30 min, $\sim 0.4 \mu\text{m}$ thick), respectively, which are corresponding to the above AFM micrographs in Figures 4.12 and 4.13. The $\text{Y}_2\text{O}_3\text{:Eu}$ TFPs on quartz, sapphire, and silicon substrates exhibit only (111) orientation while the $\text{Y}_2\text{O}_3\text{:Eu}$ TFPs on LAO substrates exhibit only (200) orientation.

Figure 4.16 shows the FWHM values of the main XRD peaks of the $Y_2O_3:Eu$ TFPs as a function of thickness for the films deposited on various substrates. The (400) peaks were plotted for the films on LAO and the (222) peaks were plotted for the films on other substrates. Although no conclusions can be derived from these measurements, the figure shows that the $Y_2O_3:Eu$ TFPs on LAO substrates exhibited the smallest 2θ values of the FWHMs of (400) peaks. The $Y_2O_3:Eu$ TFPs on LAO substrates showed a decrease in FWHM with film thickness up to $\sim 0.3 \mu m$ (12000 pulses for 20 min) and similar behavior was observed in the films on sapphire substrates.

Figure 4.17 shows how the $Y_2O_3:Eu$ TFP grows epitaxially on LAO substrate with 2-dimensional schematic illustration. The structure of $Y_2O_3:Eu$ is closely related to a cubic fluorite structure with alternating Y- and O-layers. The atomic positions in the Y-layer are schematically shown in Figure 4.17(a). Shown also in Figure 4.17(b) is the atomic positions in La-O layer in LAO. A comparison of atomic positions in these layers of the film and the substrate materials suggests that a rotation of the film-plane (Y-layer or O-layer) by 45° can result in a situation which is very favorable for epitaxial growth of the $Y_2O_3:Eu$ TFPs on LAO substrates. Under this arrangement, represented schematically in Figure 4.17(c), the lattice mismatch is

given by $\{[(2a_s)^2 + (2a_s)^2]^{1/2} - a_f\} / [(2a_s)^2 + (2a_s)^2]^{1/2}$. In this figure, an Y-terminated layer from a unit cell of $Y_2O_3:Eu$ is diagonally superimposed on the 4×4 matrix of LAO unit cell terminated with a La-O layer. Substituting the values of a_s and a_f in this expression, we find the lattice mismatch between the film and the substrate is only $\sim 1\%$. This small difference in lattice parameters between the film and substrate promotes epitaxial film growth with better crystallinity.

Figure 4.18 is a low magnification TEM micrograph of a plan view and the corresponding selected area electron diffraction pattern (SAEDP) of the $Y_2O_3:Eu$ TFP. The SAEDP indicates that the $Y_2O_3:Eu$ TFP on the LAO substrate is a single crystalline film. The numerous small voids in the image suggest an island growth mechanism with incomplete coalescence of the islands. A cross section image of the sample is presented in Figure 4.19 (a), showing the smooth surface, sharp interface and a uniform thickness of 300 nm maintained over the entire region. Figures 4.19(a)-(b) also show the SAEDPs of the film and the $LaAlO_3$ substrate, showing the orientation relationship to be $[110]Y_2O_3 // [100]LaAlO_3$ and $[-110]Y_2O_3 // [010]LaAlO_3$. The columnar structure of the film is also apparent from the cross section image, with small rotations between neighboring grains giving the strong diffraction contrast. Each

individual column however appears to be a good single crystal, which implies that the presence of the voids may avoid the need for a high density of dislocations between the grains to accommodate the rotations, and/or a high level of stress within the grains.

In order to determine the detailed interface atomic structure, high-resolution Z-contrast STEM imaging of the samples was carried out. The Z-contrast image directly reflects the highly localized atomic column positions with intensity and the intensity is approximately proportional to the mean square atomic number (Z). Thus the La- and Al-columns in LaAlO_3 , and the Y-columns in Y_2O_3 , are directly distinguishable in a Z-contrast image taken along the $[010]$ zone axis of the LaAlO_3 substrate. Figure 4.20(a) is an atomic resolution Z-contrast STEM image of the film/substrate interface. The bright spots in the film are Y-columns, the bright spots in the substrate are La-columns, and the less bright spots are Al-columns. The O-columns are not visible. Also shown in Figure 4.20(b) is a higher magnification Z-contrast image that shows clearly the atomic structure of the interface. The substrate is seen to terminate with the Al-plane, which matches directly onto the Y-layer of the film as shown in the schematic. Another important aspect of the work concerns the possibility of Eu precipitation in the Y_2O_3 films. Z-contrast STEM is very

sensitive to Eu with $Z = 63$. In our observations, however, no sign of any precipitation was found, or of any preferential segregation to the surfaces of the columnar grains. This implies that the Eu was distributed uniformly within the films.

Optical Properties

Table 4.1 shows the measured and calculated optical data for the $Y_2O_3:Eu$ TFP and the substrate materials with an incident wavelength of 611 nm. The constants of n and t represent the refractive index and the thickness of films or substrates, respectively. The value of the critical angle (θ_c) is 0.545 arc degree which corresponds to 31.2° . According to the data in Table 4.1, the quartz substrate has the smallest optical absorption coefficient (α) for a wavelength of 611 nm. LAO is crystallographically a better substrate material for epitaxial $Y_2O_3:Eu$ TFPs [Gao99, Kum99a,b], but it is optically less advantageous than the other two transparent substrates because of its transmittance characteristics. Figure 4.21 shows the measured transmittance properties measured in a range of wavelengths from 200 to 700 nm. The figure shows that the LAO substrate has the lowest transmittance (75 % at 700 nm), followed by sapphire and quartz substrates.

Table 4.1. Optical data of $\text{Y}_2\text{O}_3\text{:Eu}$ TFP and substrates.

Constant	$\text{Y}_2\text{O}_3\text{:Eu}$	Quartz	Sapphire	LAO	Silicon
n	1.93	1.46	1.77	2.0	3.91
α (mm^{-1})	5	0.07	0.3	0.55	>200
t (μm)	0.07-0.5	1000	500	500	500
θ_c (w/air)	0.545 (31.2°)	0.755 (43.2°)	0.600 (34.4°)	0.523 (30.0°)	0.258 (14.8°)
θ_c (w/film)	1.570 (90.0°)	0.858 (49.2°)	1.160 (66.5°)	-	-
$\lambda = 611 \text{ nm}, \quad n_1: 1.0 \text{ (air)}$					

Photoluminescence

Figure 4.22 shows the PL brightness of the $\text{Y}_2\text{O}_3\text{:Eu}$ TFPs deposited on quartz, sapphire, LAO, and silicon substrates with film thickness. In the figure, the $\text{Y}_2\text{O}_3\text{:Eu}$ TFPs on quartz substrates showed the highest PL brightness followed by the TFPs on sapphire, LAO, and silicon substrates. These differences in the PL brightness of the $\text{Y}_2\text{O}_3\text{:Eu}$ TFPs were mainly attributed to the different optical properties of the substrates, which form different optical interfaces between the TFPs and substrates, resulting in different light scattering effects. In general, substrates with the smaller refractive index exhibit higher brightness in both PL and CL measurements. The details of this phenomenon will be discussed in Chapter 5.

Cathodoluminescence

Figure 4.23 shows the CL brightness of the $Y_2O_3:Eu$ TFPs deposited on quartz, sapphire, LAO, and silicon substrates with film thickness. The $Y_2O_3:Eu$ TFPs on quartz substrates also showed higher CL brightness followed by the TFPs on sapphire, LAO, and silicon substrates, like the PL in Figure 4.22. The differences in the CL brightness of the $Y_2O_3:Eu$ TFPs were also caused by the different optical properties of the substrates. The quartz substrate with the smaller refractive index ($n: \sim 1.46$) and less absorption of light, as shown in Table 4.1, gave higher brightness in both PL and CL. The detailed CL studies on the $Y_2O_3:Eu$ TFPs deposited on quartz, sapphire, and LAO substrates in the previous figures are representatively shown in Figures 4.24.

Figures 4.24(a)-(d) show the CL efficiency graphs obtained from the $Y_2O_3:Eu$ TFPs on quartz, sapphire, and LAO substrates as a function of film thickness in R- and T-modes with a current density of $0.1 \mu A/cm^2$ at 1 and 5 kV accelerating voltages. In Figure 4.24(a), at 1 kV in R-mode, the $Y_2O_3:Eu$ TFPs on LAO substrates showed higher CL efficiency where the film thickness is smaller, whereas the $Y_2O_3:Eu$ TFPs on quartz substrates showed higher CL efficiency where the film thickness is larger. Initially the $Y_2O_3:Eu$ TFPs on LAO substrates dominated the TFPs on the

other substrates in CL efficiency, but the dominance switched by the TFPs on sapphire and finally by the TFPs on quartz substrates. As the interaction volume increased at 5 kV in R-mode in Figure 4.24(b), the $\text{Y}_2\text{O}_3\text{:Eu}$ TFPs on quartz substrates showed the highest CL efficiency over the entire film thickness. When the interaction volume is small, the CL properties are greatly influenced by the surface characteristics of the TFPs. However, as the interaction volume increases, the importance of the surface characteristics becomes smaller while the importance of the optical properties of the substrates becomes larger. In Figures 4.24(c)-(d) in T-mode, the CL efficiency graphs did not clearly show the trends like in R-mode. The $\text{Y}_2\text{O}_3\text{:Eu}$ TFPs on sapphire substrates showed higher CL efficiency than the $\text{Y}_2\text{O}_3\text{:Eu}$ TFPs on the other substrates at 1 kV, but it is hard to compare the CL efficiencies of the TFPs at 5 kV due to the existence of many abrupt changes in the CL efficiency graphs. The thicker $\text{Y}_2\text{O}_3\text{:Eu}$ TFPs deposited on quartz substrates showed many abrupt changes in CL efficiency, as shown in Figure 4.24(d).

Figures 4.25(a)-(b) show the variations in the CL efficiency of the $\text{Y}_2\text{O}_3\text{:Eu}$ TFPs on the quartz, sapphire, and LAO substrates for 30 minute deposition ($\sim 0.4 \mu\text{m}$ thick) in both R- and T-modes, respectively, as a function of the

accelerating voltage. These TFPs are the ones showing the best CL brightness and efficiency values in this set of experiments. The saturation and decrease of efficiency after ~4 kV was apparent through most of the $Y_2O_3:Eu$ TFPs in the figures. The abrupt changes in T-mode CL efficiency were also observed in the graphs as previously shown in Figure 4.24(d). The $Y_2O_3:Eu$ TFPs measured in R-mode showed higher CL efficiencies than the $Y_2O_3:Eu$ TFPs measured in T-mode.

Summary

In order to investigate the effects of the surface roughness on the luminance properties of TFPs, $Y_2O_3:Eu$ TFPs were deposited on diamond-coated silicon substrates. The $Y_2O_3:Eu$ TFPs on diamond-coated silicon substrates showed higher CL and PL brightnesses than those on bare silicon substrates throughout the deposition temperature range. The realization of the $Y_2O_3:Eu$ TFPs with higher brightness by means of a diamond buffer layer is mainly attributed to more outcoupling of light due to reduced internal reflection.

For more detailed studies on the effects of the TFP roughness with other fundamental parameters controlling the luminance properties of the TFPs, $Y_2O_3:Eu$ TFPs with different thicknesses and roughnesses were fabricated on various substrate materials using PLD under a controlled

experimental procedure. Microstructural and optical characterizations were conducted on those samples. Higher CL and PL brightness values were observed from the $\text{Y}_2\text{O}_3:\text{Eu}$ TFPs on quartz substrates in R-mode. The higher CL and PL brightness values of the $\text{Y}_2\text{O}_3:\text{Eu}$ TFPs on quartz substrates than those on sapphire, LAO, and silicon substrates, were mainly associated with the advantageous optical properties of the quartz substrate in terms of smaller refractive index and low absorption coefficient. Higher CL brightness of the $\text{Y}_2\text{O}_3:\text{Eu}$ TFPs on LAO substrates in the smaller film thickness region was mainly associated with the capability of better epitaxial growth of the $\text{Y}_2\text{O}_3:\text{Eu}$ TFPs on the LAO substrates than the $\text{Y}_2\text{O}_3:\text{Eu}$ TFPs on quartz, sapphire, and silicon substrates. TEM and Z-contrast STEM studies strongly support this explanation. The best CL brightness and efficiency was observed from the $\text{Y}_2\text{O}_3:\text{Eu}$ TFPs deposited for about 30 minutes of PLD (18000 laser pulses) in this study. The $\text{Y}_2\text{O}_3:\text{Eu}$ TFPs showed higher CL brightness and efficiency in R-mode than in T-mode.

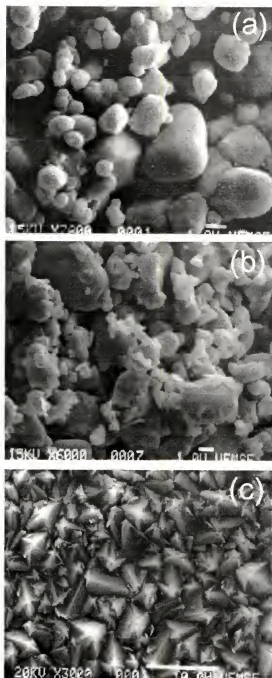
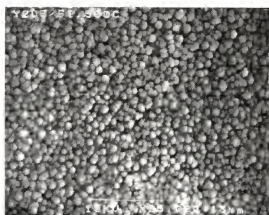
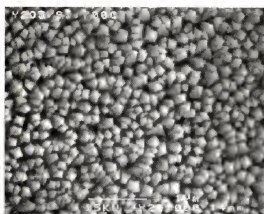


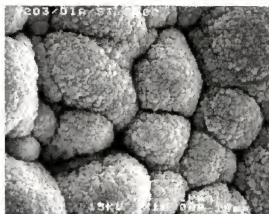
Figure 4.1. SEM micrographs of (a) bare $\text{Y}_2\text{O}_3\text{:Eu}$ powder particles, (b) sintered $\text{Y}_2\text{O}_3\text{:Eu}$ target at 1400°C for 24 hours after cold compaction, and (c) surface image of diamond film coated on silicon substrate.



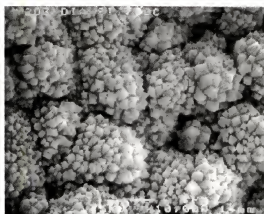
(a) 500°C, Si



(b) 700°C, Si



(c) 500°C, Diamond



(d) 700°C, Diamond

Figure 4.2. SEM micrographs of $\text{Y}_2\text{O}_3:\text{Eu}$ TFPs deposited on (100) silicon at the temperatures of (a) 500°C (b) 700°C ($\times 25000$) and diamond-coated silicon at the temperatures of (c) 500°C (d) 700°C ($\times 10000$).

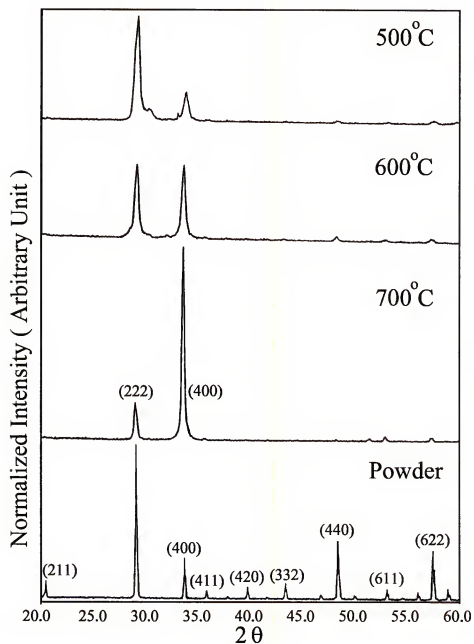


Figure 4.3. XRD patterns of $\text{Y}_2\text{O}_3:\text{Eu}$ TFPs deposited on (100) bare silicon substrates at 500, 600, 700°C temperatures, and powder.

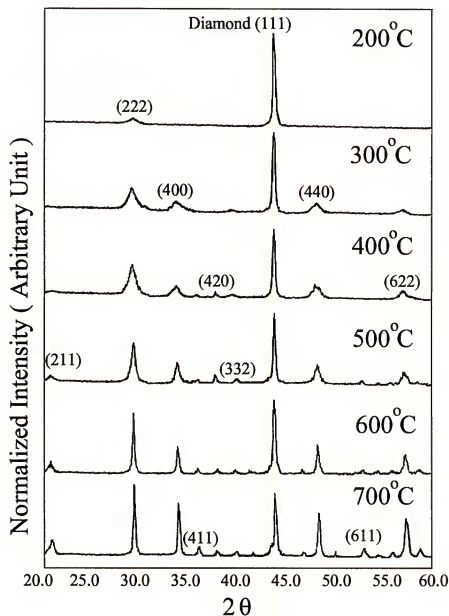


Figure 4.4. XRD patterns of $\text{Y}_2\text{O}_3:\text{Eu}$ TFPs deposited on diamond-coated (100) silicon substrates at the deposition temperatures of 200, 300, 400, 500, 600, and 700°C.

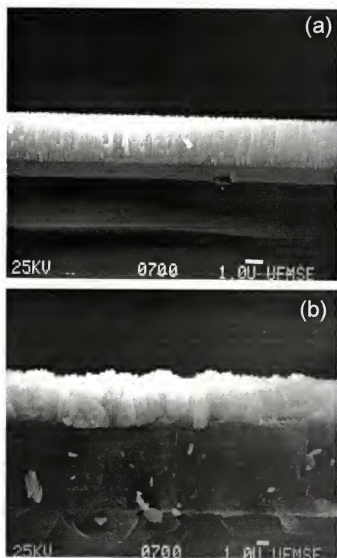


Figure 4.5. SEM Cross-sectional views of Y₂O₃:Eu TFPs deposited on (a) bare and (b) diamond-coated (100) silicon substrates at 700°C deposition temperature. Diamond layer is shown in between Y₂O₃:Eu film and Si substrate in figure (b).

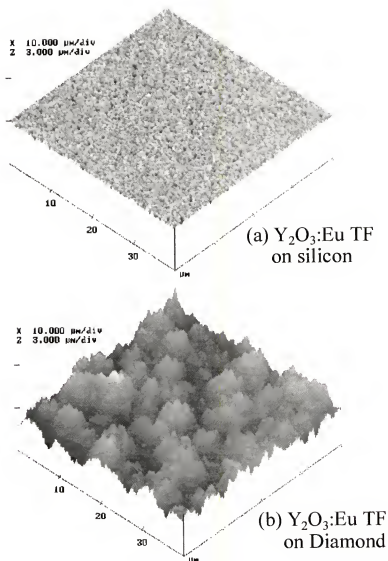


Figure 4.6. AFM micrographs showing morphologies of $\text{Y}_2\text{O}_3:\text{Eu}$ TFPs deposited on (a) bare and (b) diamond-coated silicon substrates at 700°C deposition temperature. TFP on diamond layer has ~ 8 times more RMS roughness.

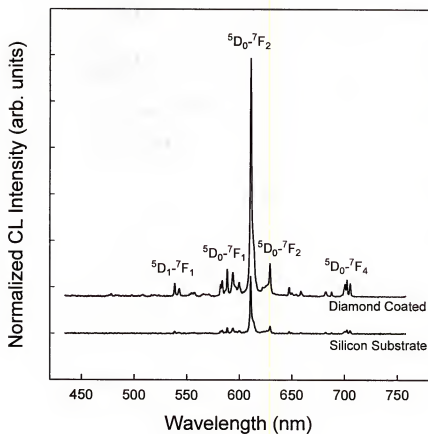


Figure 4.7. Normalized CL spectra recorded from $\text{Y}_2\text{O}_3:\text{Eu}$ TFPs deposited on bare (lower) and diamond-coated (upper) silicon substrates at 700°C deposition temperature. TFP on diamond layer shows more than 3 times higher CL brightness.

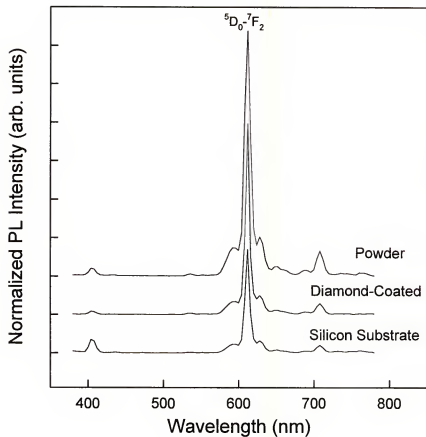


Figure 4.8. PL spectra recorded from $\text{Y}_2\text{O}_3:\text{Eu}$ TFPs deposited on bare (lower) and diamond-coated (middle) silicon substrates at 700°C deposition temperature compared to the PL spectrum of $\text{Y}_2\text{O}_3:\text{Eu}$ powder (upper). Scale is normalized.

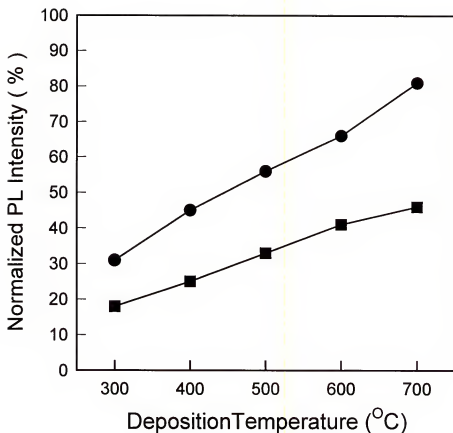


Figure 4.9. PL brightness of $\text{Y}_2\text{O}_3:\text{Eu}$ TFPs deposited on bare (lower) and diamond-coated (upper) silicon substrates as a function of deposition temperature from 300 to 700°C normalized by the PL brightness of $\text{Y}_2\text{O}_3:\text{Eu}$ powder layer on silicon. TFP on diamond layer shows up to ~80% PL brightness of that of the powder layer.

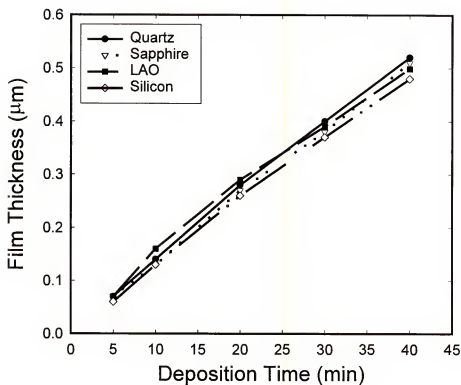


Figure 4.10. Increases in the film thickness of Y₂O₃:Eu TFPs deposited on quartz, sapphire, LAO, and silicon substrates with deposition time, showing very small difference among substrates which is believed to be induced by the experimental errors during the measurements due to different film morphologies.

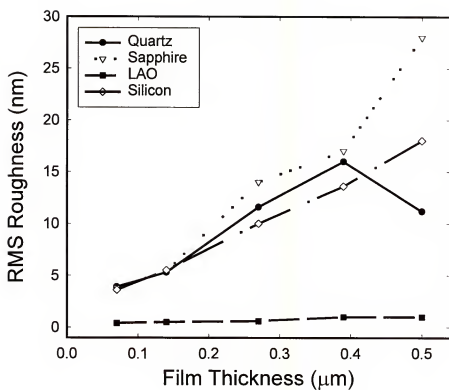


Figure 4.11. RMS roughness variation of Y₂O₃:Eu TFPs deposited on quartz, sapphire, LAO, and silicon substrates with film thickness.

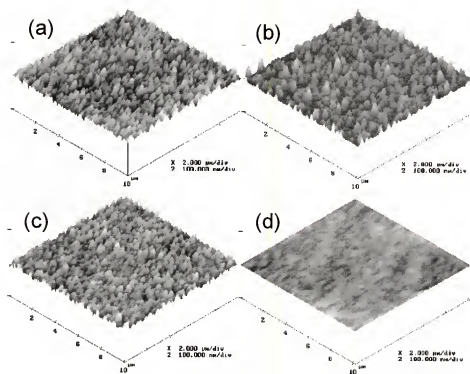


Figure 4.12. AFM micrographs of Y₂O₃:Eu TFPs deposited on (a) quartz, (b) sapphire, (c) silicon, and (d) LAO substrates for 6000 pulses (10 min, ~0.14 μm thick). Measured RMS roughness values are 5.30, 5.40, 0.50, and 5.50 nm, respectively.

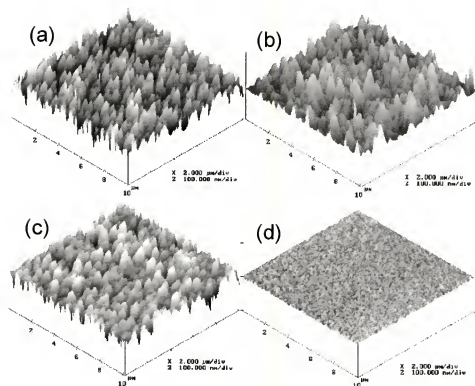


Figure 4.13. AFM micrographs of $\text{Y}_2\text{O}_3\text{:Eu}$ TFPs deposited on (a) quartz, (b) sapphire, (c) silicon, and (d) LAO substrates for 18000 pulses (30 min, $\sim 0.4 \mu\text{m}$ thick). Measured RMS roughness values are 16.00, 17.00, 13.60, and 1.00 nm, respectively.

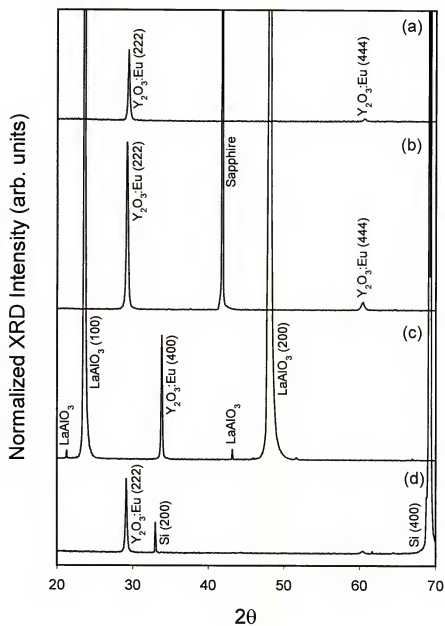


Figure 4.14. XRD patterns of Y₂O₃:Eu TFPs deposited on (a) quartz, (b) sapphire, (c) silicon, and (d) LAO substrates for 6000 pulses (10 min, ~0.14 μm thick).

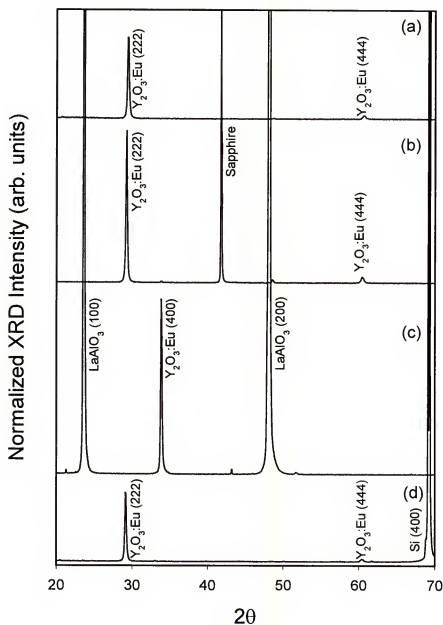


Figure 4.15. XRD patterns of Y₂O₃:Eu TFPs deposited on (a) quartz, (b) sapphire, (c) silicon, and (d) LAO substrates for 18000 pulses (30 min, ~0.4 μm thick).

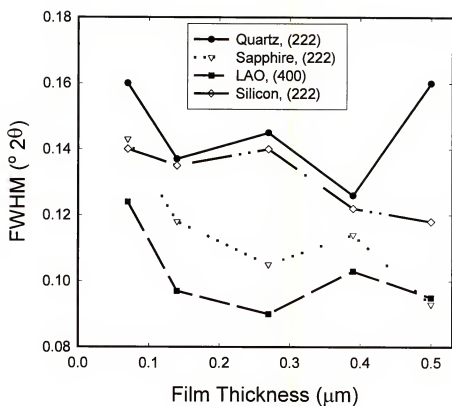


Figure 4.16. Full width half maximum (FWHM) values of $\text{Y}_2\text{O}_3:\text{Eu}$ TFPs with film thickness. (400) peaks are measured for the films on LAO but (222) for the films on other substrates.

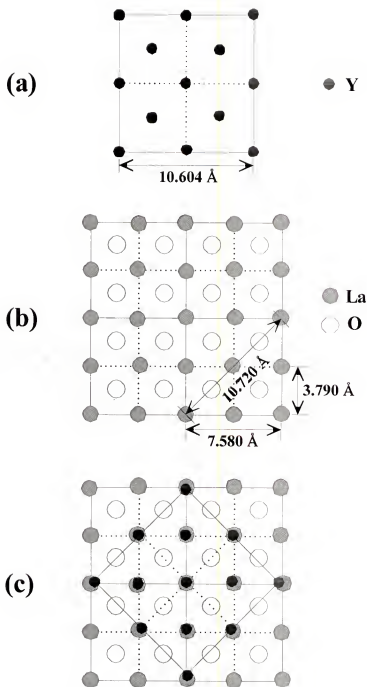


Figure 4.17. 2-dimensional schematic illustrations of (a) the unit cell size of $\text{Y}_2\text{O}_3:\text{Eu}$ TFP with a lattice parameter of 10.604 \AA , (b) the structure of LaAlO_3 substrate with a lattice parameter of 3.790 \AA , and (c) 45° rotational atomic stacking of $\text{Y}_2\text{O}_3:\text{Eu}$ TFP on LAO substrate which results in the single crystal growth with only 1.1% lattice mismatch.

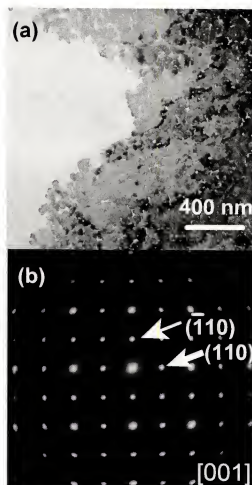


Figure 4.18. (a) Plan view TEM image and (b) corresponding selected area electron diffraction pattern of Y₂O₃:Eu TFP on LAO substrate, showing the formation of a good single crystalline film containing numerous voids. The electron projection is along the $[001]$ zone axis of the Y₂O₃:Eu crystalline thin film.

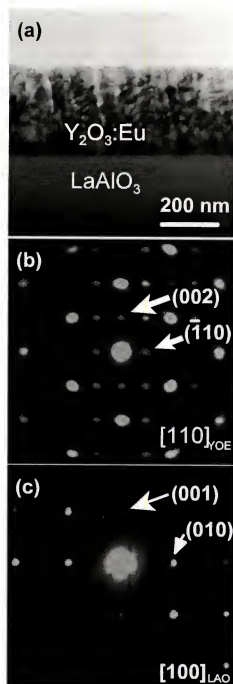


Figure 4.19. (a) Cross sectional view TEM image and corresponding selected area electron diffraction patterns of (b) $\text{Y}_2\text{O}_3:\text{Eu}$ TFP and (c) LAO substrate showing the orientation relationship to be $[110]_{\text{Y}_2\text{O}_3} // [100]_{\text{LaAlO}_3}$ and $[-110]_{\text{Y}_2\text{O}_3} // [010]_{\text{LaAlO}_3}$.

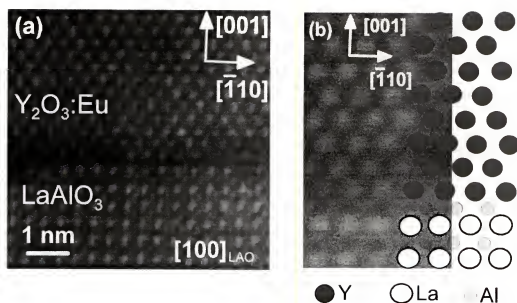


Figure 4.20. (a) Z-contrast STEM dark field image showing the atomically abrupt fil/substrate interface, and (b) higher magnification image showing clearly the Al terminated substrate, as shown in the schematic illustration together.

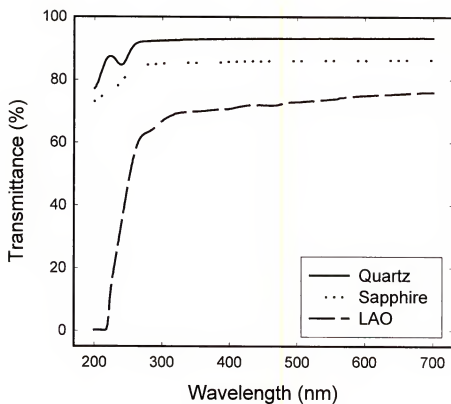


Figure 4.21. Transmittance properties of the quartz, sapphire, and LAO substrates measured using UV/VIS/NIR spectrometer in a range of 200-700 nm wavelength.

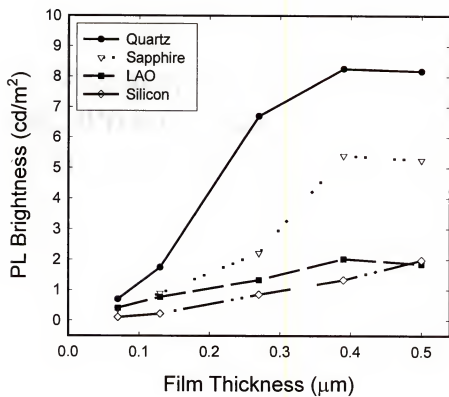


Figure 4.22. PL brightness of $\text{Y}_2\text{O}_3:\text{Eu}$ TFPs deposited on quartz, sapphire, LAO, and silicon substrates with film thickness excited by 254 nm UV radiation.

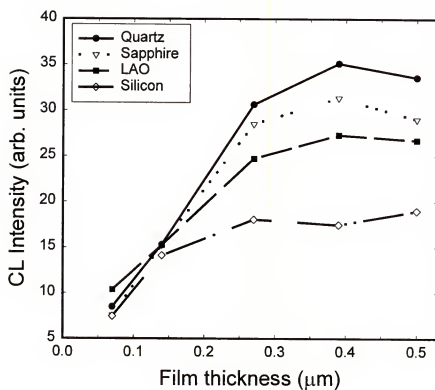


Figure 4.23. CL brightness of $\text{Y}_2\text{O}_3:\text{Eu}$ TFPs deposited on quartz, sapphire, LAO, and silicon substrates with film thickness excited by $0.1 \mu\text{A}/\text{cm}^2$ current density at 5 kV.

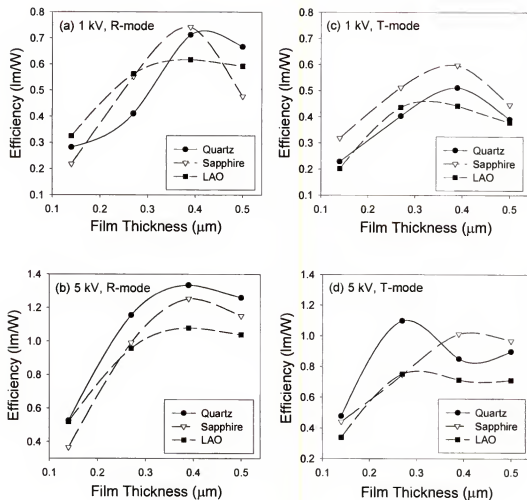


Figure 4.24. CL efficiency graphs obtained from $\text{Y}_2\text{O}_3:\text{Eu}$ TFPs deposited on quartz, sapphire, and LAO substrates as a function of film thickness at (a) 1 and (b) 5 kV in R-mode, and (c) 1 and (d) 5 kV in T-mode.

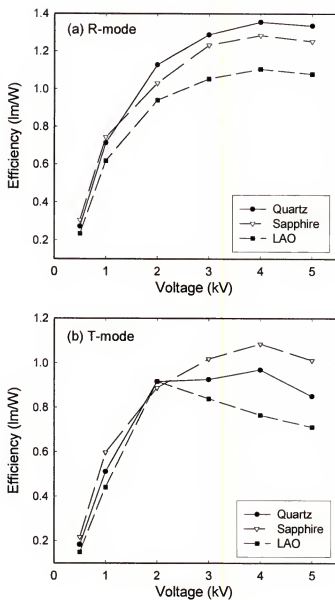


Figure 4.25. CL efficiency graphs of $\text{Y}_2\text{O}_3:\text{Eu}$ TFPs deposited on quartz, sapphire, and LAO substrates for 30 minutes ($\sim 0.4 \mu\text{m}$ thick) in both (a) R-mode and (b) T-mode as a function of accelerating voltage.

CHAPTER 5 MODELING

There have been intensive efforts to enhance the relatively low brightness of TFPs compared to that of powder phosphors by tailoring the surface roughness of the TFPs. The various methodologies include variation in processing conditions [Jon97a,b], modifying TFP's surface [Cho99, Lee98b, Sch93], and addition of a buffer layer between TFP and substrate [Cho98a,b]. Their experimental results showed that light trapping due to internal reflection from a smooth surface is significantly reduced as the surface becomes progressively rougher up to a certain level. Although this phenomenon is qualitatively understood well, there has been a lack of integrated analysis of the scattering effects of the propagating light on the brightness of the TFPs. Parameters which affect the brightness of TFPs include film thickness, optical interfaces, microstructure, surface roughness, substrate type, e-beam-solid interaction, and surface recombination rate. In general, these parameters are interrelated with complexity and cannot be varied independently. Thus, it is hard to quantitatively explain the experimental results. Moreover, classical theories based

on rectilinear propagation of the light cannot be used without gross simplifications, as the wavelength of the surface roughness is smaller than the wavelength of the emitted light.

As discussed in Chapter 2, if the dimensions of the facets of the crystallites are large compared with the wavelength of light, the reflectance of a surface in a given direction is determined entirely by geometrical optics and is only a function of the inclinations of the facets [Ben61]. As the dimensions of the facets becomes smaller than the wavelength of light, diffraction effects become more important, and the reflectance is a function of both the inclination and the size of the facets. As the dimensions of the facets become very small compared with the wavelength of light, the reflectance of the surface is determined almost entirely by diffraction effects [Ben61, Top79].

Some simplified models have been suggested to predict the brightness of the TFPs as a function of the effect of bulk and surface structure [Cho99, Jon99, Lee98b, Sch93]. However, their solutions include only a couple of affecting parameters mentioned above and do not take into account complex multiple scattering at the interfaces as well as beam-solid interactions. In order to overcome the deficiencies of the earlier work, a new model which

incorporates most of the affecting parameters mentioned above, especially including diffraction-based multiple light scatterings with different thicknesses of TFPs on various substrates as well as e-beam-solid interactions, has been developed. Therefore, the objective of this modeling is to understand the effects of the fundamental parameters controlling the luminance properties of TFPs and develop a general solution to predict thin film-related light emission properties, with a computer-based flexible theoretical model. This understanding and development of a predictable theoretical model will eventually lead to fabrication of TFPs for FEDs with optimum CL properties.

Assumptions for Modeling

The model of light emission from $Y_2O_3:Eu$ TFPs is based on the diffraction scattering of light from the various interfaces (air/film: interface 1, film/substrate: interface 2, and substrate/air: interface 3). Figure 5.1 (a) shows the spatial distribution of the energy reflected from a rough surface with the coordinates and angle notations based on diffraction scattering theory [Bec63, Top79]. The diffraction scattering theory explains two different scattering components of the reflected light when surface roughness is smaller or comparable to the wavelength of the

incident light, as expressed as,

$$f(\psi, \zeta; \theta, \varphi) = f_c(\psi, \zeta; \theta, \varphi) + f_{ic}(\psi, \zeta; \theta, \varphi) \quad (5.1)$$

where f is 2-directional reflection coefficient, f_c is coherent (specular) component which reflects at an angle equal to the incident angle, f_{ic} is incoherent (diffuse) component which scatters in a space with some fraction of light propagating in the specular direction along with the specularly reflected light, and the definitions of the four angles $(\psi, \zeta, \theta, \varphi)$ are illustrated in Figure 5.1(a). The f_c depends on the incident angle (ψ) , the optical roughness (σ/λ) , and the solid angle $(\Delta\Omega_i)$ containing the incident energy, while the f_{ic} depends not only on ψ and σ/λ but also on the direction in which the energy is reflected (θ, φ) and the ratio of the peak distance in Figure 5.1(b) to the wavelength of the light (a/λ) [Top79].

The generated light from each activator in the TFP, encounters absorption, diffuse and specular reflection, and diffuse and specular transmittance effects, as it traverses across the TFP. The observed brightness is the total sum intensity of the light escaping out of film surface (R-mode) or substrate surface (T-mode) through the multiple scattering occurring at the interfaces of 1, 2, and 3. Since the roughness of the interfaces 2 and 3 are very low, the

diffuse effects from these interfaces are not considered. Also, the scattering effects at the grain boundaries are neglected, because significant changes in the refractive index are not expected to occur at the grain boundaries.

Surface Roughness of Film

A sine waveform roughness is assumed for the shape of the surface roughness of the TFPs as depicted in Figure 5.1(b). From the definition of RMS roughness (σ), the relationship between the roughness height (h) and σ can be derived as

$$\sigma = \left[\frac{1}{N} \sum_{n=1}^N (h_i - \bar{h})^2 \right]^{\frac{1}{2}} = \left[\int_0^{2\pi} \frac{A^2 \sin^2 \theta d\theta}{2\pi} \right]^{\frac{1}{2}} = \frac{A}{\sqrt{2}} = \frac{h}{2\sqrt{2}}, \text{ or } h = 2\sqrt{2}\sigma \quad (5.2)$$

where \bar{h} is the average roughness height with N measurements, A is the amplitude of the sine waveform roughness, and θ is the angle of the propagating light with respect to normal.

Intensity Change by an Angle Change

By definition of the solid angle (Ω) with a surface area of s in a cone of emission, the Ω is defined as

$$\Omega = \frac{s}{r^2} = \frac{2\pi r h}{r^2} = \frac{2\pi r(r - r \cos \theta)}{r^2} = 2\pi(1 - \cos \theta) \quad (5.3)$$

where r is the radius of the cone of emission, as illustrated in Figure 5.2. Then, the derivative of the Ω (the solid angle change: $d\Omega$) is the change of the cone of emission, as defined as

$$d\Omega = 2\pi \sin\theta d\theta . \quad (5.4)$$

When light is generated in the activator center, the intensity of light (I_0) in all directions has 4π solid angle. This defines the intensity of the light of an unit solid angle as $I_0/4\pi$. Therefore, the intensity change (dI_0) by an angular element ($d\theta$) is

$$dI_0 = \frac{I_0}{4\pi} d\Omega = \frac{I_0}{4\pi} \cdot 2\pi \sin\theta d\theta = \frac{I_0}{2} \cdot \sin\theta d\theta . \quad (5.5)$$

Scattering of Light at Interface

When propagating light scatters at the film interface having a RMS roughness of σ , the light is divided into four different components, such as T_s , T_d , R_s , and R_d , as illustrated in Figure 5.3. From the relationship defined by Beckmann et al. [Bec63] and Toporetts [Top79], the intensity of the specular reflection (I_{R_s}) can be defined as

$$I_{R_s} = I_{R_0} \exp \left[- \left(\frac{2\sqrt{2}\pi\sigma}{\lambda} \cos\theta \right)^2 \right] \quad (5.6)$$

where I_{R0} is the intensity of the internally reflecting light when $\sigma=0$, λ is the wavelength of the generated light in the film, and θ is the angle of propagating light with respect to normal.

Figure 5.4 illustrates the assumptions for the diffuse component of the propagating light after being generated from an activator. When the light generated from an activator scatters at the interface 1, the light reflected back to the film with an angle less than θ_c ($R_d < \theta_c$) will transmit into the substrate, and the light reflected back to the film with an angle greater than θ_c ($R_d > \theta_c$) will internally reflect with another angle β , in addition to R_s . For this case, the intensity of the total internal reflection when $\sigma \neq 0$ ($I_{R\sigma \neq 0}$) is reduced by the presence of the intensity of the diffuse transmittance (I_{Td}) which is the light escaping from the film to air due to surface roughness. Then, $I_{R\sigma \neq 0}$ is defined as the sum intensity of the specularly reflected light (I_{Rs}) and the diffusely reflecting light (I_{Rd}):

$$I_{R\sigma \neq 0} = I_{R0} - I_{Td} = I_{Rs} + I_{Rd} . \quad (5.7)$$

I_{Td} is a part of the I_{Rd} since the internal reflection is reduced by the existing surface roughness, thus it is defined as

$$I_{Td} = \eta I_{Rd} \quad (5.8)$$

where η is a constant between 0 and 1. Therefore, I_{Td} is an additional contributor to the total sum intensity of the light from the film side, in addition to the intensity of specularly transmitted light (I_{Ts}) which directly escapes from the film when θ is smaller than the critical angle, θ_c .

Equation (5.7) can be expressed for I_{Rd} by subtracting the I_{Rs} and I_{Td} from I_{R0} ,

$$I_{Rd} = I_{R0} - I_{Rs} - I_{Td} . \quad (5.9)$$

According to Beckmann et al.[Bec63] and Toporets [Top79], the I_{Rd} is also defined as

$$I_{Rd} = I_{R0} \left[1 - \exp \left[- \left(\frac{2\sqrt{2}\pi\sigma}{\lambda} \cos\theta \right)^2 \right] \right] . \quad (5.10)$$

I_{Rd} is assumed to be uniformly distributed in all directions and is expressed again using Equations (5.8)-(5.10) as

$$I_{Rd} + I_{Td} = I_{R0} - I_{Rs} = I_{R0} - I_{R0} \exp \left[- \left(\frac{2\sqrt{2}\pi\sigma}{\lambda} \cos\theta \right)^2 \right] \quad (5.11)$$

$$I_{Rd} + \eta I_{Rd} = (1 + \eta) I_{Rd} = I_{R0} \left[1 - \exp \left[- \left(\frac{2\sqrt{2}\pi\sigma}{\lambda} \cos\theta \right)^2 \right] \right] \quad (5.12)$$

$$\therefore I_{R_d} = \frac{I_{R_0}}{1 + \eta} \left[1 - \exp \left[- \left(\frac{2\sqrt{2}\pi\sigma}{\lambda} \cos\theta \right)^2 \right] \right]. \quad (5.13)$$

The I_{R_d} in an unit solid angle in hemisphere is defined as

$$\frac{I_{R_d}}{2\pi} = \frac{I_{R_0}}{(1 + \eta)2\pi} \left[1 - \exp \left[- \left(\frac{2\sqrt{2}\pi\sigma}{\lambda} \cos\theta \right)^2 \right] \right]. \quad (5.14)$$

According to Equations (5.3) and (5.4), $d\Omega$ with an angular unit $d\beta$ is

$$d\Omega = 2\pi \sin\beta d\beta. \quad (5.15)$$

Therefore, the intensities of the diffusely reflected ($I_{R_d,\beta}$) and transmitted ($I_{T_d,\beta}$) light related to $d\Omega$ in Equation (5.15) are

$$I_{R_d,\beta} = \frac{I_{R_d}}{2\pi} d\Omega = \frac{I_{R_0}}{(\eta + 1)} \left[1 - \exp \left[- \left(\frac{2\sqrt{2}\pi\sigma}{\lambda} \cos\theta \right)^2 \right] \right] \sin\beta d\beta \quad (5.16)$$

$$I_{T_d,\beta} = \frac{\eta I_{R_0}}{(1 + \eta)} \left[1 - \exp \left[- \left(\frac{2\sqrt{2}\pi\sigma}{\lambda} \cos\theta \right)^2 \right] \right] \sin\beta d\beta. \quad (5.17)$$

Modeling of Specular Component of Light

The generated light from an activator which is located at a distance of x to the film surface with an intensity of I_0 propagates in all directions. A fraction of the light by changing the angular element, which is defined in Equation (5.5), can be specularly transmitted from film into air ($p_{1,2,3}$) and substrate ($q_{1,2,3}$) through multiple scattering between interfaces 1 and 2 during propagating upward and downward with a starting angle θ , as illustrated in Figures 5.5 (a)-(b), respectively. Some part of the light transmitted into substrate will be transmitted back into film through interface 2 and some other part of the light will be transmitted into air through interface 3, experiencing multiple scattering, as depicted in Figure 5.6(a). The light transmitted back from substrate will also experience multiple scattering in the film allowing transmittance into air and substrate again, as shown in Figure 5.6(b). The intensity of the transmitted light depends on transmittance and reflectivity properties at the interfaces 1 (T_1 and R_1 , respectively) and 2 (T_2 and R_2 , respectively), absorption coefficients of film (α_1) and substrate (α_2), and thicknesses of film (t_1) and substrate (t_2). More detailed mathematical derivations for the

expressions of the specular component of the propagating light are attached in Appendix A.

Light Propagating in Upward Direction

In Figure 5.5(a), the sum intensity of the specular components transmitted from film into air through the interface 1 ($P_1 = p_1 + p_2 + p_3 + \dots + p_\infty$) can be expressed as

$$P_1 = \sum_{i=1}^{\infty} p_i = \frac{\frac{I_0}{2} \sin \theta d \theta T_1(\theta) \exp\left(\frac{-\alpha_1 x}{\cos \theta}\right)}{1 - R_1(\theta) R_2(\theta) \exp\left(\frac{-2\alpha_1 t_1}{\cos \theta}\right) \exp\left[-\left(\frac{2\sqrt{2}\pi\sigma \cos \theta}{\lambda}\right)^2\right]}. \quad (5.18)$$

The same approach can be applied for the sum intensity of the specular components transmitted from film into substrate through the interface 2 ($Q_1 = q_1 + q_2 + q_3 + \dots + q_\infty$):

$$Q_1 = \sum_{i=1}^{\infty} q_i = \frac{\frac{I_0}{2} \sin \theta d \theta R_1(\theta) T_2(\theta) \exp\left(\frac{-\alpha_1(t_1 + x)}{\cos \theta}\right) \exp\left[-\left(\frac{2\sqrt{2}\pi\sigma \cos \theta}{\lambda}\right)^2\right]}{1 - R_1(\theta) R_2(\theta) \exp\left(\frac{-2\alpha_1 t_1}{\cos \theta}\right) \exp\left[-\left(\frac{2\sqrt{2}\pi\sigma \cos \theta}{\lambda}\right)^2\right]}. \quad (5.19)$$

Light Propagating in Downward Direction

In Figure 5.5(b), the sum intensity of the specular components transmitted from film into air through the interface 1 ($P_2 = p_1 + p_2 + p_3 + \dots + p_\infty$) can be expressed as

$$P_2 = \sum_{i=1}^{\infty} P_i = \frac{\frac{I_0}{2} \sin \theta d \theta R_2(\theta) T_1(\theta) \exp\left(\frac{-\alpha_1(2t_1 - x)}{\cos \theta}\right)}{1 - R_1(\theta) R_2(\theta) \exp\left(\frac{-2\alpha_1 t_1}{\cos \theta}\right) \exp\left[-\left(\frac{2\sqrt{2}\pi\sigma \cos \theta}{\lambda}\right)^2\right]}. \quad (5.20)$$

The same can be applied for the sum intensity of the specular components transmitted from film into substrate through the interface 2 ($Q_2 = q_1 + q_2 + q_3 + \dots + q_{\infty}$):

$$Q_2 = \sum_{i=1}^{\infty} q_i = \frac{\frac{I_0}{2} \sin \theta d \theta T_2(\theta) \exp\left(\frac{-\alpha_1(t_1 - x)}{\cos \theta}\right)}{1 - R_1(\theta) R_2(\theta) \exp\left(\frac{-2\alpha_1 t_1}{\cos \theta}\right) \exp\left[-\left(\frac{2\sqrt{2}\pi\sigma \cos \theta}{\lambda}\right)^2\right]}. \quad (5.21)$$

Light Transmitted from Film into Substrate

In Figure 5.6(a), the sum intensity of the specular components transmitted back from substrate into film through the interface 2 ($P_3 = p_1 + p_2 + p_3 + \dots + p_{\infty}$) can be expressed as

$$P_3 = \sum_{i=1}^{\infty} P_i = \frac{I_1 R_3(\theta) T_2(\theta) \exp\left(\frac{-2\alpha_2 t_2}{\cos \gamma}\right)}{1 - R_2(\theta) R_3(\theta) \exp\left(\frac{-2\alpha_2 t_2}{\cos \gamma}\right)} \quad (5.22)$$

where I_1 is the intensity of the light just after entered into the substrate through the interface 2, and γ is the refracted angle in the substrate corresponding to the incident angle θ in the film. The same method can be applied for the sum intensity of the specular components transmitted

from substrate into air through the interface 3 ($Q_3 = q_1 + q_2 + q_3 + \dots + q_\infty$) :

$$Q_3 = \sum_{i=1}^{\infty} q_i = \frac{I_1 T_3(\theta) \exp\left(\frac{-a_2 t_2}{\cos \gamma}\right)}{1 - R_2(\theta) R_3(\theta) \exp\left(\frac{-2a_2 t_2}{\cos \gamma}\right)} . \quad (5.23)$$

Light Transmitted Back from Substrate into Film

Figure 5.6(b) shows the case of light transmitting back from substrate into film (I_2). The light with an intensity of I_2 will also experience multiple scattering in the film. Then, the sum intensity of the specular components transmitted from film into air through the interface 1 ($P_4 = p_1 + p_2 + p_3 + \dots + p_\infty$) can be expressed as

$$P_4 = \sum_{i=1}^{\infty} p_i = \frac{I_2 T_1(\theta) \exp\left(\frac{-a_1 t_1}{\cos \theta}\right)}{1 - R_1(\theta) R_2(\theta) \exp\left(\frac{-2a_1 t_1}{\cos \theta}\right) \exp\left[-\left(\frac{2\sqrt{2}\pi\sigma \cos \theta}{\lambda}\right)^2\right]} . \quad (5.24)$$

The same can be applied for the sum intensity of the specular components transmitted into substrate ($Q_4 = q_1 + q_2 + q_3 + \dots + q_\infty$) :

$$Q_4 = \sum_{i=1}^{\infty} q_i = \frac{I_2 R_1(\theta) T_2(\theta) \exp\left(\frac{-2a_1 t_1}{\cos \theta}\right) \exp\left[-\left(\frac{2\sqrt{2}\pi\sigma \cos \theta}{\lambda}\right)^2\right]}{1 - R_1(\theta) R_2(\theta) \exp\left(\frac{-2a_1 t_1}{\cos \theta}\right) \exp\left[-\left(\frac{2\sqrt{2}\pi\sigma \cos \theta}{\lambda}\right)^2\right]} . \quad (5.25)$$

Summation of Intensities

It is required to consider all the above four cases together to derive the expressions for the added specular components, as illustrated in Figure 5.7. The sum intensity of the light transmitted from film into substrate for the 1st time (FS_1) is the sum of Q_1 and Q_2 as defined as

$$FS_1 = \frac{\frac{I_0}{2} \sin \theta d\theta T_2(\theta) \left[R_1(\theta) \exp\left(\frac{-\alpha_1(t_1+x)}{\cos \theta}\right) \exp\left[-\left(\frac{2\sqrt{2}\pi\sigma \cos \theta}{\lambda}\right)^2\right] + \exp\left(\frac{-\alpha_1(t_1-x)}{\cos \theta}\right) \right]}{1 - R_1(\theta)R_2(\theta) \exp\left(\frac{-2\alpha_1 t_1}{\cos \theta}\right) \exp\left[-\left(\frac{2\sqrt{2}\pi\sigma \cos \theta}{\lambda}\right)^2\right]}. \quad (5.26)$$

Next, the sum intensity of light transmitted back from the substrate into film for the 1st time (SF_1) is the case of P_3 when I_1 is FS_1 as shown below

$$SF_1 = FS_1 \cdot \frac{R_3(\theta)T_2(\theta) \exp\left(\frac{-2\alpha_2 t_2}{\cos \gamma}\right)}{1 - R_2(\theta)R_3(\theta) \exp\left(\frac{-2\alpha_2 t_2}{\cos \gamma}\right)}. \quad (5.27)$$

Then, the sum intensity of the light transmitted from film into substrate for the n^{th} time (FS_n) is the case of Q_4 when I_2 is SF_{n-1} as defined as

$$FS_n = FS_1 \cdot \left[\frac{R_3(\theta)T_2(\theta) \exp\left(\frac{-2\alpha_2 t_2}{\cos \gamma}\right)}{1 - R_2(\theta)R_3(\theta) \exp\left(\frac{-2\alpha_2 t_2}{\cos \gamma}\right)} \right]^{n-1} \cdot \left[\frac{R_1(\theta)T_2(\theta) \exp\left(\frac{-2\alpha_1 t_1}{\cos \theta}\right) \exp\left[-\left(\frac{2\sqrt{2}\pi\sigma \cos \theta}{\lambda}\right)^2\right]}{1 - R_1(\theta)R_2(\theta) \exp\left(\frac{-2\alpha_1 t_1}{\cos \theta}\right) \exp\left[-\left(\frac{2\sqrt{2}\pi\sigma \cos \theta}{\lambda}\right)^2\right]} \right]^{n-1}. \quad (5.28)$$

The sum intensity of light transmitted back from the substrate into film for the n^{th} time (SF_n) is the case of P_3 when I_1 is FS_n as shown below

$$SF_n = FS_1 \cdot \left[\frac{R_3(\theta)T_2(\theta)\exp\left(\frac{-2a_2t_2}{\cos\gamma}\right)}{1 - R_2(\theta)R_3(\theta)\exp\left(\frac{-2a_2t_2}{\cos\gamma}\right)} \right]^n \cdot \left[\frac{R_1(\theta)T_2(\theta)\exp\left(\frac{-2a_1t_1}{\cos\theta}\right)\exp\left[-\left(\frac{2\sqrt{2}\pi\sigma\cos\theta}{\lambda}\right)^2\right]}{1 - R_1(\theta)R_2(\theta)\exp\left(\frac{-2a_1t_1}{\cos\theta}\right)\exp\left[-\left(\frac{2\sqrt{2}\pi\sigma\cos\theta}{\lambda}\right)^2\right]} \right]^{n-1} \quad (5.29)$$

The relationship simply follows as $FS_1=Q_1+Q_2$, $FS_2=Q_4$ when $I_2=SF_1$, $FS_3=Q_4$ when $I_2=SF_2$, $FS_4=Q_4$ when $I_2=SF_3, \dots$, $FS_n=Q_4$ when $I_2=SF_{n-1}$, and $SF_1=P_3$ when $I_1=FS_1$, $SF_2=P_3$ when $I_1=FS_2$, $SF_3=P_3$ when $I_1=FS_3$, $SF_4=P_3$ when $I_1=FS_4, \dots$, $SF_n=P_3$ when $I_1=FS_n$. Therefore, the total intensities of the light specularly transmitted from film into substrate ($FS_{\theta} = \sum Q_{1,2,4}$) and of the light transmitted back from substrate into film ($SF_{\theta} = \sum P_3$), started with a propagation angle of θ are

$$FS_{\theta} = \frac{FS_1}{1 - \left[\frac{R_3(\theta)T_2(\theta)\exp\left(\frac{-2a_2t_2}{\cos\gamma}\right)}{1 - R_2(\theta)R_3(\theta)\exp\left(\frac{-2a_2t_2}{\cos\gamma}\right)} \right] \cdot \left[\frac{R_1(\theta)T_2(\theta)\exp\left(\frac{-2a_1t_1}{\cos\theta}\right)\exp\left[-\left(\frac{2\sqrt{2}\pi\sigma\cos\theta}{\lambda}\right)^2\right]}{1 - R_1(\theta)R_2(\theta)\exp\left(\frac{-2a_1t_1}{\cos\theta}\right)\exp\left[-\left(\frac{2\sqrt{2}\pi\sigma\cos\theta}{\lambda}\right)^2\right]} \right]} \quad (5.30)$$

$$SF_{\theta} = FS_{\theta} \cdot \left[\frac{R_3(\theta)T_2(\theta)\exp\left(\frac{-2a_2t_2}{\cos\gamma}\right)}{1 - R_2(\theta)R_3(\theta)\exp\left(\frac{-2a_2t_2}{\cos\gamma}\right)} \right] \quad (5.31)$$

Finally, the total intensity of light escaping from film to air through the interface 1 (TF_{s_0}) (R-mode) is the sum of $\sum P_1$, $\sum P_2$, and $\sum P_4$, and the total intensity of the light escaping from substrate to air through interface 3 (TS_{s_0}) (T-mode) started with a propagation angle of θ , is $\sum Q_3$, as expressed as

$$TF_{s_0} = \frac{T_1(\theta) \left[\frac{I_0}{2} \sin \theta \exp\left(\frac{-\alpha_1 x}{\cos \theta}\right) + \frac{I_0}{2} \sin \theta R_2(\theta) \exp\left(\frac{-\alpha_1(2t_1 - x)}{\cos \theta}\right) + SF_{\theta} \exp\left(\frac{-\alpha_1 t_1}{\cos \theta}\right) \right]}{1 - R_1(\theta) R_2(\theta) \exp\left(\frac{-2\alpha_1 t_1}{\cos \theta}\right) \exp\left[-\left(\frac{2\sqrt{2}\pi\sigma \cos \theta}{\lambda}\right)^2\right]} \quad (5.32)$$

$$TS_{s_0} = FS_{\theta} \cdot \frac{T_3(\theta) \exp\left(\frac{-\alpha_2 t_2}{\cos \gamma}\right)}{1 - R_2(\theta) R_3(\theta) \exp\left(\frac{-2\alpha_2 t_2}{\cos \gamma}\right)} \quad (5.33)$$

Integration of Specular Component

The total intensity of the generated light in the TFP with a thickness of t_1 is

$$I_{0_total} = \int_0^{t_1} I_0 dx = I_0 t_1 \quad (5.34)$$

assuming here that the whole thickness generates light.

Therefore, the total intensity of specular light escaping from film to air (Film_s: R-mode) or from substrate to air (Substrate_s: T-mode) after generated in the film of thickness t_1 , can be finalized as

$$Film_s = \int_0^{\frac{\pi}{2}} \int_0^1 TF_{s,\theta} dx d\theta \quad (5.35)$$

$$Substrate_s = \int_0^{\frac{\pi}{2}} \int_0^1 TS_{s,\theta} dx d\theta . \quad (5.36)$$

Modeling of Diffuse Component of Light

Figures 5.8(a)-(b) illustrates the two possible cases for the diffuse cases. The diffusely reflected light with an angle β originally started with an angle θ from an activator, can also propagate like a specular component of the light and this light can also specularly transmits from film into air ($p_{1,2,3}$) and substrate ($q_{1,2,3}$) during propagating multiply upward and downward directions depending on T_1 and T_2 , and R_1 and R_2 properties at the interfaces 1 and 2, respectively. More detailed mathematical derivations for the equations of the diffuse component of the propagating light are attached in Appendix A.

Light Propagating in Upward Direction (Diffuse)

In Figure 5.8(a), the p_1, p_2 , and p_3 are the intensities of the light propagating like a specular component after 1st scattering at interface 1. For this case, the sum intensity of the light transmitted from film into air through the interface 1 initiated by the 1st diffuse reflection ($P_s =$

$p_1 + p_2 + p_3 + \dots + p_m$ is

$$P_3 = \frac{\frac{I_0}{2} \sin \theta d \theta \exp\left(\frac{-a_1 x}{\cos \theta}\right) R_1(\theta) \left(\frac{1}{1+\eta}\right) \left[1 - \exp\left[-\left(\frac{2\sqrt{2}\pi\sigma}{\lambda} \cos \theta\right)^2\right]\right] \sin \beta d \beta R_2(\beta) T_1(\beta) \exp\left(\frac{-2a_1 t_1}{\cos \beta}\right)}{1 - R_1(\beta) R_2(\beta) \exp\left(\frac{-2a_1 t_1}{\cos \beta}\right)} \quad (5.37)$$

The same approach can be applied for the sum intensity of the light transmitted from film into substrate ($Q_5 = q_1 + q_2 + q_3 + \dots + q_m$) propagating like a specular component initiated by the 1st diffuse reflection at interface 1:

$$Q_5 = \frac{\frac{I_0}{2} \sin \theta d \theta \exp\left(\frac{-a_1 x}{\cos \theta}\right) R_1(\theta) \left(\frac{1}{1+\eta}\right) \left[1 - \exp\left[-\left(\frac{2\sqrt{2}\pi\sigma}{\lambda} \cos \theta\right)^2\right]\right] \sin \beta d \beta T_2(\beta) \exp\left(\frac{-a_1 t_1}{\cos \beta}\right)}{1 - R_1(\beta) R_2(\beta) \exp\left(\frac{-2a_1 t_1}{\cos \beta}\right)} \quad (5.38)$$

Therefore, the intensity of the diffuse transmittance from film into air by upward propagation (I_{Td_up}) can be derived as

$$I_{Td_up} = \frac{\frac{I_0}{2} \sin \theta d \theta \exp\left(\frac{-a_1 x}{\cos \theta}\right) R_1(\theta) \left(\frac{\eta}{1+\eta}\right) \left[1 - \exp\left[-\left(\frac{2\sqrt{2}\pi\sigma}{\lambda} \cos \theta\right)^2\right]\right]}{1 - R_1(\theta) \exp\left[-\left(\frac{2\sqrt{2}\pi\sigma}{\lambda} \cos \theta\right)^2\right] R_2(\theta) \exp\left(\frac{-2a_1 t_1}{\cos \theta}\right)} \quad (5.39)$$

Light Propagating in Downward Direction (Diffuse)

In Figure 5.8(b), the p_1 , p_2 , and p_3 are the intensities of the light propagating like a specular component after

reflected at interface 2 and then the 1st scattering at interface 1. For this case, the sum intensity of the light transmitted into air initiated by the 1st diffuse reflection ($P_6 = p_1 + p_2 + p_3 + \dots + p_\infty$) is

$$P_6 = \frac{\frac{I_0}{2} \sin \theta d \theta \exp\left(\frac{-a_1(2t_1 - x)}{\cos \theta}\right) R_2(\theta) R_1(\theta) \left(\frac{1}{1 + \eta}\right) \left[1 - \exp\left[-\left(\frac{2\sqrt{2}\pi\sigma}{\lambda} \cos \theta\right)^2\right]\right] \sin \beta d \beta R_2(\beta) T_1(\beta) \exp\left(\frac{-2a_1 t_1}{\cos \beta}\right)}{1 - R_1(\beta) R_2(\beta) \exp\left(\frac{-2a_1 t_1}{\cos \beta}\right)} \quad (5.40)$$

The same approach can be applied for the sum intensity of all the light transmitted into substrate through the interface 2 ($Q_6 = q_1 + q_2 + q_3 + \dots + q_\infty$) propagating like a specular component initiated by the 1st diffuse reflection at interface 1:

$$Q_6 = \frac{\frac{I_0}{2} \sin \theta d \theta \exp\left(\frac{-a_1(t_1 - x)}{\cos \theta}\right) R_2(\theta) R_1(\theta) \left(\frac{1}{1 + \eta}\right) \left[1 - \exp\left[-\left(\frac{2\sqrt{2}\pi\sigma}{\lambda} \cos \theta\right)^2\right]\right] \sin \beta d \beta T_2(\beta) \exp\left(\frac{-a_1 t_1}{\cos \beta}\right)}{1 - R_1(\beta) R_2(\beta) \exp\left(\frac{-2a_1 t_1}{\cos \beta}\right)} \quad (5.41)$$

Therefore, the diffuse transmittance from film into air by downward propagation (I_{Td_down}) can be derived as

$$I_{Td_down} = \frac{\frac{I_0}{2} \sin \theta d \theta \exp\left(\frac{-a_1(2t_1 - x)}{\cos \theta}\right) R_2(\theta) R_1(\theta) \left(\frac{\eta}{1 + \eta}\right) \left[1 - \exp\left[-\left(\frac{2\sqrt{2}\pi\sigma}{\lambda} \cos \theta\right)^2\right]\right]}{1 - R_1(\theta) \exp\left[-\left(\frac{2\sqrt{2}\pi\sigma}{\lambda} \cos \theta\right)^2\right] R_2(\theta) \exp\left(\frac{-2a_1 t_1}{\cos \theta}\right)} \quad (5.42)$$

Summation of Intensities (Diffuse)

The sum intensity of the diffuse light transmitted from film into substrate for the 1st time (FS_{1d}) is the sum of Q_5 and Q_6 :

$$FS_{1d} = \frac{\frac{I_0}{2} \sin \theta d \theta R_1(\theta) \left(\frac{1}{1+\eta} \right) \left[1 - \exp \left[- \left(\frac{2\sqrt{2}\pi\sigma}{\lambda} \cos \theta \right)^2 \right] \right] \sin \beta d \beta T_2(\beta) \exp \left(\frac{-\alpha_1 t_1}{\cos \beta} \right) \left[\exp \left(\frac{-\alpha_1 x}{\cos \theta} \right) + \exp \left(\frac{-\alpha_1 (t_1 - x)}{\cos \theta} \right) R_2(\theta) \right]}{1 - R_1(\beta) R_2(\beta) \exp \left(\frac{-2\alpha_1 t_1}{\cos \beta} \right)} \quad (5.43)$$

This equation leads to the sum intensity of the diffuse light transmitted from film into substrate (FS_{d_β}) and transmitted back from substrate into film (SF_{d_β}) with an angle β :

$$FS_{d_\beta} = \frac{FS_{1d}}{1 - \left[\frac{R_3(\beta) T_2(\beta) \exp \left(\frac{-2\alpha_2 t_2}{\cos \phi} \right)}{1 - R_2(\beta) R_3(\beta) \exp \left(\frac{-2\alpha_2 t_2}{\cos \phi} \right)} \right] \cdot \left[\frac{R_1(\beta) T_2(\beta) \exp \left(\frac{-2\alpha_1 t_1}{\cos \beta} \right) \exp \left[- \left(\frac{2\sqrt{2}\pi\sigma \cos \beta}{\lambda} \right)^2 \right]}{1 - R_1(\beta) R_2(\beta) \exp \left(\frac{-2\alpha_1 t_1}{\cos \beta} \right) \exp \left[- \left(\frac{2\sqrt{2}\pi\sigma \cos \beta}{\lambda} \right)^2 \right]} \right]} \quad (5.44)$$

$$SF_{d_\beta} = FS_{d_\beta} \cdot \left[\frac{R_3(\beta) T_2(\beta) \exp \left(\frac{-2\alpha_2 t_2}{\cos \phi} \right)}{1 - R_2(\beta) R_3(\beta) \exp \left(\frac{-2\alpha_2 t_2}{\cos \phi} \right)} \right] \quad (5.45)$$

where ϕ is the refraction angle in the substrate corresponding to the angle β in the film.

Therefore, the total sum intensities of the diffuse components of the light transmitted from film into air (TF_{d_β}) (R-mode), and transmitted from substrate into air (TS_{d_β}) (T-mode) with an angle β are:

$$TF_{d_\beta} = P_5 + P_6 + SF_{d_\beta} \cdot \frac{T_1(\beta) \exp\left(\frac{-\alpha_1 t_1}{\cos \beta}\right)}{1 - R_1(\beta) R_2(\beta) \exp\left(\frac{-2\alpha_1 t_1}{\cos \beta}\right) \exp\left[-\left(\frac{2\sqrt{2}\pi\sigma \cos \beta}{\lambda}\right)^2\right]} \quad (5.46)$$

$$TS_{d_\beta} = FS_{d_\beta} \cdot \frac{T_3(\beta) \exp\left(\frac{-\alpha_2 t_2}{\cos \phi}\right)}{1 - R_2(\beta) R_3(\beta) \exp\left(\frac{-2\alpha_2 t_2}{\cos \phi}\right)} \quad (5.47)$$

Finally, The total intensity of the diffuse light out of film into air (TF_{d_θ}) started with a propagation angle θ is the sum of I_{Td_up} , I_{Td_down} , and the integration of TF_{d_β} from 0 to $\pi/2$, and the total intensity of the diffuse light out of substrate into air (TS_{d_θ}) starting with an angle θ is the integration of TS_{d_β} from 0 to $\pi/2$:

$$TF_{d_\theta} = IT_{d_up} + IT_{d_down} + \int_0^{\pi/2} TF_{d_\beta} d\beta \quad (5.48)$$

$$TS_{d_\theta} = \int_0^{\pi/2} TS_{d_\beta} d\beta \quad (5.49)$$

Integration of Diffuse Component

The total generated light in a TFP with a thickness of t_1 is defined in Equation (5.34), assuming that the whole thickness generates light. Therefore, the total intensity of diffuse light escaping from film into air (Film_d: R-mode) or from substrate into air (Substrate_d: T-mode) after being generated in the film of thickness t_1 , can be finalized as

$$Film_d = \int_0^{\frac{\pi}{2}} \int_0^{t_1} TF_{d,\theta} dx d\theta \quad (5.50)$$

$$Substrate_d = \int_0^{\frac{\pi}{2}} \int_0^{t_1} TS_{d,\theta} dx d\theta . \quad (5.51)$$

Summation of Specular and Diffuse

The total sum intensities of the specular and diffuse from film into air (R-mode: I_{refl}), and from substrate into air (T-mode: I_{trans}) are

$$I_{refl} = Film_s + Film_d = \int_0^{\frac{\pi}{2}} \int_0^{t_1} TF_{s,\theta} dx d\theta + \int_0^{\frac{\pi}{2}} \int_0^{t_1} TF_{d,\theta} dx d\theta \quad (5.52)$$

$$I_{trans} = Substrate_s + Substrate_d = \int_0^{\frac{\pi}{2}} \int_0^{t_1} TS_{s,\theta} dx d\theta + \int_0^{\frac{\pi}{2}} \int_0^{t_1} TS_{d,\theta} dx d\theta . \quad (5.53)$$

It is worth noting that the integration of the model equations should be considered separately for three different regimes and added up together to get a total sum

intensity since the TFP system has three different optical interfaces resulting in different critical angles.

Therefore, each contributing part of the above equations can be written as

$$Film_{-s} = \int_0^{\theta_{c1}} \int_0^{\theta_1} TF_{s_{-\theta}} dx d\theta + \int_{\theta_{c1}}^{\theta_{c2}} \int_0^{\theta_1} TF_{s_{-\theta}} dx d\theta + \int_{\theta_{c2}}^{\frac{\pi}{2}} \int_0^{\theta_1} TF_{s_{-\theta}} dx d\theta \quad (5.54)$$

$$Film_{-d} = \int_0^{\theta_{c1}} \int_0^{\theta_1} TF_{d_{-\theta}} dx d\theta + \int_{\theta_{c1}}^{\theta_{c2}} \int_0^{\theta_1} TF_{d_{-\theta}} dx d\theta + \int_{\theta_{c2}}^{\frac{\pi}{2}} \int_0^{\theta_1} TF_{d_{-\theta}} dx d\theta \quad (5.55)$$

$$Substrate_{-s} = \int_0^{\theta_{c1}} \int_0^{\theta_1} TS_{s_{-\theta}} dx d\theta + \int_{\theta_{c1}}^{\theta_{c2}} \int_0^{\theta_1} TS_{s_{-\theta}} dx d\theta + \int_{\theta_{c2}}^{\frac{\pi}{2}} \int_0^{\theta_1} TS_{s_{-\theta}} dx d\theta \quad (5.56)$$

$$Substrate_{-d} = \int_0^{\theta_{c1}} \int_0^{\theta_1} TS_{d_{-\theta}} dx d\theta + \int_{\theta_{c1}}^{\theta_{c2}} \int_0^{\theta_1} TS_{d_{-\theta}} dx d\theta + \int_{\theta_{c2}}^{\frac{\pi}{2}} \int_0^{\theta_1} TS_{d_{-\theta}} dx d\theta . \quad (5.57)$$

Each integration part of the diffuse components above should also be considered separately in three different regimes of $0 < \beta < \theta_{c1}$, $\theta_{c1} < \beta < \theta_{c2}$, and $\theta_{c2} < \beta < \pi/2$, as did in the specular components.

Charge Carrier Diffusion and Concentration

There are other important physical processes to be included in the model. Since CL is excited by the electron beam, which interacts differently with the solid depending on material's characteristics, accelerating voltage, and current density, it is important to predict how many charge

carriers are created and involved in the luminescence process in a TFP. Since under the steady state condition the number of photons emitted is equal to the number of carriers released by the incident electrons that recombine (N), the diffusion equation defined in Equation (2.4) can be used to determine the carrier concentrations in a phosphor. The generation rate (G) and the interaction range of e-beam with the host matrix (R) defined by Kanaya-Okayama in Equation (2.1) are also applicable to solve the diffusion equation for N. For simplification, divide each term in Equation (2.4) by D and let

$$\sqrt{\frac{1}{Dr}} = m. \quad (5.58)$$

Then the equation can be rewritten as

$$\frac{d^2}{dx^2} N - m^2 N + \frac{G}{D} = 0, \quad (5.59)$$

where m is a constant. By combining Equations (2.1) and (2.5), G can be expressed as

$$G = \frac{i_0 V_0 Z^{0.89} \rho}{27.6 \Delta E M E_0^{1.67}}. \quad (5.60)$$

For simplification again, let

$$C = \frac{-i_0 V_0 Z^{0.89} \rho}{\Delta E 27.6 M E_0^{1.67} D} = -\frac{G}{D}. \quad (5.61)$$

Then the Equation (5.59) can be rewritten as

$$\frac{d^2}{dx^2} N - m^2 N = C. \quad (5.62)$$

Charge carriers can reach the activator centers outside the interaction range by diffusion. Thus two different regimes of interaction between carriers and TFP ($0 < x \leq R$ and $R < x \leq t_1$) should be considered in the model, as illustrated in Figure 5.9:

$$\frac{d^2}{dx^2} N_1 - m^2 N_1 = C \quad \text{for } 0 < x \leq R \quad (5.63)$$

$$\frac{d^2}{dx^2} N_2 - m^2 N_2 = 0 \quad \text{for } R < x \leq t_1. \quad (5.64)$$

The solutions for the N_1 and N_2 are the expressions for the number of e-h pairs created in a TFP for each regime above. The solutions are given as

$$N_1 = c_1 \exp(mx) + c_2 \exp(-mx) - \frac{C}{m^2} \quad (5.65)$$

$$N_2 = c_3 \exp(mx) + c_4 \exp(-mx) \quad (5.66)$$

where c_1 , c_2 , c_3 , and c_4 are constants. In order to determine c_1 , c_2 , c_3 , and c_4 , the required boundary conditions are

$$(1) \quad D \left(\frac{dN_1}{dx} \right)_{x=0} = (S \cdot N_1)_{x=0} \quad (5.67)$$

$$(2) \quad \left(\frac{dN_1}{dx} \right)_{x=R} = \left(\frac{dN_2}{dx} \right)_{x=R} \quad (5.68)$$

$$(3) \quad (N_1 = N_2)_{x=t_1} \quad (5.69)$$

$$(4) \quad D \left(\frac{dN_2}{dx} \right)_{x=t_1} = -(S \cdot N_2)_{x=t_1} \quad (5.70)$$

where x is the location of the activator center to the film surface, and S is the surface recombination velocity in cm/s. Solving the four boundary conditions yields the expressions for the constants, c_1 , c_2 , c_3 , and c_4 [see Appendix B].

Therefore, the intensity of the generated light (or brightness) can be obtained using the final solutions as:

(1) when $R > t_1$

$$(a) \quad 0 < x < t_1: \quad I_0(x) = \frac{E_e}{r} \cdot N_1(x) \quad (5.71)$$

(2) when $R < t_1$:

$$(a) \quad 0 < x < R: \quad I_0(x) = \frac{E_e}{r} \cdot N_1(x) \quad (5.72)$$

$$(b) \quad R < x < t_1: \quad I_0(x) = \frac{E_e}{r} \cdot N_2(x) \quad (5.73)$$

where E_e is the photon energy emitted in a TFP by an e-beam.

Predicted TFP Properties by Model

In order to apply the model to predict the CL properties of the TFPs, several prerequisite calculations are required in optical properties, e-beam-solid interactions, and resultant e-h pair concentrations. One example of the calculation procedures of the predictable

model built-up by Mathcad is shown in detail for a $Y_2O_3:Eu$ TFP on quartz substrate in Appendix C.

Optical Properties

Figure 5.10 shows that the propagating light with an angle θ is refracted by different optical media contacting with a film. The angles of r_1 , r_2 , and r_3 represent the refracted angles of θ in the air, substrate, and air on substrate side, respectively, and the refracted angles can be obtained using the equations below,

$$r_1(\theta) = \sin^{-1} \left(\frac{n_2}{n_1} \sin \theta \right) \quad (5.74)$$

$$r_2(\theta) = \sin^{-1} \left(\frac{n_2}{n_3} \sin \theta \right) \quad (5.75)$$

$$r_3(\theta) = \sin^{-1} \left(\frac{n_3}{n_1} \sin \theta \right) \quad (5.76)$$

where n_1 , n_2 , and n_3 are the refractive indices of air, film, and substrate, respectively.

Figure 5.11 shows that the schematic illustrations of different critical angles formed by $Y_2O_3:Eu$ TFP with quartz, sapphire, LAO, and silicon substrates. The angles of θ_{c1} , θ_{c2} , and θ_{c3} represent the critical angles from TFP to air (R-mode), TFP to substrate, and substrate to air (T-mode), respectively, and the critical angles can be obtained using the equations below,

$$\theta_{c1} = \sin^{-1}\left(\frac{n_1}{n_2}\right) \quad (5.77)$$

$$\theta_{c2} = \sin^{-1}\left(\frac{n_3}{n_2}\right) \quad (5.78)$$

$$\theta_{c3} = \sin^{-1}\left(\frac{n_1}{n_3}\right) . \quad (5.79)$$

Figure 5.12 shows that the calculated reflectivity of light having a wavelength of 611 nm with different incident angles at different interfaces formed among $Y_2O_3:Eu$ TFPs, air, and substrates such as quartz, sapphire, LAO, and silicon. Each ending point in each plot represents the critical angle formed by the two different optical media, and no ending point for YOE/Si and YOE/LAO indicates no existing critical angle between the two different optical media. One important thing in this figure is that all the propagating light with the incident angles greater than the critical angle has the reflectivity value of 1.0, which indicates total internal reflection inside the film. Therefore, the order of magnitude in total internal reflection inside the film is YOE/quartz > YOE/sapphire > YOE/silicon > YOE>LAO TFP systems. The reflectivity data can be obtained using the equations below,

$$R_1(\theta) = \frac{1}{2} \left(\frac{\sin(\theta - r_1(\theta))^2}{\sin(\theta + r_1(\theta))^2} + \frac{\tan(\theta - r_1(\theta))^2}{\tan(\theta + r_1(\theta))^2} \right) \quad (5.80)$$

$$R_2(\theta) = \frac{1}{2} \left(\frac{\sin(\theta - r_2(\theta))^2}{\sin(\theta + r_2(\theta))^2} + \frac{\tan(\theta - r_2(\theta))^2}{\tan(\theta + r_2(\theta))^2} \right) \quad (5.81)$$

$$R_3(\theta) = \frac{1}{2} \left(\frac{\sin(r_2(\theta) - r_3(\theta))^2}{\sin(r_2(\theta) + r_3(\theta))^2} + \frac{\tan(r_2(\theta) - r_3(\theta))^2}{\tan(r_2(\theta) + r_3(\theta))^2} \right) \quad (5.82)$$

where R_1 , R_2 , and R_3 are the reflectivities when light propagates from film to air, from film to substrate, and from substrate to air, respectively [Bil72].

Electron Beam-Solid Interactions

Figure 5.13 shows that the calculated R with $Y_2O_3:Eu$ phosphor based on the Equation 2.1. The R of ZnS solid is given for comparison. The expressions for calculating M , Z , and ρ are shown for $Y_2O_3:Eu$ as

$$M = \frac{3M_O + 2(0.97M_Y + 0.03M_{Eu})}{5} \quad (5.83)$$

$$Z = \frac{3Z_O + 2(0.97Z_Y + 0.03Z_{Eu})}{5} \quad (5.84)$$

$$\rho = \rho_{Y_2O_3} \left(\frac{M}{\frac{3M_O + 2M_Y}{5}} \right) \quad (5.85)$$

which result in, $M=45.921$ (g/mol), $Z=20.688$, and $\rho=5.115$ (g/cm³), and the R values of 53 nm at 2 kV and 246 nm at 5 kV.

Number of E-H Pairs in TFP

Figures 5.14 shows that the predicted concentrations of e-h pairs in $Y_2O_3:Eu$ TFP as a function of depth from the surface or film thickness. To calculate the concentrations, the values adopted in the proposed model are: $D=5.0 \text{ cm}^2/\text{s}$, $\tau=1e-9 \text{ sec}$, $\phi_0=100 \text{ nA}/\text{cm}^2$, $V_0=2 \text{ kV}$, and $\Delta E=3E_{g-Y2O3}$, depending on the S values. The graphs indicate that (1) the e-h pair concentration drastically decreases with increasing the penetration depth except for the very high S values; (2) higher S ($>1e5 \text{ cm/s}$) significantly reduces the number of e-h pairs which will participate the luminescent process; (3) smaller S ($<1e3 \text{ cm/s}$) negligibly affects the e-h pair concentrations.

Figure 5.15 shows another predicted e-h pair concentration profiles in the unit volume of $Y_2O_3:Eu$ TFP as a function of depth from film surface (or film thickness) with different accelerating voltages when $S=1e4 \text{ cm/s}$, $D=5.0 \text{ cm}^2/\text{s}$, $\tau=1e-9 \text{ sec}$, $\phi_0=100 \text{ nA}/\text{cm}^2$, and $\Delta E=3E_{g-Y2O3}$. This figure shows that the e-h pair concentration increases with increasing the applied voltage, and decreases with increasing the distance from the film surface. The total number of e-h pairs created in the $Y_2O_3:Eu$ TFP with the different voltages can be obtained using the sub-area of each plot by integrating from surface to the depth, as shown

in Figure 5.16. The graph clearly explains the linear increase of CL brightness with the accelerating voltage.

Shown in Figure 5.17 are the e-h pair profiles created in $Y_2O_3:Eu$ TFP as a function of film thickness with 2 and 5 kV when $S=1e4$ cm/s, $D=5.0$ cm²/s, and $\tau=1e-9$ sec, $i_0=100$ nA/cm², and $\Delta E=3E_{g-Y2O3}$. According to the model plot, the number of e-h pairs at 2 kV is greater than the number of e-h pairs at 5 kV when the film thickness is smaller than 100 nm. However, the rapid increase in the number of e-h pairs at 5 kV rapidly rises for the film thicknesses over 100 nm and then saturates at around 250 nm thickness which is the electron interaction range with $Y_2O_3:Eu$ phosphor.

Predicted CL Properties

Figure 5.18 predicts the total generated initial CL intensities (ΣI_0) inside $Y_2O_3:Eu$ TFP before propagation with three different diffusion coefficients of $D=1, 5$, and 10 cm²/sec as a function of film thickness when $\eta=0.3$, $S=1e4$ cm/s, $D=5.0$ cm²/s, $\tau=1e-9$ sec, $i_0=100$ nA/cm², $V_0=5$ kV, $t_i=500$ nm, and $\Delta E=3E_{g-Y2O3}$. This figure shows that the intensities increase very rapidly and then saturate at around 1 μ m film thickness for all the three cases. It also shows very small differences among the intensities before saturation and slightly higher intensities with increase of D value after 1

μm . Since the initial intensities are directly proportional to the number of charge carriers in a TFP, this calculation indicates that the charge carrier diffusion is an important part of CL generation process over the e-beam-solid interaction range. It also explains the reason why $\text{Y}_2\text{O}_3:\text{Eu}$ TFPs show rapid increase in CL brightness up to around $1 \mu\text{m}$ film thickness and then saturate after that, indicating that increasing film thickness greater than $1 \mu\text{m}$ is not very advantageous to get more CL brightness for the $\text{Y}_2\text{O}_3:\text{Eu}$ TFPs.

Figure 5.19 shows the predicted CL intensities of $\text{Y}_2\text{O}_3:\text{Eu}$ TFPs on quartz and sapphire substrates in both R- and T-modes as a function of RMS with $\eta=0.3$ and 0.5 when $S=1\text{e}4 \text{ cm/s}$, $D=5.0 \text{ cm}^2/\text{s}$, $\tau=1\text{e}-9 \text{ sec}$, $i_0=100 \text{ nA/cm}^2$, $V_0=2 \text{ kV}$, and $\Delta E=3E_{g-\text{Y}_2\text{O}_3}$. These predictions indicate that the quartz substrate gives higher CL intensities than the sapphire substrate does in both R- and T-modes, and even that quartz substrate with $\eta=0.3$ gives higher CL intensities than sapphire substrate with $\eta=0.5$.

Figure 5.20 shows separately the predicted diffuse and specular components of CL intensities of the $\text{Y}_2\text{O}_3:\text{Eu}$ TFPs on quartz, sapphire, LAO, and silicon substrates in R-mode as a function of RMS roughness when $S=1\text{e}4 \text{ cm/s}$, $D=5.0 \text{ cm}^2/\text{s}$, $\tau=1\text{e}-9 \text{ sec}$, $i_0=100 \text{ nA/cm}^2$, $V_0=2 \text{ kV}$, and $\Delta E=3E_{g-\text{Y}_2\text{O}_3}$. This figure

indicates that (1) for all the TFPs, specular component is almost independent of the roughness but diffuse component increases with the roughness increase; (2) the difference in specular component among the four different TFPs on various substrates is small; (3) specular component is the dominant contributor to the CL of $\text{Y}_2\text{O}_3\text{:Eu}$ TFPs on sapphire, LAO, and silicon substrates, but dominant only in the low roughness region for the $\text{Y}_2\text{O}_3\text{:Eu}$ TFPs on quartz substrates; (4) the contribution of diffuse component follows the order of total internal reflection in magnitude as shown previously in Figure 5.12, i.e., the diffuse part is greater with the roughness as the amount of total internal reflection is greater inside the film; (5) the diffuse component is the main factor to generate the difference in CL intensities for those TFP systems. Thus, quartz substrate is the most advantageous to get more diffuse contribution to CL for $\text{Y}_2\text{O}_3\text{:Eu}$ TFPs. Although the specular components in R-mode is approximately independent of the roughness and a small difference among the four TFP systems in Figure 5.20, a close investigation, as shown in Figure 5.21, shows very steady decrease in CL with the roughness and the order of $\text{YOE/silicon} > \text{YOE/quartz} > \text{YOE/LAO} > \text{YOE/sapphire}$ in CL.

Figure 5.22 is the combined CL intensities of the diffuse and specular components of the $\text{Y}_2\text{O}_3\text{:Eu}$ TFPs on quartz, sapphire, LAO, and silicon substrates, shown in

Figure 5.19. This figure indicates that the diffuse component of each TFP system determines the relative total CL intensity in R-mode among the four TFP systems except for the very small roughness region where the diffuse component is very small. Therefore, the predicted total CL intensities shows the order of magnitude as $\text{YOE/quartz} > \text{YOE/sapphire} > \text{YOE/silicon} > \text{YOE/LAO}$.

Figure 5.23 shows the combined CL intensities of the diffuse and specular components of the $\text{Y}_2\text{O}_3\text{:Eu}$ TFPs on quartz, sapphire, and LAO substrates in T-mode as a function of RMS roughness. Since the RMS roughness values at the interfaces 2 and 3 in the model were assumed to be negligible compared to the RMS roughness at the interface 1, the predicted CL intensities show almost independent of the roughness. The CL intensity also shows the same order as in R-mode. Silicon substrate gave no transmittance of light due to its high absorption of visible light. For comparison, the combined (diffuse + specular) CL intensities of the $\text{Y}_2\text{O}_3\text{:Eu}$ TFPs on quartz, sapphire, and LAO substrates in both R- and T-modes are shown in Figure 5.24. The plots predict higher CL intensities in R-mode than in T-mode for all the TFPs on the three different transparent substrates.

In summary, the smaller refractive index and low absorption coefficient characteristics of the quartz substrate resulted in higher theoretical CL intensities in

both R- and T-modes for the $Y_2O_3:Eu$ TFP systems. The smaller refractive index gives larger amount of internally reflected light in the film and this internally reflected light can get out of the film more easily as the film surface is rougher. The low absorption characteristic of visible light decreases absorption during multiple internal reflection and/or traveling through the substrate. These two combined effects result in better theoretical CL properties for the $Y_2O_3:Eu$ TFPs on quartz substrates.

Predicted and Experimental Results

In order to compare the predicted values with the experimental ones, all the required parameters discussed earlier in the modeling part in this chapter were input in the model. The model program automatically calculated the CL intensities step by step using the model equations in this chapter and gave the output data for the predicted CL intensities. The representative parameters input for the model calculation here were $S=4e3$ cm/s (1e3 cm/s for the TFPs on LAO due to small RMS values), $D=5.0$ cm²/s, $\tau=1e-9$ sec, $i_0=100$ nA/cm², $V_0=2$ kV and 5 kV, and $\Delta E=3E_{g-Y_2O_3}$. All of these input parameters can be changed in the model program depending on TFP systems [See the details in Appendix C].

Figures 5.25-5.28 show the predicted and experimental CL intensities of the $\text{Y}_2\text{O}_3\text{:Eu}$ TFPs deposited on quartz, sapphire, LAO, and silicon substrates in both R- and T-modes (no T-mode for the TFPs on silicon), respectively, as a function of RMS roughness or film thickness. In order to compare the trends of the both predicted and experimental CL intensities together at 2 and 5 kV voltages, the experimental CL intensities were normalized by the experimental CL value of the smallest roughness at 2 kV, and the predicted CL intensities were also normalized by the predicted CL value of the smallest roughness at 2 kV. According to Figures 5.25(a), 5.26(a), and 5.28 for the $\text{Y}_2\text{O}_3\text{:Eu}$ TFPs on quartz, sapphire, and silicon substrates, respectively, the experimental CL intensities in R-mode were observed lower than the predicted CL values as the RMS roughness increases. This is mainly attributed to the fixed surface recombination rate assumed to be $S=4\text{e}3$ cm/s for the figures, but actually the surface recombination rate increases as the roughness increases due to the increase of surface area. However, the $\text{Y}_2\text{O}_3\text{:Eu}$ TFPs on LAO substrates which showed very small difference in RMS roughness over the film thicknesses, showed close CL intensities between experimental and predicted ones in R-mode as shown in Figure 5.27(a). The figures indicate that the experimental values are closely distributed around the predicted ones.

Summary

A new model of CL from $\text{Y}_2\text{O}_3:\text{Eu}$ TFPs has been developed using the diffraction scattering theory which explains two different scattering components, specular and diffuse, of the reflected light when surface roughness is smaller or comparable to the wavelength of the incident light. Since CL is the resultant light emission by the e-beam-solid interaction, the number of photons emitted was assumed to be equal to the number of e-h pairs released by the incident electrons that recombine. The number of e-h pairs created and involved in the CL process was obtained using the diffusion equation under the steady state condition. The Kanaya-Okayama equation for the e-beam-solid interaction range was used to solve the generation rate and the diffusion equation. Two different regimes of CL generation ($0 < x \leq R$ and $R < x \leq t_1$) were considered in a TFP due to the charge carriers reaching the activator centers outside the e-beam-solid interaction range by diffusion process. Since the generated light from each activator in a TFP, experiences absorption, diffuse and specular reflections, and diffuse and specular transmittances at the various interfaces, the brightness was obtained integrating the total light intensity escaping out of film (R-mode) or substrate (T-mode) surfaces through the multiple scattering.

The model satisfactorily predicts the brightness of the TFPs well being in good agreement with the controlled experiments. The model explains CL generation due to the charge carrier diffusion process in addition to the e-beam-solid interaction range, rapid increase of CL brightness of the $\text{Y}_2\text{O}_3\text{:Eu}$ TFPs up to around 1 μm film thickness and saturation after that, higher CL intensities in R-mode than in T-mode in a TFP, higher CL intensities from the $\text{Y}_2\text{O}_3\text{:Eu}$ TFPs on quartz substrates than the TFPs on the other substrates.

The new model provides solid understandings on the CL properties of the TFPs with the effects of the various parameters, in terms of the role of surface roughness on reducing internal reflection, and the correlations of the surface roughness with other parameters such as substrate types, e-beam-solid interactions, surface recombination rates of carriers, carrier diffusion properties, optical scattering at the interfaces, and material's optical properties. Therefore, the model supplies a general solution to predict the luminance properties of the TFPs for the CL-based technologies like FEDs and CRTs.

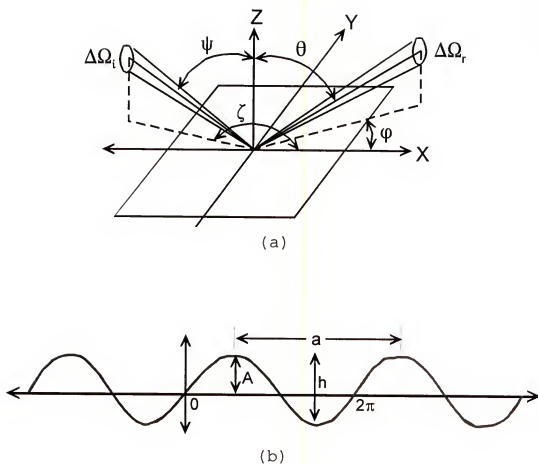


Figure 5.1. (a) Spatial distribution of the energy reflected from a rough surface with the coordinates and angle notations based on diffraction scattering theory [Top79]. (b) A sine waveform roughness where A is the amplitude of the waveform, a is the distance between the two peaks, and h is the roughness height.

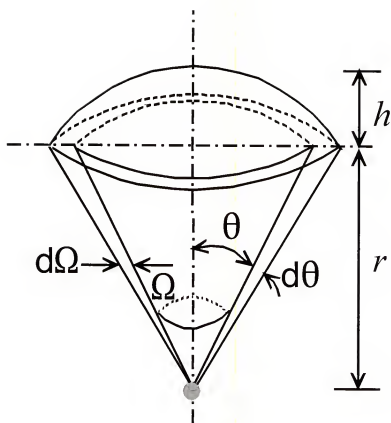


Figure 5.2. The solid angle (Ω) is defined as the ratio of surface area (s) to the square of a radius (r^2) of a cone.

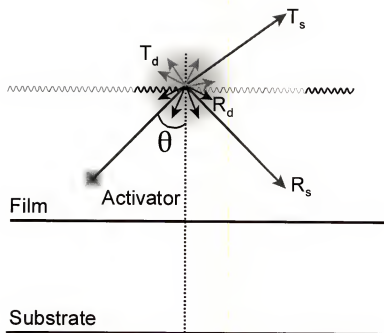


Figure 5.3. The light originated from an activator travels through the host matrix with an angle θ and scatters at the rough film surface. This scattered light is composed of specularly reflected (R_s), diffusely reflected (R_d), specularly transmitted (T_s), and diffusely transmitted (T_d) light.

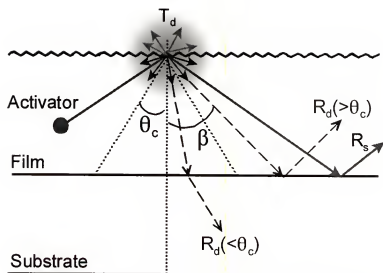
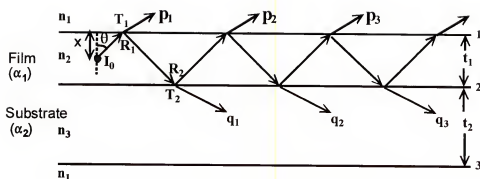
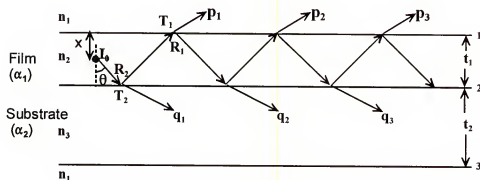


Figure 5.4. When the light generated from an activator diffusely transmits (T_d) and reflects (R_d) at the rough film surface, the light reflected back to film with an angle less than θ_c will transmit into substrate, and the light reflected back to film with an angle greater than θ_c will reflect internally with an angle β , in addition to specularly reflected light (R_s).

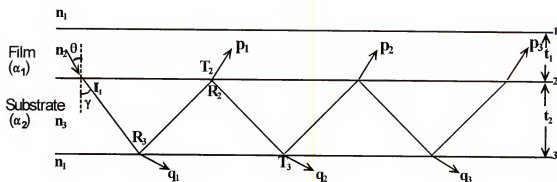


(a)

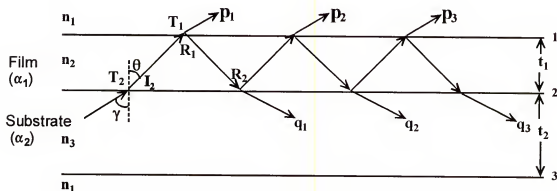


(b)

Figure 5.5. The generated light from an activator (I_0) which is located at a distance x from the film surface can be specularly transmitted from film into air ($p_{1,2,3}$) and substrate ($q_{1,2,3}$) during traveling (a) upward and (b) downward with an angle θ , depending on transmittance (T_1, T_2) and reflectivity (R_1, R_2) properties at the interfaces (1,2). α , n , and t represent absorption coefficient, refractive index, and thickness, respectively.



(a)



(b)

Figure 5.6. (a) The light transmitted from film into substrate (I_1) can be specularly transmitted from substrate into air ($q_{1,2,3}$) and also back-transmitted from substrate into film ($p_{1,2,3}$). (b) The light transmitted from substrate into film (I_2) can be specularly transmitted from film into air ($p_{1,2,3}$) and also back-transmitted from film into substrate ($q_{1,2,3}$). For both cases, light intensity depends on transmittance (T), reflectivity (R) at the interfaces (1,2,3), absorption coefficient ($\alpha_{1,2}$), thickness ($t_{1,2}$), and the angle θ .

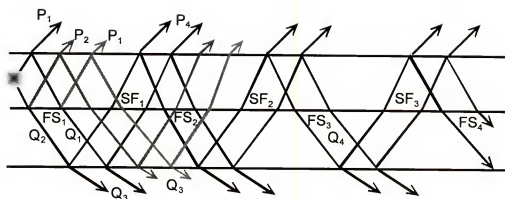
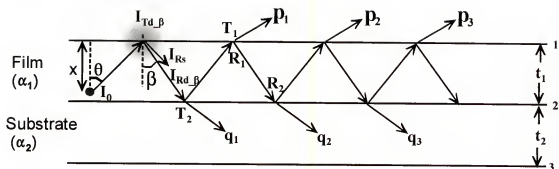
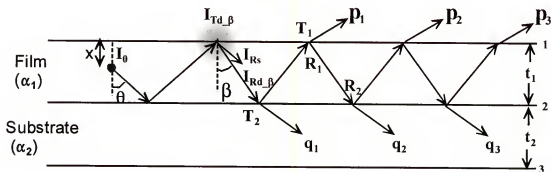


Figure 5.7. The sum of light specularly transmitted from film into substrate for the first time (FS_1), second time (FS_2), third time (FS_3), and so on, can be added together. The same applies for the sum of light specularly transmitted from substrate into air ($SF_{1,2,3,...}$). The sum of all $P_{1,2,4}$ is total specular light from film side, and the sum of all Q_3 is total specular light from substrate side. The sum of $Q_{1,2,4}$ equals to the sum of FS_i .



(a)



(b)

Figure 5.8. The diffusely reflected light with an angle β originally started with an angle θ , can also travel like specular component of the light and this light can also specularly transmit from film into air ($p_{1,2,3}$) and substrate ($q_{1,2,3}$) during traveling (a) upward and (b) downward, depending on transmittance (T_1, T_2) and reflectivity (R_1, R_2) properties at the interfaces (1,2).

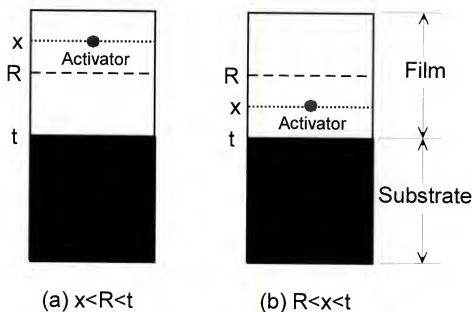


Figure 5.9. Light can be generated at the activator center located (a) inside the electron interaction range ($0 < x < R$), or (b) outside the electron interaction range ($R < x < t$) by charge carrier diffusion process in a thin film phosphor. R , x , and t represent electron interaction range, the location of activator center, and film thickness, respectively.

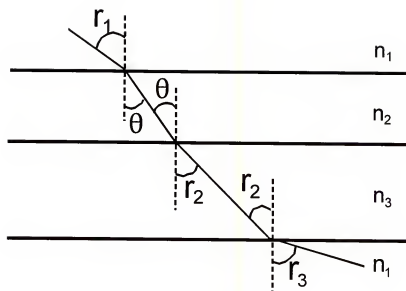


Figure 5.10. The light traveling with an angle θ is refracted by different optical media contacting with the film. Refracted angles r_1 , r_2 , and r_3 represent the corresponding angle of θ to the air (n_1), substrate (n_3), and air from substrate side (n_1), respectively.

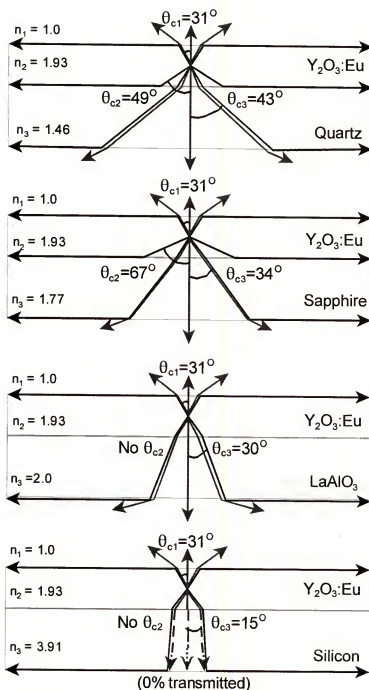


Figure 5.11. Schematic illustration of different critical angles formed by Y₂O₃:Eu TFPs with quartz, sapphire, LAO, and silicon substrates. The angles of θ_{c1} , θ_{c2} , and θ_{c3} represent the critical angles from TFP to air (R-mode), TFP to substrate, and substrate to air (T-mode), respectively.

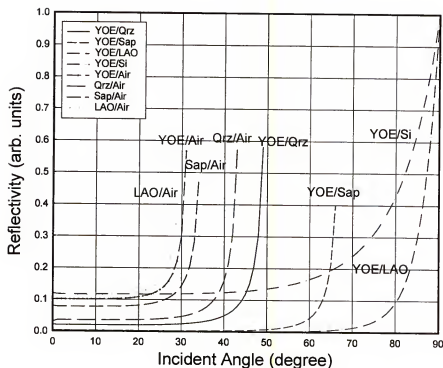


Figure 5.12. Calculated reflectivity of 611 nm wavelength with incident angles at different interfaces formed among $\text{Y}_2\text{O}_3\text{:Eu}$ TFPs, air, quartz, sapphire, LAO, and silicon substrates. Each ending point represents the critical angle formed by two different optical media, and no ending point with YOE/Si and YOE/LAO indicates no existing critical angle between the two media.

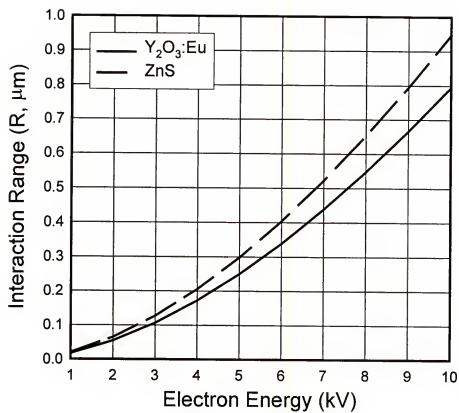


Figure 5.13. Calculated electron interaction ranges (R) with Y₂O₃:Eu and ZnS solids based on the Kanaya-Okayama equation.

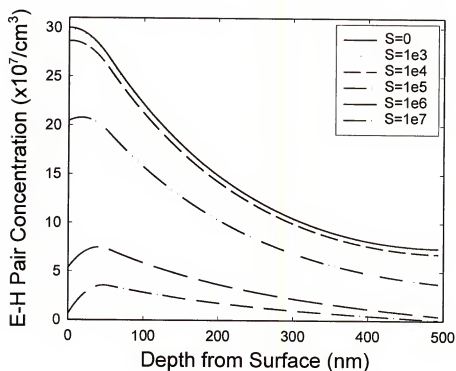


Figure 5.14. Predicted e-h pair concentrations created in $\text{Y}_2\text{O}_3:\text{Eu}$ TFPs with different distance from the surface (or film thickness) by the proposed model depending on the surface recombination rate (S) when $D=5.0 \text{ cm}^2/\text{s}$, $\tau=1e-9 \text{ sec}$, $I_0=100 \text{ nA}/\text{cm}^2$, $V_0=2 \text{ kV}$, and $\Delta E=3E_{g-\text{Y}_2\text{O}_3}$.

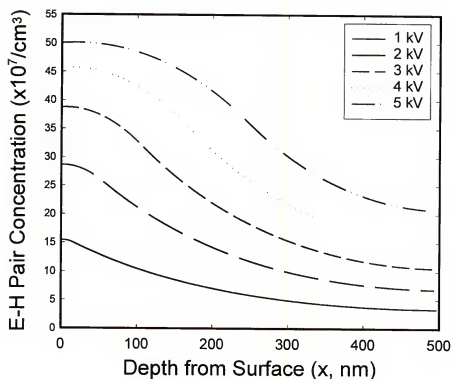


Figure 5.15. Predicted e-h pair concentration profile created in the unit volume of $\text{Y}_2\text{O}_3:\text{Eu}$ TFP as a function of distance from surface (or film thickness) with different accelerating voltages when $S=1\text{e}4 \text{ cm/s}$, $D=5.0 \text{ cm}^2/\text{s}$, $\tau=1\text{e}-9 \text{ sec}$, $i_0=100 \text{ nA/cm}^2$, and $\Delta E=3E_{g-\text{Y}_2\text{O}_3}$.

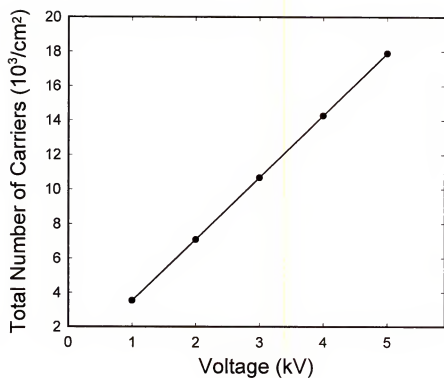


Figure 5.16. Predicted total number of e-h pairs created in the unit area of $\text{Y}_2\text{O}_3:\text{Eu}$ TFP with increasing the applied voltages when $R < t$, $S = 1 \times 10^4 \text{ cm/s}$, $D = 5.0 \text{ cm}^2/\text{s}$, and $\tau = 1 \times 10^{-9} \text{ sec}$.

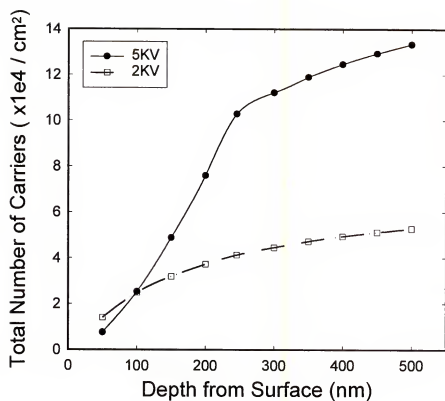


Figure 5.17. Predicted e-h pair profiles created in Y₂O₃:Eu TFP as a function of film thickness with 2 and 5 kV applied voltages when $S=1e4$ cm/s, $D=5.0$ cm²/s, and $\tau=1e-9$ sec.

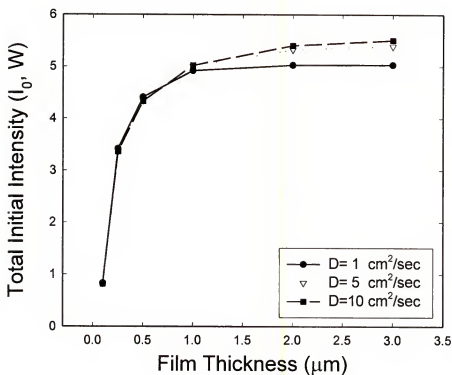


Figure 5.18. Predicted total initial CL intensities of $\text{Y}_2\text{O}_3:\text{Eu}$ TFP on quartz substrate with 3 different diffusion coefficients as a function of film thickness when $\eta=0.3$, $S=1\text{e}4 \text{ cm/s}$, $\tau=1\text{e}-9 \text{ sec}$, $i_0=100 \text{ nA/cm}^2$, $V_0=5 \text{ kV}$, and $\Delta E=3E_g$.

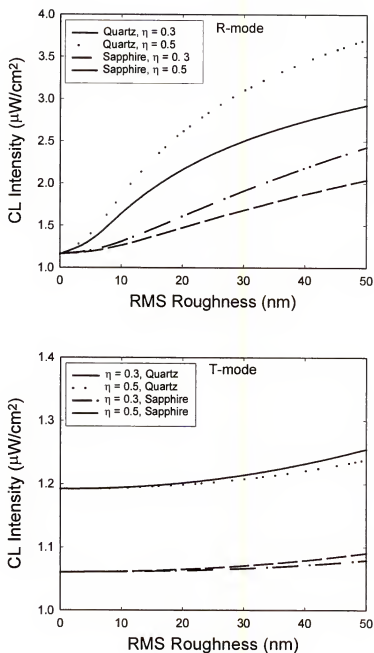


Figure 5.19. Predicted CL intensities of $\text{Y}_2\text{O}_3:\text{Eu}$ TFPs on quartz and sapphire substrates in both R- and T-modes as a function of RMS roughness with $\eta=0.3$ and 0.5 when $S=1\text{e}4$ cm/s , $D=5.0$ cm^2/s , $\tau=1\text{e}-9$ sec, $i_0=100$ nA/cm^2 , $V_0=2$ kV, and $\Delta E=3E_{g-\text{Y}_2\text{O}_3}$.

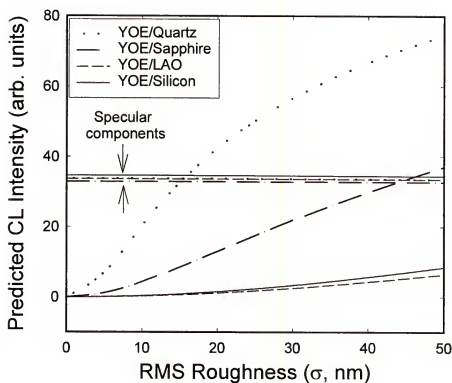


Figure 5.20. Predicted diffuse and specular (denoted) components of CL intensities of $\text{Y}_2\text{O}_3:\text{Eu}$ TFPs on quartz, sapphire, LAO, and silicon substrates in R-mode as a function of RMS when $\eta=0.3$, $S=1\text{e}4$ cm/s, $D=5.0$ cm^2/s , $\tau=1\text{e}-9$ sec, $i_0=100$ nA/cm^2 , $V_0=2$ kV, and $\Delta E=3E_{g-\text{Y}_2\text{O}_3}$.

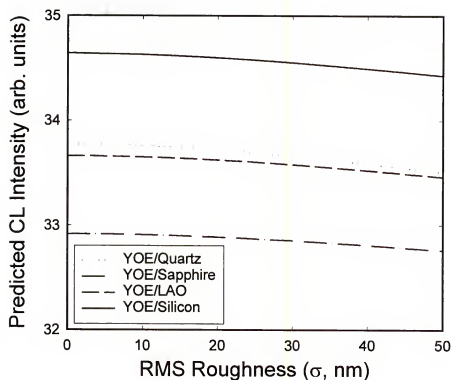


Figure 5.21 Predicted specular components of CL intensities of $\text{Y}_2\text{O}_3\text{:Eu}$ (YOE) TFPs on quartz, sapphire, LAO, and silicon substrates in R-mode as a function of RMS roughness when $\eta=0.3$, $S=1\text{e}4$ cm/s, $D=5.0\text{cm}^2/\text{s}$, $\tau=1\text{e}-9$ sec, $i_0=100$ nA/cm², $V_0=2$ kV, and $\Delta E=3E_{g-\text{Y}_2\text{O}_3}$.

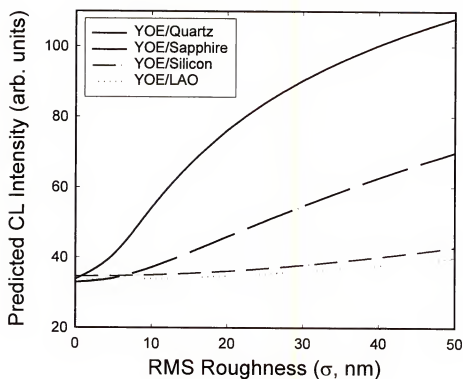


Figure 5.22. Predicted combined (diffuse + specular) CL intensities of $\text{Y}_2\text{O}_3\text{:Eu}$ TFPs on quartz, sapphire, LAO, and silicon substrates in R-mode as a function of RMS when $\eta=0.3$, $S=1\text{e}4$ cm/s, $D=5.0$ cm²/s, $\tau=1\text{e-}9$ sec, $i_0=100$ nA/cm², $V_0=2$ kV, and $\Delta E=3E_{g-\text{Y}_2\text{O}_3}$.

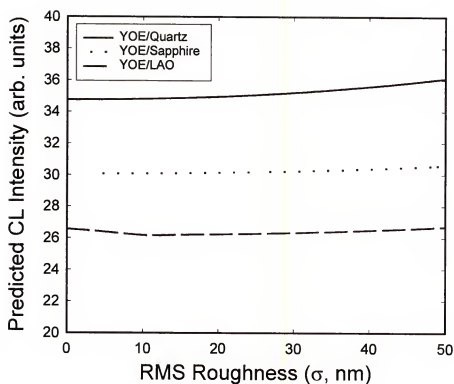


Figure 5.23. Predicted combined (diffuse + specular) CL intensities of $\text{Y}_2\text{O}_3:\text{Eu}$ TFPs on quartz, sapphire, and LAO substrates in T-mode as a function of RMS when $\eta=0.3$, $S=1\text{e}4$ cm/s , $D=5.0$ cm^2/s , $\tau=1\text{e}-9$ sec, $i_0=100$ nA/cm^2 , $V_0=2$ kV, and $\Delta E=3E_{g-\text{Y}_2\text{O}_3}$.

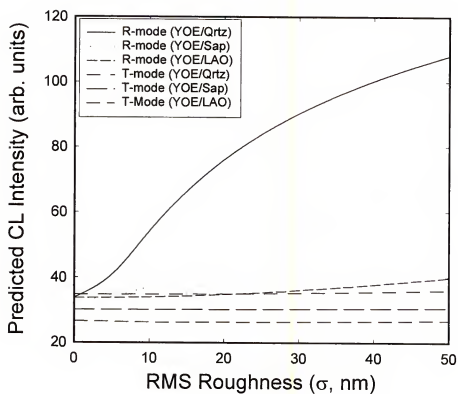


Figure 5.24. Comparison of the combined (diffuse + specular) CL intensities of $\text{Y}_2\text{O}_3\text{:Eu}$ TFPs on quartz, sapphire, and LAO substrates in both R-mode and T-mode as a function of RMS roughness when $\eta=0.3$, $S=1\text{e}4$ cm/s, $D=5.0$ cm²/s, $\tau=1\text{e}-9$ sec, $I_0=100$ nA/cm², $V_0=2$ kV, and $\Delta E=3E_{g-\text{Y}_2\text{O}_3}$.

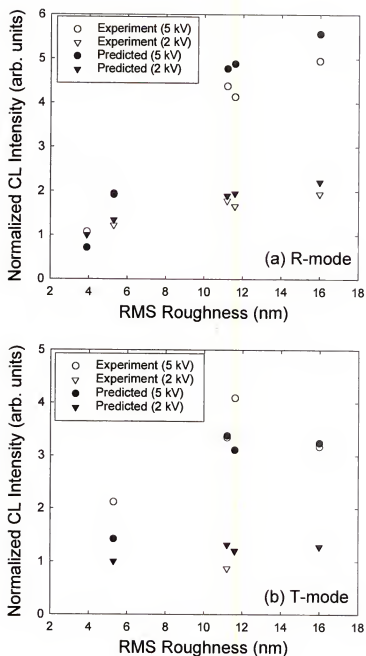


Figure 5.25. Predicted and experimental CL intensities of $\text{Y}_2\text{O}_3:\text{Eu}$ TFPs deposited on quartz substrates in (a) R-mode and (b) T-mode as a function of RMS when $\eta=0.3$, $S=4\text{e}3$ cm/s, $D=5.0$ cm^2/s , $\tau=1\text{e}-9$ sec, $i_0=100$ nA/ cm^2 , and $\Delta E=3E_{\text{g-Y}_2\text{O}_3}$.

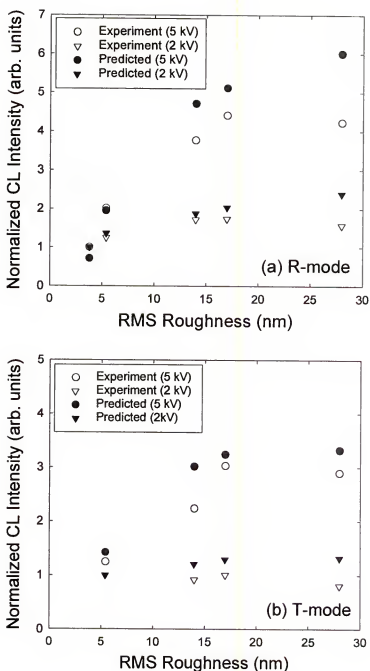


Figure 5.26. Predicted and experimental CL intensities of $\text{Y}_2\text{O}_3:\text{Eu}$ TFPs deposited on sapphire substrates in (a) R-mode and (b) T-mode as a function of RMS when $\eta=0.3$, $S=4\text{e}3$ cm/s, $D=5.0$ cm^2/s , $\tau=1\text{e}-9$ sec, $i_0=100$ nA/cm^2 , and $\Delta E=3E_{g-\text{Y}_2\text{O}_3}$.

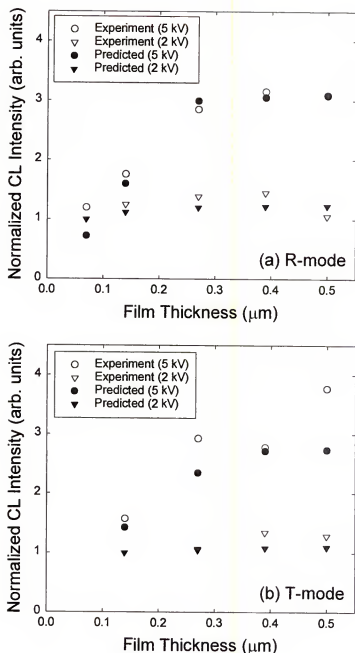


Figure 5.27. Predicted and experimental CL intensities of $\text{Y}_2\text{O}_3:\text{Eu}$ TFPs deposited on LaAlO_3 substrates in (a) R-mode and (b) T-mode with film thickness when $\eta=0.3$, $S=1\text{e}3$ cm/s, $D=5.0$ cm^2/s , $\tau=1\text{e}-9$ sec, $t_0=100$ nA/ cm^2 , and $\Delta E=3E_{g-\text{Y}_2\text{O}_3}$.

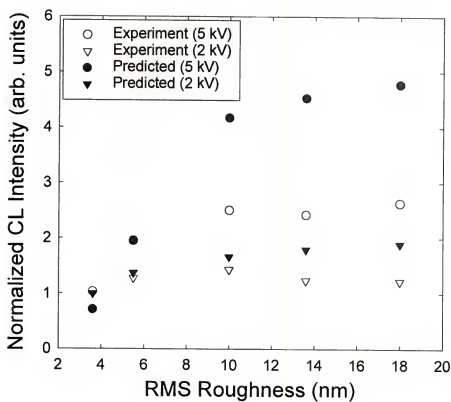


Figure 5.28. Predicted and experimental CL intensities of $\text{Y}_2\text{O}_3\text{:Eu}$ TFPs deposited on silicon substrates in R-mode only as a function of RMS when $\eta=0.3$, $S=4\text{e}3\text{ cm/s}$, $D=5.0\text{ cm}^2/\text{s}$, $\tau=1\text{e-}9\text{ sec}$, $i_0=100\text{ nA/cm}^2$, and $\Delta E=3E_{q-\text{Y}2\text{O}3}$.

CHAPTER 6 CONCLUSIONS

The effects of surface roughness on the luminance properties of TFPs have been investigated using PLD with $Y_2O_3:Eu$ TFPs grown on diamond-coated and bare silicon substrates. The $Y_2O_3:Eu$ TFPs on diamond-coated silicon substrates showed at least 2 times higher CL and PL brightness values than those on bare silicon substrates throughout the range of deposition temperatures from 200 to 700°C. The realization of the $Y_2O_3:Eu$ TFPs with higher CL and PL brightness values by means of an inherently rough diamond buffer layer, was mainly attributed to more outcoupling of light due to reduced internal reflection.

For more detailed studies on the effects of the TFP roughness with other fundamental parameters determining the luminance properties of the TFPs, the $Y_2O_3:Eu$ TFPs with different thicknesses and roughnesses were fabricated using PLD on the various substrate materials under a controlled experimental procedure. Microstructural and optical characterizations were conducted on those samples. Higher CL brightness of the $Y_2O_3:Eu$ TFPs deposited on LAO substrates in the smaller film thickness region, was mainly associated

with the capability of better epitaxial growth of the $Y_2O_3:Eu$ TFPs on the LAO substrates than the $Y_2O_3:Eu$ TFPs on quartz, sapphire, and silicon substrates. TEM and Z-contrast STEM studies strongly supported this explanation. The best CL brightness and efficiency was observed from the $Y_2O_3:Eu$ TFPs deposited for around 30 minutes of PLD (18000 laser pulses) in this study. The $Y_2O_3:Eu$ TFPs showed higher CL brightness and efficiency in R-mode than in T-mode, and the new theoretical model also explains this result.

The smaller refractive index and low absorption coefficient characteristics of the quartz substrates resulted in higher CL intensities in both theoretical and experimental results for the $Y_2O_3:Eu$ TFP systems. The smaller refractive index substrates produce larger amount of internally reflected light in the film and this internally reflected light escaped from the film more easily as the film surface is rougher. The low absorption of visible light by the quartz substrates also decreased light intensity losses during multiple internal reflections. These two combined effects resulted in better CL properties for the $Y_2O_3:Eu$ TFPs on quartz substrate.

A new predictable theoretical model of CL from the $Y_2O_3:Eu$ TFPs has been developed using the diffraction scattering theory which explains two different scattering components, specular and diffuse, of the reflected light

when the surface roughness is smaller or comparable to the wavelength of the incident light. Since CL is the resultant light emission by the interaction of e-beam with phosphor material, the number of photons emitted was assumed to be equal to the number of e-h pairs released by the incident electrons that recombine. The number of e-h pairs created and involved in the CL process was obtained using the diffusion equation under the steady state condition. The Kanaya-Okayama equation for the e-beam-solid interaction range was used to solve the generation rate and the diffusion of charge carriers. Two different regimes of CL generation ($0 < x \leq R$ and $R < x \leq t_1$) were considered in a TFP due to the charge carriers reaching the activator centers over the e-beam-solid interaction range by diffusion process. Since the generated light from each activator in a TFP, experiences absorption by TFP and substrate, diffuse and specular reflections, and diffuse and specular transmittances at the various interfaces (air/film, film/substrate, and substrate/air), the brightness was obtained integrating the total light intensity escaping out of film (R-mode) or substrate (T-mode) surfaces through the multiple scattering.

The model satisfactorily predicts the CL brightness of the TFPs well being in good agreement with the controlled experiments. The model explains CL generation due to the

charge carrier diffusion process in addition to the e-beam-solid interaction range, rapid increase of CL brightness of the $Y_2O_3:Eu$ TFPs up to around 1 μm film thickness and saturation after that, higher CL intensities in R-mode than in T-mode in a TFP, higher CL intensities from the $Y_2O_3:Eu$ TFPs on quartz substrates than the TFPs on the other substrates.

The model provides solid understandings on the CL properties of the TFPs with the effects of the various parameters, in terms of the role of surface roughness on reducing internal reflection, and the correlations of the surface roughness with other parameters such as substrate types, e-beam-solid interactions, surface recombination rates of carriers, carrier diffusion properties, optical scattering at the interfaces, and material's optical properties. Therefore, the new model supplies a general solution to predict the luminance properties of the TFPs for the CL-based technologies like FEDs and CRTs.

APPENDIX A DERIVATIONS FOR SPECULAR AND DIFFUSE PARTS

The mathematical derivations for the specular ($P_1 \sim P_4$, $Q_1 \sim Q_4$) and diffuse ($P_5 \sim P_6$, $Q_5 \sim Q_6$, I_{Td_up} , I_{Td_down}) components of the propagating light are introduced in detail for understandings.

1. Derivation for Specular Component of Light

(1) Light Propagating in Upward Direction

In Figure 5.5(a); using Equations (5.2), (5.5), and (5.8), the intensity of each specular component of light transmitted from film into air through the interface 1 (p_1, p_2 , and p_3) are:

$$p_1 = \frac{I_0}{2} \sin \theta d T_1(\theta) \exp\left(\frac{-\alpha_1 x}{\cos \theta}\right) \quad (A.1)$$

$$p_2 = p_1 R_1(\theta) R_2(\theta) \exp\left(\frac{-2\alpha_1 t_1}{\cos \theta}\right) \exp\left[-\left(\frac{2\sqrt{2}\pi\sigma \cos \theta}{\lambda}\right)^2\right] \quad (A.2)$$

$$p_3 = p_1 \left[R_1(\theta) R_2(\theta) \exp\left(\frac{-2\alpha_1 t_1}{\cos \theta}\right) \exp\left[-\left(\frac{2\sqrt{2}\pi\sigma \cos \theta}{\lambda}\right)^2\right] \right]^2. \quad (A.3)$$

The equations (A.1)-(A.3) and further expressions for p_4 , p_5, \dots, p_∞ show the relationship of the geometric series,

$$a + ar + ar^2 + \dots = \sum_{n=0}^{\infty} ar^n = \frac{a}{1-r}. \quad (A.4)$$

Therefore, the sum intensity of the specular components transmitted from film into air through the interface 1 ($P_1 = p_1 + p_2 + p_3 + \dots + p_\infty$) can be derived as in Equation (5.18).

The same approach can be applied for the intensity of each specular component of light transmitted from film into substrate through the interface 2 (q_1, q_2 , and q_3):

$$q_1 = \frac{I_0}{2} \sin \theta d \theta R_1(\theta) T_2(\theta) \exp\left(\frac{-a_1(t_1 + x)}{\cos \theta}\right) \exp\left[-\left(\frac{2\sqrt{2}\pi\sigma \cos \theta}{\lambda}\right)^2\right] \quad (\text{A.5})$$

$$q_2 = q_1 R_1(\theta) R_2(\theta) \exp\left(\frac{-2a_1 t_1}{\cos \theta}\right) \exp\left[-\left(\frac{2\sqrt{2}\pi\sigma \cos \theta}{\lambda}\right)^2\right] \quad (\text{A.6})$$

$$q_3 = q_1 \left[R_1(\theta) R_2(\theta) \exp\left(\frac{-2a_1 t_1}{\cos \theta}\right) \exp\left[-\left(\frac{2\sqrt{2}\pi\sigma \cos \theta}{\lambda}\right)^2\right] \right]^2 \quad (\text{A.7})$$

Therefore, the sum intensity of the specular components transmitted from film into substrate through the interface 2 ($Q_1 = q_1 + q_2 + q_3 + \dots + q_\infty$) can also be derived as in Equation (5.19).

(2) Light Propagating in Downward Direction

In Figure 5.5(b), the intensity of each specular component of light transmitted from film into air through interface 1 (p_1, p_2 , and p_3) can be expressed using Equations (5.2), (5.5), and (5.8) as

$$p_1 = \frac{I_0}{2} \sin \theta d \theta R_2(\theta) T_1(\theta) \exp\left[\frac{-a_1(2t_1 - x)}{\cos \theta}\right] \quad (\text{A.8})$$

$$p_2 = p_1 R_1(\theta) R_2(\theta) \exp\left(\frac{-2a_1 t_1}{\cos \theta}\right) \exp\left[-\left(\frac{2\sqrt{2}\pi\sigma \cos \theta}{\lambda}\right)^2\right] \quad (\text{A.9})$$

$$p_3 = p_1 \left[R_1(\theta) R_2(\theta) \exp\left(\frac{-2a_1 t_1}{\cos \theta}\right) \exp\left[-\left(\frac{2\sqrt{2}\pi\sigma \cos \theta}{\lambda}\right)^2\right] \right]^2 \quad (\text{A.10})$$

Using Equation (A.4), the sum intensity of all the specular components transmitted from film into air through the interface 1 ($P_2 = p_1 + p_2 + p_3 + \dots + p_\infty$) can be derived as in Equation (5.20).

The intensity of each specular component of light transmitted from film into substrate through the interface 2 (q_1, q_2 , and q_3) is:

$$q_1 = \frac{I_0}{2} \sin \theta d \theta T_2(\theta) \exp\left(\frac{-a_1(t_1 - x)}{\cos \theta}\right) \quad (\text{A.11})$$

$$q_2 = q_1 R_1(\theta) R_2(\theta) \exp\left(\frac{-2a_1 t_1}{\cos \theta}\right) \exp\left[-\left(\frac{2\sqrt{2}\pi\sigma \cos \theta}{\lambda}\right)^2\right] \quad (\text{A.12})$$

$$q_3 = q_1 \left[R_1(\theta) R_2(\theta) \exp\left(\frac{-2\alpha_1 t_1}{\cos\theta}\right) \exp\left[-\left(\frac{2\sqrt{2}\pi\sigma \cos\theta}{\lambda}\right)^2\right] \right]^2. \quad (\text{A.13})$$

Therefore, the sum intensity of all the specular components transmitted from film into substrate through the interface 2 ($Q_2 = q_1 + q_2 + q_3 + \dots + q_\infty$) can also be derived using Equation (A.4) as in Equation (5.21).

(3) Light (I_1) Transmitted from Film into Substrate

In Figure 5.6(a), the intensity of each specular component of light transmitted back from substrate into film through the interface 2 (p_1, p_2 , and p_3) can be expressed as

$$p_1 = I_1 R_3(\theta) T_2(\theta) \exp\left(\frac{-2\alpha_2 t_2}{\cos\gamma}\right) \quad (\text{A.14})$$

$$p_2 = p_1 R_2(\theta) R_3(\theta) \exp\left(\frac{-2\alpha_2 t_2}{\cos\gamma}\right) \quad (\text{A.15})$$

$$p_3 = p_1 \left[R_2(\theta) R_3(\theta) \exp\left(\frac{-2\alpha_2 t_2}{\cos\gamma}\right) \right]^2. \quad (\text{A.16})$$

Using Equation (A.4), the sum intensity of all the specular components transmitted back from substrate into film through the interface 2 ($P_3 = p_1 + p_2 + p_3 + \dots + p_\infty$) can be derived as in Equation (5.22).

The intensity of each specular component of light transmitted from substrate into air through the interface 3 (q_1, q_2 , and q_3) is:

$$q_1 = I_1 T_3(\theta) \exp\left(\frac{-\alpha_2 t_2}{\cos\gamma}\right) \quad (\text{A.17})$$

$$q_2 = q_1 R_2(\theta) R_3(\theta) \exp\left(\frac{-2\alpha_2 t_2}{\cos\gamma}\right) \quad (\text{A.18})$$

$$q_3 = q_1 \left[R_2(\theta) R_3(\theta) \exp\left(\frac{-2\alpha_2 t_2}{\cos\gamma}\right) \right]^2. \quad (\text{A.19})$$

Therefore, the sum intensity of all the specular components transmitted from substrate into air through the interface 3 ($Q_3 = q_1 + q_2 + q_3 + \dots + q_\infty$) can also be derived as in Equation (5.23).

(4) Light (I_2) Transmitted Back from Substrate into Film

In Figure 5.6(b), the light with an intensity of I_2 will also experience multiple scattering in the film. Then, the intensity of each specular component of light transmitted from film into air through the interface 1 (p_1, p_2 , and p_3) can be expressed using Equation (5.6) as

$$p_1 = I_2 T_1(\theta) \exp\left(\frac{-\alpha_1 t_1}{\cos\theta}\right) \quad (\text{A.20})$$

$$p_2 = p_1 R_1(\theta) R_2(\theta) \exp\left(\frac{-2\alpha_1 t_1}{\cos\theta}\right) \exp\left[-\left(\frac{2\sqrt{2}\pi\sigma \cos\theta}{\lambda}\right)^2\right] \quad (\text{A.21})$$

$$p_3 = p_1 \left[R_1(\theta) R_2(\theta) \exp\left(\frac{-2\alpha_1 t_1}{\cos\theta}\right) \exp\left[-\left(\frac{2\sqrt{2}\pi\sigma \cos\theta}{\lambda}\right)^2\right] \right]^2 \quad (\text{A.22})$$

Using the geometric series, the sum intensity of all the specular components transmitted from film into air through the interface 1 ($P_4 = p_1 + p_2 + p_3 + \dots + p_\infty$) can be derived as in Equation (5.24).

The same can be applied for the intensity of each specular component of light transmitted from film into substrate through the interface 2 (q_1, q_2 , and q_3):

$$q_1 = I_2 R_1(\theta) T_2(\theta) \exp\left(\frac{-2\alpha_1 t_1}{\cos\theta}\right) \exp\left[-\left(\frac{2\sqrt{2}\pi\sigma \cos\theta}{\lambda}\right)^2\right] \quad (\text{A.23})$$

$$q_2 = q_1 R_1(\theta) R_2(\theta) \exp\left(\frac{-2\alpha_1 t_1}{\cos\theta}\right) \exp\left[-\left(\frac{2\sqrt{2}\pi\sigma \cos\theta}{\lambda}\right)^2\right] \quad (\text{A.24})$$

$$q_3 = q_1 \left[R_1(\theta) R_2(\theta) \exp\left(\frac{-2\alpha_1 t_1}{\cos\theta}\right) \exp\left[-\left(\frac{2\sqrt{2}\pi\sigma \cos\theta}{\lambda}\right)^2\right] \right]^2 \quad (\text{A.25})$$

These equations yield the expression for the sum intensity of all the specular components transmitted into substrate

($Q_d = q_1 + q_2 + q_3 + \dots + q_\infty$) as in Equation (5.25).

2. Derivation for Diffuse Component of Light

(1) Light Propagating in Upward Direction (Diffuse)

In Figure 5.8(a), the p_1, p_2 , and p_3 are the intensities of the light propagating like a specular component after the 1st scattering at interface 1. For this case, the intensities of p_1, p_2 , and p_3 can be expressed using Equations (A.1), (A.5), and (5.16) as

$$p_1 = \frac{I_0}{2} \sin \theta d \theta \exp\left(\frac{-\alpha_1 x}{\cos \theta}\right) R_1(\theta) \left(\frac{1}{1+\eta}\right) \left[1 - \exp\left[-\left(\frac{2\sqrt{2}\pi\sigma}{\lambda} \cos \theta\right)^2\right]\right] \sin \beta d \beta R_2(\beta) T_1(\beta) \exp\left(\frac{-2\alpha_1 t_1}{\cos \beta}\right) \quad (\text{A.26})$$

$$p_2 = p_1 R_1(\beta) R_2(\beta) \exp\left(\frac{-2\alpha_1 t_1}{\cos \beta}\right) \quad (\text{A.27})$$

$$p_3 = p_1 \left[R_1(\beta) R_2(\beta) \exp\left(\frac{-2\alpha_1 t_1}{\cos \beta}\right) \right]^2 \quad (\text{A.28})$$

Thus, the sum intensity of all the light transmitted from film into air initiated by the 1st diffuse reflection ($P_5 = p_1 + p_2 + p_3 + \dots + p_\infty$) is as in Equation (5.37).

The same approach can be applied for the intensities of the light transmitted from film into substrate through the interface 2 (q_1, q_2 , and q_3) propagating like a specular component after the 1st scattering at interface 1:

$$q_1 = \frac{I_0}{2} \sin \theta d \theta \exp\left(\frac{-\alpha_1 x}{\cos \theta}\right) R_1(\theta) \left(\frac{1}{1+\eta}\right) \left[1 - \exp\left[-\left(\frac{2\sqrt{2}\pi\sigma}{\lambda} \cos \theta\right)^2\right]\right] \sin \beta d \beta T_2(\beta) \exp\left(\frac{-\alpha_1 t_1}{\cos \beta}\right) \quad (\text{A.29})$$

$$q_2 = q_1 R_1(\beta) R_2(\beta) \exp\left(\frac{-2\alpha_1 t_1}{\cos \beta}\right) \quad (\text{A.30})$$

$$q_3 = q_1 \left[R_1(\beta) R_2(\beta) \exp\left(\frac{-2\alpha_1 t_1}{\cos \beta}\right) \right]^2 \quad (\text{A.31})$$

Thus, the sum intensity of all the light transmitted from film into substrate ($Q_s = q_1 + q_2 + q_3 + \dots + q_\infty$) initiated by the 1st diffuse reflection at interface 1 is as in Equation (5.38).

Therefore, Equation (5.39), the diffuse transmittance from film into air by upward propagation ($I_{T_d, up}$), can be derived using the below equations which shows the relationship of Equation (A.4),

$$\text{1st diffuse: } I_{T_d, up}^1 = \frac{I_0}{2} \sin \theta d \theta \exp\left(\frac{-\alpha_1 x}{\cos \theta}\right) R_1(\theta) \left(\frac{\eta}{1+\eta}\right) \left[1 - \exp\left[-\left(\frac{2\sqrt{2}\pi\sigma}{\lambda} \cos \theta\right)^2\right]\right] \quad (\text{A.32})$$

$$2nd \text{ diffuse: } I_{t_{2,sp}}^2 = I_{t_{2,sp}}^1 \cdot R_1(\theta) \exp \left[- \left(\frac{2\sqrt{2}\pi\sigma}{\lambda} \cos\theta \right)^2 \right] R_2(\theta) \exp \left(\frac{-2\alpha_1 t_1}{\cos\theta} \right) \quad (\text{A.33})$$

$$3rd \text{ diffuse: } I_{t_{2,sp}}^3 = I_{t_{2,sp}}^1 \cdot \left[R_1(\theta) \exp \left[- \left(\frac{2\sqrt{2}\pi\sigma}{\lambda} \cos\theta \right)^2 \right] R_2(\theta) \exp \left(\frac{-2\alpha_1 t_1}{\cos\theta} \right) \right]^2. \quad (\text{A.34})$$

(2) Light Propagating in Downward Direction (Diffuse)

In Figure 5.8(b), the p_1, p_2 , and p_3 are the intensities of the light propagating like a specular component after reflected at interface 2 and then the 1st scattering at interface 1, which can be expressed using Equations (A.1), (A.5), and (5.16) as

$$p_1 = \frac{I_0}{2} \sin\theta d\theta \exp \left(\frac{-\alpha_1(t_1 - x)}{\cos\theta} \right) R_2(\theta) \exp \left(\frac{-\alpha_1 t_1}{\cos\theta} \right) R_1(\theta) \left(\frac{1}{1+\eta} \right) \left[1 - \exp \left[- \left(\frac{2\sqrt{2}\pi\sigma}{\lambda} \cos\theta \right)^2 \right] \right] \sin\beta d\beta R_2(\beta) T_1(\beta) \exp \left(\frac{-2\alpha_1 t_1}{\cos\beta} \right) \quad (\text{A.35})$$

$$p_2 = p_1 R_1(\beta) R_2(\beta) \exp \left(\frac{-2\alpha_1 t_1}{\cos\beta} \right) \quad (\text{A.36})$$

$$p_3 = p_1 \left[R_1(\beta) R_2(\beta) \exp \left(\frac{-2\alpha_1 t_1}{\cos\beta} \right) \right]^2. \quad (\text{A.37})$$

Thus, the sum intensity of all the light transmitted from film into air initiated by the 1st diffuse reflection ($p_6 = p_1 + p_2 + p_3 + \dots + p_\infty$) is as in Equation (5.40).

The same approach can be applied for the intensities of the light transmitted from film into substrate through the interface 2 (q_1, q_2 , and q_3) propagating like a specular component after the 1st scattering at interface 1:

$$q_1 = \frac{I_0}{2} \sin\theta d\theta \exp \left(\frac{-\alpha_1(2t_1 - x)}{\cos\theta} \right) R_2(\beta) R_1(\theta) \left(\frac{1}{1+\eta} \right) \left[1 - \exp \left[- \left(\frac{2\sqrt{2}\pi\sigma}{\lambda} \cos\theta \right)^2 \right] \right] \sin\beta d\beta T_2(\beta) \exp \left(\frac{-\alpha_1 t_1}{\cos\beta} \right) \quad (\text{A.38})$$

$$q_2 = q_1 R_1(\beta) R_2(\beta) \exp \left(\frac{-2\alpha_1 t_1}{\cos\beta} \right) \quad (\text{A.39})$$

$$q_3 = q_1 \left[R_1(\beta) R_2(\beta) \exp \left(\frac{-2\alpha_1 t_1}{\cos\beta} \right) \right]^2. \quad (\text{A.40})$$

Thus, the sum intensity of all the light transmitted from film into substrate ($Q_6 = q_1 + q_2 + q_3 + \dots + q_\infty$) initiated by the 1st diffuse reflection at interface 1 is as in Equation 5.41.

Therefore, Equation (5.42), the diffuse transmittance from film into air by downward propagation ($I_{Td,down}$), can be derived using below equations showing the relationship of Equation (A.4),

$$1st \text{ diffuse: } I_{T_{d,down}}^1 = \frac{I_0}{2} \sin \theta d\theta \exp\left(\frac{-a_1(2t_1 - x)}{\cos \theta}\right) R_2(\theta) R_1(\theta) \left(\frac{\eta}{1+\eta}\right) \left[1 - \exp\left[-\left(\frac{2\sqrt{2}\pi\sigma}{\lambda} \cos \theta\right)^2\right]\right] \quad (A.41)$$

$$2nd \text{ diffuse: } I_{T_{d,down}}^2 = I_{T_{d,down}}^1 \cdot R_1(\theta) \exp\left[-\left(\frac{2\sqrt{2}\pi\sigma}{\lambda} \cos \theta\right)^2\right] R_2(\theta) \exp\left(\frac{-2a_1 t_1}{\cos \theta}\right) \quad (A.42)$$

$$3rd \text{ diffuse: } I_{T_{d,down}}^3 = I_{T_{d,down}}^1 \cdot \left[R_1(\theta) \exp\left[-\left(\frac{2\sqrt{2}\pi\sigma}{\lambda} \cos \theta\right)^2\right] R_2(\theta) \exp\left(\frac{-2a_1 t_1}{\cos \theta}\right) \right]^2. \quad (A.43)$$

APPENDIX B
SOLUTIONS FOR CONSTANTS C_1 , C_2 , C_3 , and C_4

The expressions of the four constants (c_1 , c_2 , c_3 , and c_4) required for calculating the number of charge carriers, N_1 and N_2 in Equations 5.64-65, are given by solving the four boundary conditions in Equations 5.66-69 using Mathcad:

$$c_1 = \frac{1}{2} C \frac{D^2 m^2 \exp(2mR - 2mt_1) - S^2 \exp(2mR - 2mt_1) - 2DmS \exp(mR - 2mt_1) + 2S^2 \exp(mR - 2mt_1) - D^2 m^2 - 2DmS - S^2}{\exp(mR)m^2 [-D^2 m^2 - 2DmS - S^2 + D^2 m^2 \exp(-mt_1)^2 - 2DmS \exp(-mt_1)^2 + S^2 \exp(-mt_1)^2]} \quad (\text{B.1})$$

$$c_2 = \frac{1}{2} C \frac{D^2 m^2 \exp(2mR - 2mt_1) - 2DmS \exp(2mR - 2mt_1) + S^2 \exp(2mR - 2mt_1) - D^2 m^2 + S^2 - 2S \exp(mR) Dm - 2S^2 \exp(mR)}{\exp(mR)m^2 [-D^2 m^2 - 2DmS - S^2 + D^2 m^2 \exp(-mt_1)^2 - 2DmS \exp(-mt_1)^2 + S^2 \exp(-mt_1)^2]} \quad (\text{B.2})$$

$$c_3 = \frac{1}{2} C \frac{[-D^2 m^2 + 2DmS + D^2 m^2 \exp(mR)^2 - S^2 - S^2 \exp(mR)^2 - 2DmS \exp(mR) + 2S^2 \exp(mR)] \exp(-2mt_1 - mR)}{m^2 [-D^2 m^2 - 2DmS - S^2 + D^2 m^2 \exp(-mt_1)^2 - 2DmS \exp(-mt_1)^2 + S^2 \exp(-mt_1)^2]} \quad (\text{B.3})$$

$$c_4 = \frac{1}{2} C \frac{(Dm + S)[-Dm + Dm \exp(mR)^2 + S - 2S \exp(mR) + S \exp(mR)^2]}{\exp(mR)m^2 [-D^2 m^2 - 2DmS - S^2 + D^2 m^2 \exp(-mt_1)^2 - 2DmS \exp(-mt_1)^2 + S^2 \exp(-mt_1)^2]} \quad (\text{B.4})$$

APPENDIX C MODEL CALCULATION FOR A $Y_2O_3:Eu$ TFP ON QUARTZ

An example of calculation using the theoretical model built-up by Mathcad is shown for a $Y_2O_3:Eu$ TFP on quartz substrate. Most of the complicated equations in chapter 5 are omitted or abbreviated here.

$Y_2O_3:Eu$ on Quartz Substrate When $R < 1$

Input Data

Initial current density:	$I_0 := 100 \cdot 10^{-9}$	(A/cm ²)
Accelerating voltage:	$V_0 := 5000$	(V)
Thickness:	film:	$t_1 := 500 \cdot 10^{-7}$ (cm)
	substrate:	$t_2 := 0.1$ (cm)
Refractive index:	air:	$n_1 := 1.93$ (at 611 nm)
	film:	$n_2 := 1.46$ (at 611 nm)
	substrate:	$n_3 := 1.00$ (at 611 nm)
Absorption coefficient:	film:	$\alpha_1 := 50$ (cm ⁻¹)
	substrate:	$\alpha_2 := 0.7$ (cm ⁻¹)
Film roughness:	$\sigma := 11.2 \cdot 10^{-7}$	(cm)
Carrier lifetime:	$\tau := 1 \cdot 10^{-9}$	(sec)
Carrier mobility:	$\mu_e := 192$	(cm ² /V-s)
Surface recombination rate:	$S := 1 \cdot 10^4$	(cm/sec)
Ratio (T/R):	$\eta := 0.3$	
Wavelength of generated light:	$\lambda := 611 \cdot 10^{-7}$	(cm)
Band gap of $Y_2O_3:Eu$:	$E_g := 5.60 \cdot 1.6 \cdot 10^{-19}$	(J)
Photon energy at 611 nm:	$E_e := 2.03 \cdot 1.6 \cdot 10^{-19}$	(J)
Boltzmann factor at room temp:	$kT := 0.026 \cdot 1.6 \cdot 10^{-19}$	(J)
Density of Y_2O_3 :	$r_{Y_2O_3} := 5.03$	(g/cm ³)
Atomic number:	$Z_O := 8,$ $Z_Y := 39,$ $Z_{Eu} := 63,$	
Atomic weight:	$M_O := 16,$ $M_Y := 88.91,$ $M_{Eu} := 151.96$	

Interaction Range and Optical Properties

$$M_{_Y2O3:Eu} := \frac{2(0.97 \cdot M_{_Y} + 0.03 \cdot M_{_Eu}) + 3 \cdot M_{_O}}{5}, \quad M_{_Y2O3:Eu} = 45.921 \quad (\text{g/mol})$$

$$Z_{_Y2O3:Eu} := \frac{2(0.97 \cdot Z_{_Y} + 0.03 \cdot Z_{_Eu}) + 3 \cdot Z_{_O}}{5}, \quad Z_{_Y2O3:Eu} = 45.921$$

$$\rho_{_Y2O3:Eu} := 5.03 \cdot \frac{M_{_Y2O3:Eu}}{3 \cdot M_{_O} + 2 \cdot M_{_Y}}, \quad \rho_{_Y2O3:Eu} = 5.114 \quad (\text{g/cm}^3)$$

$$E_0 := \frac{V_0}{1000}, \quad E_0 = 5 \quad (\text{keV})$$

$$R := \frac{276 \cdot 10^{-8} \cdot M_{_Y2O3:Eu} \cdot E_0^{1.67}}{Z_{_Y2O3:Eu}^{0.89} \cdot \rho_{_Y2O3:Eu}}, \quad R = 2.457 \cdot 10^{-5} \quad (\text{cm})$$

$$D := 0.026 \cdot \mu_e, \quad D = 4.992 \quad (\text{cm}^2/\text{s})$$

$$m := \sqrt{\frac{1}{D \cdot r}}, \quad m = 1.415 \cdot 10^4 \quad (\text{cm}^{-1})$$

$$\Delta E := 3E_{g_Y2O3:Eu}, \quad \Delta E_{g_Y2O3} = 16.8 \cdot 1.6 \cdot 10^{-19} \quad (\text{J})$$

$$G := \frac{I_0 \cdot V_0}{\Delta E \cdot R}, \quad G = 7.57 \cdot 10^{18} \quad (\text{cm}^{-3} \cdot \text{s}^{-1})$$

$$C := -\frac{G}{D}, \quad C = -1.516 \cdot 10^{18} \quad (\text{cm}^{-5})$$

$$\frac{R}{t_1} = 0.491$$

$$r_1(\theta) := \sin^{-1} \left(\frac{n_2}{n_1} \cdot \sin(\theta) \right), \quad R_1(\theta) := \left(\frac{\sin(\theta - r_1(\theta))^2}{\sin(\theta + r_1(\theta))^2} + \frac{\tan(\theta - r_1(\theta))^2}{\tan(\theta + r_1(\theta))^2} \right)$$

$$r_2(\theta) := \sin^{-1} \left(\frac{n_2}{n_3} \cdot \sin(\theta) \right), \quad R_2(\theta) := \left(\frac{\sin(\theta - r_2(\theta))^2}{\sin(\theta + r_2(\theta))^2} + \frac{\tan(\theta - r_2(\theta))^2}{\tan(\theta + r_2(\theta))^2} \right)$$

$$r_3(\theta) := \sin^{-1} \left(\frac{n_3}{n_1} \cdot \sin(r_2(\theta)) \right), \quad R_3(\theta) := \left(\frac{\sin(r_2(\theta) - r_3(\theta))^2}{\sin(r_2(\theta) + r_3(\theta))^2} + \frac{\tan(r_2(\theta) - r_3(\theta))^2}{\tan(r_2(\theta) + r_3(\theta))^2} \right)$$

$$\gamma(\theta) := r_2(\theta), \quad \phi(\beta) := \sin^{-1} \left(\frac{n_2}{n_3} \cdot \sin(\beta) \right)$$

$$T_1(\theta) := 1 - R_1(\theta), \quad T_2(\theta) := 1 - R_2(\theta), \quad T_3(\theta) := 1 - R_3(\theta)$$

$$\theta_{c1} := \sin^{-1} \left(\frac{n_1}{n_2} \right), \quad \theta_{c1} = 0.545, \quad R_1(\theta_{c1}) = 1, \quad R_3(\theta_{c1}) = 1$$

$$\theta_{c2} := \sin^{-1} \left(\frac{n_3}{n_2} \right), \quad \theta_{c2} = 0.858, \quad \frac{n_1}{n_2} = 0.756$$

$$\theta_{c3} := \sin^{-1} \left(\frac{n_1}{n_3} \right), \quad \theta_{c3} = 0.755$$

Created Charge Carriers and Initial CL Intensity

- When $0 < x < R$

$$c1 = -2.163 \cdot 10^9 \text{ (cm}^{-3}\text{)}, \quad c2 = -2.565 \cdot 10^9 \text{ (cm}^{-3}\text{)}$$

$$N_1(x) := c1 \cdot \exp(m \cdot x) + c2 \cdot \exp(-m \cdot x) - \frac{C}{m} \text{ (cm}^{-3}\text{)}$$

$$N_1^{\text{tot}} := \int_0^R N_1(x) dx, \quad N_1^{\text{tot}} = 6.92 \cdot 10^4 \text{ (cm}^{-2}\text{)}$$

$$I_0^1(x) := \frac{Ee}{r} \cdot N_1(x), \quad I_0^{1,\text{tot}} := \int_0^R I_0^1(x) dx, \quad I_0^{1,\text{tot}} = 2.248 \cdot 10^{-5} \text{ (W} \cdot \text{cm}^{-2}\text{)}$$

- When $R < x < t_1$

$$c3 = 5.103 \cdot 10^8 \text{ (cm}^{-3}\text{)}, \quad c4 = 2.794 \cdot 10^9 \text{ (cm}^{-3}\text{)}$$

$$N_2(x) := c3 \cdot \exp(m \cdot x) + c4 \cdot \exp(-m \cdot x) \text{ (cm}^{-3}\text{)}$$

$$N_2^{\text{tot}} := \int_0^R N_2(x) dx, \quad N_2^{\text{tot}} = 6.92 \cdot 10^4 \text{ (cm}^{-2}\text{)}$$

$$I_0^2(x) := \frac{Ee}{r} \cdot N_2(x), \quad I_0^{2,\text{tot}} := \int_R^{t_1} I_0^2(x) dx, \quad I_0^{2,\text{tot}} = 2.087 \cdot 10^{-5} \text{ (W} \cdot \text{cm}^{-2}\text{)}$$

- Total Initial Intensity

$$I_{0_total} := I_0^{1,\text{tot}} + I_0^{2,\text{tot}}, \quad I_{0_total} = 4.335 \cdot 10^{-5} \text{ (W} \cdot \text{cm}^{-2}\text{)}$$

Intensity Calculations by Conditions

1. When $0 < x < R$

1.1. When $0 < \theta < \theta_{c1}$

- Specular Part:

$$\text{Film}_{-s}^{11}(t_1, \sigma) := \int_0^{c1} \int_0^R T F_{s-\theta}^{11}(\theta, x, t_1, \sigma) dx d\theta$$

$$\text{Film}_{-s}^{11}(500 \cdot 10^{-7}, 11.2) = 1.52 \cdot 10^{-6}$$

$$\text{Substrate}_{-s}^{11}(t_1, \sigma) := \int_0^{c1} \int_0^R T S_{s-\theta}^{11}(\theta, x, t_1, \sigma) dx d\theta$$

$$\text{Substrate}_{-s}^{11}(500 \cdot 10^{-7}, 11.2) = 1.56 \cdot 10^{-6}$$

- Diffuse Part:

1.1.1. When $0 < \beta < \theta_{c1}$

$$TF_{d_0}^{111}(\theta, x, t_1, \eta, \sigma) := \int_0^{\theta_{c1}} TF_{d_\beta}^{111}(\theta, \beta, x, t_1, \eta, \sigma) d\beta, \quad TS_{d_0}^{111}(\theta, x, t_1, \eta, \sigma) := \int_0^{\theta_{c1}} TS_{d_\beta}^{111}(\theta, \beta, x, t_1, \eta, \sigma) d\beta$$

1.1.2. When $\theta_{c1} < \beta < \theta_{c2}$

$$TF_{d_0}^{112}(\theta, x, t_1, \eta, \sigma) := 0, \quad TS_{d_0}^{112}(\theta, x, t_1, \eta, \sigma) := 0$$

1.1.3. When $\theta_{c2} < \beta < \frac{\pi}{2}$

$$TF_{d_0}^{113}(\theta, x, t_1, \eta, \sigma) := 0, \quad TS_{d_0}^{113}(\theta, x, t_1, \eta, \sigma) := 0$$

1.1.4. Diffuse Part Sum

$$\text{Film}_{-d}^{11}(t_1, \eta, \sigma) := \int_0^{\theta_{c1}} \int_0^{\pi} TF_{d_\beta}^{111}(\theta, x, t_1, \eta, \sigma) + I T_{d_{up}}^{11}(\theta, x, t_1, \eta, \sigma) + I T_{d_{down}}^{11}(\theta, x, t_1, \eta, \sigma) dx d\theta$$

$$\text{Film}_{-d}^{11}(500 \cdot 10^{-7}, 0.3, 11.2) = 1.338 \cdot 10^{-9}$$

$$\text{Substrate}_{-d}^{11}(t_1, \eta, \sigma) := \int_0^{\theta_{c1}} \int_0^{\pi} TS_{d_\beta}^{111}(\theta, x, t_1, \eta, \sigma) dx d\theta$$

$$\text{Substrate}_{-d}^{11}(500 \cdot 10^{-7}, 0.3, 11.2) = 5.198 \cdot 10^{-10}$$

1.2. When $\theta_{c1} < \theta < \theta_{c2}$

- Specular Part: zero

- Diffuse Part:

1.2.1. When $0 < \beta < \theta_{c1}$

$$TF_{d_0}^{121}(\theta, x, t_1, \eta, \sigma) := \int_0^{\theta_{c1}} TF_{d_\beta}^{121}(\theta, \beta, x, t_1, \eta, \sigma) d\beta, \quad TS_{d_0}^{121}(\theta, x, t_1, \eta, \sigma) := \int_0^{\theta_{c1}} TS_{d_\beta}^{121}(\theta, \beta, x, t_1, \eta, \sigma) d\beta$$

1.2.2. When $\theta_{c1} < \beta < \theta_{c2}$

$$TF_{d_0}^{122}(\theta, x, t_1, \eta, \sigma) := 0, \quad TS_{d_0}^{122}(\theta, x, t_1, \eta, \sigma) := 0$$

1.2.3. When $\theta_{c2} < \beta < \frac{\pi}{2}$

$$TF_{d_0}^{123}(\theta, x, t_1, \eta, \sigma) := 0, \quad TS_{d_0}^{123}(\theta, x, t_1, \eta, \sigma) := 0$$

1.2.4. Diffuse Part Sum

$$\text{Film}_{-d}^{12}(t_1, \eta, \sigma) := \int_0^{\theta_{c1}} \int_0^{\pi} TF_{d_\beta}^{121}(\theta, x, t_1, \eta, \sigma) + I T_{d_{up}}^{12}(\theta, x, t_1, \eta, \sigma) + I T_{d_{down}}^{12}(\theta, x, t_1, \eta, \sigma) dx d\theta$$

$$\text{Film}_{-d}^{12}(500 \cdot 10^{-7}, 0.3, 11.2) = 1.043 \cdot 10^{-8}$$

$$\text{Substrate}_{-d}^{12}(t_1, \eta, \sigma) := \int_0^{\theta_{c1}} \int_0^{\pi} TS_{d_\beta}^{121}(\theta, x, t_1, \eta, \sigma) dx d\theta$$

$$\text{Substrate}_{-d}^{12}(500 \cdot 10^{-7}, 0.3, 11.2) = 3.483 \cdot 10^{-9}$$

1.3. When $\theta_{c2} < \theta < \frac{\pi}{2}$

- Specular Part: zero

- Diffuse Part:

1.3.1. When $0 < \beta < \theta_{c1}$

$$TF_{d_{\theta}}^{131}(\theta, x, t_1, \eta, \sigma) := \int_0^{\theta_{c1}} TF_{d_{\beta}}^{131}(\theta, \beta, x, t_1, \eta, \sigma) d\beta, \quad TS_{d_{\theta}}^{131}(\theta, x, t_1, \eta, \sigma) := \int_0^{\theta_{c1}} TS_{d_{\beta}}^{131}(\theta, \beta, x, t_1, \eta, \sigma) d\beta$$

1.3.2. When $\theta_{c1} < \beta < \theta_{c2}$

$$TF_{d_{\theta}}^{132}(\theta, x, t_1, \eta, \sigma) := 0, \quad TS_{d_{\theta}}^{132}(\theta, x, t_1, \eta, \sigma) := 0$$

1.3.3. When $\theta_{c2} < \beta < \frac{\pi}{2}$

$$TF_{d_{\theta}}^{133}(\theta, x, t_1, \eta, \sigma) := 0, \quad TS_{d_{\theta}}^{133}(\theta, x, t_1, \eta, \sigma) := 0$$

1.3.4. Diffuse Part Sum

$$\text{Film}_{-d}^{13}(t_1, \eta, \sigma) := \int_0^{\frac{\pi}{2}} \int_0^{\theta} TF_{d_{\theta}}^{131}(\theta, x, t_1, \eta, \sigma) + IT_{d_{up}}^{13}(\theta, x, t_1, \eta, \sigma) + IT_{d_{down}}^{13}(\theta, x, t_1, \eta, \sigma) dx d\theta$$

$$\text{Film}_{-d}^{13}(500 \cdot 10^{-7}, 0.3, 11.2) = 7.195 \cdot 10^{-7}$$

$$\text{Substrate}_{-d}^{13}(t_1, \eta, \sigma) := \int_0^{\frac{\pi}{2}} \int_0^{\theta} TS_{d_{\theta}}^{131}(\theta, x, t_1, \eta, \sigma) dx d\theta$$

$$\text{Substrate}_{-d}^{13}(500 \cdot 10^{-7}, 0.3, 11.2) = 5.137 \cdot 10^{-9}$$

2. When $R < x < t_1$

2.1. When $0 < \theta < \theta_{c1}$

- Specular Part:

$$\text{Film}_{-s}^{21}(t_1, \sigma) := \int_0^{\theta_{c1}} \int_{x_R}^{t_1} TF_{s_{\theta}}^{21}(\theta, x, t_1, \sigma) dx d\theta$$

$$\text{Film}_{-s}^{21}(500 \cdot 10^{-7}, 11.2) = 1.409 \cdot 10^{-6}$$

$$\text{Substrate}_{-s}^{21}(t_1, \sigma) := \int_0^{\theta_{c1}} \int_{x_R}^{t_1} TS_{s_{\theta}}^{21}(\theta, x, t_1, \sigma) dx d\theta$$

$$\text{Substrate}_{-s}^{21}(500 \cdot 10^{-7}, 11.2) = 1.447 \cdot 10^{-6}$$

- Diffuse Part:

2.1.1. When $0 < \beta < \theta_{c1}$

$$TF_{d,\theta}^{211}(\theta, x, t_1, \eta, \sigma) := \int_0^{\theta_{c1}} TF_{d,\beta}^{211}(\theta, \beta, x, t_1, \eta, \sigma) d\beta, \quad TS_{d,\theta}^{211}(\theta, x, t_1, \eta, \sigma) := \int_0^{\theta_{c1}} TS_{d,\beta}^{211}(\theta, \beta, x, t_1, \eta, \sigma) d\beta$$

2.1.2. When $\theta_{c1} < \beta < \theta_{c2}$

$$TF_{d,\theta}^{212}(\theta, x, t_1, \eta, \sigma) := 0, \quad TS_{d,\theta}^{212}(\theta, x, t_1, \eta, \sigma) := 0$$

2.1.3. When $\theta_{c2} < \beta < \frac{\pi}{2}$

$$TF_{d,\theta}^{213}(\theta, x, t_1, \eta, \sigma) := 0, \quad TS_{d,\theta}^{213}(\theta, x, t_1, \eta, \sigma) := 0$$

2.1.4. Diffuse Part Sum

$$Film_{-d}^{21}(t_1, \eta, \sigma) := \int_0^{\theta_{c1}} \int_0^{\pi/2} TF_{d,\theta}^{211}(\theta, x, t_1, \eta, \sigma) + I T_{d_up}^{21}(\theta, x, t_1, \eta, \sigma) + I T_{d_down}^{21}(\theta, x, t_1, \eta, \sigma) dx d\theta$$

$$Film_{-d}^{21}(500 \cdot 10^{-7}, 0.3, 11.2) = 1.241 \cdot 10^{-9}$$

$$Substrate_{-d}^{21}(t_1, \eta, \sigma) := \int_0^{\theta_{c1}} \int_0^{\pi/2} TS_{d,\theta}^{211}(\theta, x, t_1, \eta, \sigma) dx d\theta$$

$$Substrate_{-d}^{21}(500 \cdot 10^{-7}, 0.3, 11.2) = 4.819 \cdot 10^{-10}$$

2.2. When $\theta_{c1} < \theta < \theta_{c2}$

- Specular Part: zero

- Diffuse Part:

2.2.1. When $0 < \beta < \theta_{c1}$

$$TF_{d,\theta}^{221}(\theta, x, t_1, \eta, \sigma) := \int_0^{\theta_{c1}} TF_{d,\beta}^{221}(\theta, \beta, x, t_1, \eta, \sigma) d\beta, \quad TS_{d,\theta}^{221}(\theta, x, t_1, \eta, \sigma) := \int_0^{\theta_{c1}} TS_{d,\beta}^{221}(\theta, \beta, x, t_1, \eta, \sigma) d\beta$$

2.2.2. When $\theta_{c1} < \beta < \theta_{c2}$

$$TF_{d,\theta}^{222}(\theta, x, t_1, \eta, \sigma) := 0, \quad TS_{d,\theta}^{222}(\theta, x, t_1, \eta, \sigma) := 0$$

2.2.3. When $\theta_{c2} < \beta < \frac{\pi}{2}$

$$TF_{d,\theta}^{223}(\theta, x, t_1, \eta, \sigma) := 0, \quad TS_{d,\theta}^{223}(\theta, x, t_1, \eta, \sigma) := 0$$

2.2.4. Diffuse Part Sum

$$Film_{-d}^{22}(t_1, \eta, \sigma) := \int_0^{\theta_{c1}} \int_0^{\pi/2} TF_{d,\theta}^{221}(\theta, x, t_1, \eta, \sigma) + I T_{d_up}^{22}(\theta, x, t_1, \eta, \sigma) + I T_{d_down}^{22}(\theta, x, t_1, \eta, \sigma) dx d\theta$$

$$Film_{-d}^{22}(500 \cdot 10^{-7}, 0.3, 11.2) = 9.669 \cdot 10^{-9}$$

$$Substrate_{-d}^{22}(t_1, \eta, \sigma) := \int_0^{\theta_{c1}} \int_0^{\pi/2} TS_{d,\theta}^{221}(\theta, x, t_1, \eta, \sigma) dx d\theta$$

$$Substrate_{-d}^{22}(500 \cdot 10^{-7}, 0.3, 11.2) = 3.229 \cdot 10^{-9}$$

2.3. When $\theta_{e2} < \theta < \frac{\pi}{2}$

- Specular Part: zero

- Diffuse Part:

2.3.1. When $0 < \beta < \theta_{e1}$

$$TF_{d_{\theta}}^{231}(\theta, x, t_1, \eta, \sigma) := \int_0^{\theta_{e1}} TF_{d_{\beta}}^{231}(\theta, \beta, x, t_1, \eta, \sigma) d\beta, \quad TS_{d_{\theta}}^{231}(\theta, x, t_1, \eta, \sigma) := \int_0^{\theta_{e1}} TS_{d_{\beta}}^{231}(\theta, \beta, x, t_1, \eta, \sigma) d\beta$$

2.3.2. When $\theta_{e1} < \beta < \theta_{e2}$

$$TF_{d_{\theta}}^{232}(\theta, x, t_1, \eta, \sigma) := 0, \quad TS_{d_{\theta}}^{232}(\theta, x, t_1, \eta, \sigma) := 0$$

2.3.3. When $\theta_{e2} < \beta < \frac{\pi}{2}$

$$TF_{d_{\theta}}^{233}(\theta, x, t_1, \eta, \sigma) := 0, \quad TS_{d_{\theta}}^{233}(\theta, x, t_1, \eta, \sigma) := 0$$

2.3.4. Diffuse Part Sum

$$\text{Film}_{-d}^{23}(t_1, \eta, \sigma) := \int_{t_c}^{\pi} \int_0^{\theta_{e1}} TF_{d_{\theta}}^{231}(\theta, x, t_1, \eta, \sigma) + IT_{d_{-up}}^{23}(\theta, x, t_1, \eta, \sigma) + IT_{d_{-down}}^{23}(\theta, x, t_1, \eta, \sigma) dx d\theta$$

$$\text{Film}_{-d}^{23}(500 \cdot 10^{-7}, 0.3, 11.2) = 6.68 \cdot 10^{-7}$$

$$\text{Substrate}_{-d}^{23}(t_1, \eta, \sigma) := \int_{t_c}^{\pi} \int_0^{\theta_{e1}} TS_{d_{\theta}}^{231}(\theta, x, t_1, \eta, \sigma) dx d\theta$$

$$\text{Substrate}_{-d}^{23}(500 \cdot 10^{-7}, 0.3, 11.2) = 4.769 \cdot 10^{-9}$$

3. Final Sum Intensity

3.1. Specular Part Sum

$$\text{Film}_s(t_i, \sigma) := \text{Film}_s^{11} + \text{Film}_s^{21}$$

$$\text{Film}_s(500 \cdot 10^{-7}, 11.2) = 2.927 \cdot 10^{-6} \quad (\text{W})$$

$$\text{Substrate}_s(t_i, \sigma) := \text{Substrate}_s^{11} + \text{Substrate}_s^{21}$$

$$\text{Substrate}_s(500 \cdot 10^{-7}, 11.2) = 3.003 \cdot 10^{-6} \quad (\text{W})$$

3.2. Diffuse Part Sum

$$\text{Film}_d(t_i, \eta, \sigma) := \text{Film}_d^{11} + \text{Film}_d^{12} + \text{Film}_d^{13} + \text{Film}_d^{21} + \text{Film}_d^{22} + \text{Film}_d^{23}$$

$$\text{Film}_d(500 \cdot 10^{-7}, 0.3, 11.2) = 1.41 \cdot 10^{-6} \quad (\text{W})$$

$$\begin{aligned} \text{Substrate}_d(t_i, \eta, \sigma) := & \text{Substrate}_d^{11} + \text{Substrate}_d^{12} + \text{Substrate}_d^{13} \\ & + \text{Substrate}_d^{21} + \text{Substrate}_d^{22} + \text{Substrate}_d^{23} \end{aligned}$$

$$\text{Substrate}_d(500 \cdot 10^{-7}, 0.3, 11.2) = 1.762 \cdot 10^{-6} \quad (\text{W})$$

3.3. Light Output (Specular+Diffuse)

- Reflection Mode (Film Side)

$$I_{\text{refl}} := \text{Film}_s(t_i, \sigma) + \text{Film}_d(t_i, \eta, \sigma), \quad I_{\text{refl}} = 4.337 \cdot 10^{-6} \quad (\text{W})$$

- Transmission Mode (Substrate Side)

$$I_{\text{trans}} := \text{Substrate}_s(t_i, \sigma) + \text{Substrate}_d(t_i, \eta, \sigma), \quad I_{\text{trans}} = 3.021 \cdot 10^{-6} \quad (\text{W})$$

REFERENCES

- And70 R. C. Anderson. *Refractory materials*, edited by A. M. Alper. Academic, New York, 1 (1970).
- Bar97 M. W. Barsoum. *Fundamentals of ceramics*. McGraw-Hill, Singapore, 69 (1997).
- Bat94 C. E. Batten, K. G. Brown, and B. W. Lewis. NASA Technical Memorandum 4612, Dec. (1994).
- Bec63 P. Beckmann and A. Spizzichino. *The scattering of electromagnetic waves from rough surfaces*. Pergamon, Oxford (1963).
- Ben61 H. E. Bennett and J. O. Porteus. J. Opt. Soc. Amer. **51** (2), 123 (1961).
- Ben91 E. L. Benitez, D. E. Husk, S. E. Schnatterly, and C. Tarrío. J. Appl. Phys. **70** (6), 3256 (1991).
- Bil72 B. H. Billings. *American institute of physics handbook*, edited by D. E. Gray. McGraw-Hill, New York, 6-7 (1972).
- Bla94 G. Blasse and B. C. Grabmaier. *Luminescent materials*, Springer-Verlag, Berlin (1994).
- Bor63 H. J. Borchardt. J. Chem. Phys. **39**, 504 (1963).
- Bou99 S. Boughaba, M. U. Islam, J. A. Greer, and M. Tabat. Vacuum & Thin Film **2** (10), 14 (1999).
- Bri89 L. H. Brixner and G. Blasse. J. Electrochem. Soc. **136** (11), 3529 (1989).
- Bro93 J. A. C. Broekaert. *Glow discharge spectroscopies*, edited by R. K. Marcus. Plenum, New York, 113-174 (1993).

- Car66 W. N. Carr. *Infrared Physics* **6**, 1 (1966).
- Cha64 N. C. Chang and J. B. Gruber. *J. Chem. Phys.* **41** (10), 3227 (1964).
- Chi94 C. Chinnock. *Laser Focus World*. March, 47 (1994).
- Cho97a K. G. Cho, D. Kumar, D. G. Lee, S. L. Jones, P. H. Holloway, and R. K. Singh. *Appl. Phys. Lett.* **71** (23), 3335 (1997).
- Cho97b K. G. Cho, D. Kumar, S. L. Jones, D. G. Lee, P. H. Holloway, and R. K. Singh. *J. Electrochem. Soc.* **145**, 3456 (1998).
- Cho98a K. G. Cho, D. Kumar, D. G. Lee, P. H. Holloway, and R. K. Singh. *Flat panel display materials 1998*, edited by G. N. Parsons, C. C. Tsai, T. S. Fahlen, and C. H. Seager. *MRS Symp. Proc.* **508**, 301 (1998).
- Cho98b K. G. Cho, D. Kumar, P. H. Holloway, and R. K. Singh. *Appl. Phys. Lett.* **73** (21), 3058 (1998).
- Cho98c K. G. Cho, D. Kumar, P. H. Holloway, and R. K. Singh. *Advances in laser ablation of materials 1998*, edited by R. K. Singh, D. H. Lowndes, D. B. Chrisey, J. Narayan, T. Kawai, and E. Fogarass. *MRS Symp. Proc.* **526**, 317 (1998).
- Cho99 K. G. Cho, D. Kumar, Z. Chen, P. H. Holloway, and R. K. Singh. *Flat panel displays and sensors (principles, materials, and processes) 1999*, edited by F.R. Libsch, B. Chalamala, R. Friend, T. Jackson, and H. Ohshima. *MRS Symp. Proc.* **558**, Spring meeting (1999).
- Chr94 D. B. Chrisey and G. K. Hubler. *Pulsed laser deposiiton*. Wiley, New York (1994).
- Cou96 F. Courreges. *Information Display* **12**, 10 (1996).
- Cra98 V. Craciun, D. Craciun, and I. W. Boyd. *Electr. Lett.* **34** (15), 1527 (1998).

- Daa94 J. L. Daams, P. Villars, and J. H. N. van Vucht. *Atlas of crystal structure types for intermetallic phases*. ASM International, Materials Park, OH, 6706 (1994).
- Dex79 J. Dexpert-Ghys and M. Faucher. *Phys. Rev. B* **20** (1), 11 (1979).
- Dij87 D. Dijkkamp, T. Venkatesan, X. D. Wu, S. A. Shaheen, N. Jisrawi, Y. H. Minlee, W. L. Mclean, and M. Croft. *App. Phys. Lett.* **51**, 619 (1987).
- Duc94 S. J. Duclos, C. D. Greskovich, and O'Clair, C. R. *Scintillators and phosphor materials*, edited by M. J. Weber, P. Lecoq, R. C. Ruchti, C. Woody, W. M. Yen, and R. Y. Zhu. *MRS Symp. Proc.* **348**, 503 (1994).
- Dup 95 A. Duparre. *Handbook of optical properties Vol 1*, edited by R. E. Hummel and K. H. Guenther. CRC, Boca Raton, FL, 273-303 (1995).
- Fan40 U. Fano. *Phys. Rev.* **58**, 544 (1940).
- Fit98 J. M. Fitz-Gerald, T. A. Trottier, R. K. Singh, and P. H. Holloway. *Appl. Phys. Lett.* **72** (15), 1838 (1998).
- For69 H. Forest and G. Ban. *J. Electrochem. Soc.* **116** (4), 474 (1969).
- Fuk89 H. Fukumoto, T. Imura, and Y. Osaka. *Appl. Phys. Lett.* **55** (4), 360 (1989).
- Gao99 H-J. Gao, D.Kumar, K. G. Cho, P. H. Holloway, R. K. Singh, X. D. Fan, Y. Yan, and S. J. Pennycook. *Appl. Phys. Lett.* **75** (15), 2223 (1999).
- Geo94 D. B. Geohegan. *Pulsed laser deposition of thin films*, edited by D. B. Chrisey and G. K. Hubler. Wiley, New York, 115-165 (1994).
- Gol92 J. I. Goldstein, D. E. Newbury, P. Echlin, D. C. Joy, A. D. Romig, Jr., C. E. Lyman, C. Fiori, and E. Lifshin. *Scanning electron microscopy and X-ray microanalysis*. Plenum, New York, 89 (1992).

- Gre94 S. M. Green, A. Pique, K. S. Harshavardhan, and J. S. Bernstein. *Pulsed laser deposition*, edited by D. B. Chrisey and G. K. Hubler. Wiley, New York, 23 (1994).
- Gre95 J. A. Greer and M. D. Tabat. J. Vac. Sci. Technol. A **13** (3), 1175 (1995).
- Has90 T. Hase, T. Kano, E. Nakazawa, and H. Yamamoto. *Advances in electronics and electron physics*, edited by P. W. Hawkes. Academic, New York, 135 (1990).
- Hec92 J. Hecht. Laser Focus World (June), 63 (1992).
- Her70 H. N. Hersh and H. Forest. J. Luminescence **1-2**, 862 (1970).
- Hir97 G. A. Hirata, J. Mckittrick, M. Avalos-Borja, J. M. Siqueiros, and D. Devlin. Appl. Surf. Sci. **113/114**, 509 (1997).
- Hol99 P. H. Holloway, T. A. Trottier, B. Abrams, C. Kondoleon, S. L. Jones, J. S. Sebastian, W. J. Thomas, and H. Swart. J. Vac. Sci. Technol. B **17**(2), 758 (1999).
- Hu 92 J. Hu and R. G. Gordon. J. Appl. Phys. **71** (2), 880 (1992).
- Jac96 S. M. Jacobsen, C. Stoffers, S. Yang, and C. J. Summers. *Low voltage phosphor data sheets*. PTCOE, Atlanta, GA, 3 (1996).
- Jol90 F. Jollet, C. Noguera, N. Thromat, M. Gautier, and J. P. Duraud. Phys. Rev. B **42** (12), 7587 (1990).
- Jon97a S. L. Jones, D. Kumar, R.K. Singh, and P.H. Holloway. Appl. Phys. Lett. **71** (3), 404 (1997).
- Jon97b S. L. Jones, D. Kumar, R. K. Singh, and P. H. Holloway. *Flat Panel Display Materials III*, edited by R. T. Fulks, G.N. Parsons, D.E. Slobod, and T. H. Yuzuriha. MRS Symp. Proc. **471**, 299 (1997).
- Jon99 S. L. Jones, D. Kumar, K. G. Cho, R. K. Singh, and P. H. Holloway. Displays **19**, 151 (1997).

- Kam98 S. Kamiya and H. Mizuno, *Phosphor handbook*, edited by S. Shionoya and W. M. Yen. CRC, Boca Raton, FL, 389-444 (1998).
- Kim97 J. M. Kim, J. P. Hong, J. W. Kim, J. H. Choi, N. S. Park, J. H. Kang, J. E. Jang, Y. S. Ryu, H. C. Yang, B. I. Gorfinkel, and E. V. Roussina. *J. Vac. Sci. Technol. B* **15** (2), 528 (1997).
- Kim98 J. M. Kim, J. P. Hong, J. H. Choi, Y. S. Ryu, and S. S. Hong. *J. Vac. Sci. Technol. B* **16** (2), 736 (1998).
- Kim99 J. M. Kim, H. W. Lee, Y. S. Choi, J. E. Jung, N. S. Lee, Y. W. Jin, and N. S. Park. *J. Vac. Sci. Technol. B* **17** (2), 744 (1999).
- Kla87 D. B. M. Klaassen, D. M. de Leeuw, and T. J. Welker. *J. Luminescence*. **37**, 21 (1987).
- Kom96 H. Kominami, K. Horikawa, T. Auki, T. Nakamura, Y. Nakanishi, and Y. Hatanaka. *Proc. 15th Int. Display Res. Conf.*, 867 (1996).
- Kor99 Ed Korczynski. *Solid State Technology* (January), 51 (1999).
- Kum93 D. Kumar, M. Sharon, R. Pinto, P. R. Apte, S. P. Pai, S. C. Purandare, L. C. Gupta, and R. Vijayaraghavan. *Appl. Phys. Lett.* **62**, 3522 (1993).
- Kum99a D. Kumar, K. G. Cho, Z. Chen, P.H. Holloway, and R. K. Singh. *Phys. Rev. B* **60** (19), 13331 (1999).
- Kum99b D. Kumar, K. G. Cho, P.H. Holloway, and R. K. Singh, *Multicomponent Oxide Films for Electronics 1999*, edited by M. E. Hawley, D. H. Blank, C.-B. Eom, S. K. Streiffer, and D. G. Schlom. *MRS Symp. Proc.* **574**, 11 (1999).
- Kuo97 H. P. Kuo, S. F. Burriesci, J. Lin, and D. J. Miller. *J. Vac. Sci. Technol. B* **15** (6), 2782 (1997).
- Lee97 D. G. Lee and R. K. Singh, *Appl. Phys. Lett.* **70**, 1542 (1997).

- Lee98a D. G. Lee. Ph.D. Dissertation, University of Florida, Gainesville (1997).
- Lee98b Song Jae Lee. Jpn. J. Appl. Phys. **37**, 509 (1998).
- Low96 D. H. Lowndes, D. B. Geohegan, A. A. Puretzky, D. P. Norton, and C. M. Rouleau. Science **273**, 898 (1996).
- Mac84 R. Mach and G. O. Muller. Phys. Status Solidi A **81**, 609 (1984).
- Mae92 P. Maestro, D. Huguenin, A. Seigneurin, F. Deneuve, P. L. Lam, and J. F. Berar. J. Electrochem. Soc. **139** (5), 1479 (1992).
- Mar88 D. J. Marshall. *Cathodoluminescence of geological materials*. Unwin Hyman, Boston, 1-16 (1988).
- May90 J. W. Mayer and S. S. Lau. *Electronic materials science: For integrated circuits in Si and GaAs*. Macmillan, New York, 96 (1990).
- Mor98 K. Morimoto. *Phosphor handbook*, edited by S. Shionoya and W. M. Yen. CRC, Boca Raton, FL, 561-580 (1998).
- Myh98 S. Myhajlenko. *Luminescence of Solids*, edited by D. R. Vij. Plenum, New York, 135 (1998).
- Off95 Office of Technology Assessment, U.S. Congress. *Flat panel displays in perspective*, OTA-ITC-631. U.S. Government Printing Office, Washington, DC, September (1995).
- Ohn98 K. Ohno. *Phosphor handbook*, edited by S. Shionoya and W. M. Yen. CRC, Boca Raton, FL, 489-498 (1998).
- Oku98 M. Okuda, S. Matsutani, A. Asai, A. Yamano, and K. Hatanaka. SID98, Tech. Deg. **14** (1), 185 (1998).
- Oni90 K. I. Onisawa, M. Fuyama, K. Tamura, K. Taguchi, T. Nakayama, and Y. A. Ono. J. Appl. Phys. **68** (2), 719 (1990).
- Oza90 L. Ozawa, *Cathodoluminescence: Theory and applications*. VCH, New York (1990).

- Pap85 R. G. Pappalardo and R. B. Hunt, Jr. J. Electrochem. Soc. **132** (3), 721 (1985).
- Pat65 M. G. Paten and E. N. Maslen. Acta. Crystallogr. **19**, 307 (1965).
- Pet95 T. Petrovich. Electronic Design. January 9, 95 (1995).
- Pfa61 A. Pfahnl. *Advances in electron tube techniques*, Pergamon, New York, 204 (1961).
- Pie98 S. V. Pietambaram, D. Kumar, R. K. Singh, and C. B. Lee. Phys. Rev. B **58** (13), 8182 (1998).
- Pin64 D. Pines. *Elementary excitation in solids*. Benjamin, New York (1964).
- Pol93 D. D. Pollock. *Physical properties of materials for engineers* (2nd ed.). CRC, Boca Raton, FL, 269-315 (1993).
- Rao96a R. P. Rao. J. Electrochem. Soc. **143** (1), 189 (1996).
- Rao96b R. P. Rao. Solid State Communications **99** (6), 439 (1996).
- Ras96 C. E. Rash and E. McGowin III. Information Display **12** (8), 26 (1996).
- Rie 70 E. P. Riedel. J. Luminescence **1-2**, 176 (1970).
- Rin95 A. G. Rinzler, J. H. Hafner, P. Nikolaev, L. Lou, S. G. Kim, D. Tomanek, P. Nordlander, D. T. Colbert, and R. E. Smalley. Science **269**, 1550 (1995).
- Ron94 C. R. Ronda, H. Bechtel, U. Kynast, and T. Welker. J. Appl. Phys. **75** (9), 4636 (1994).
- Roo94 A. Roos and D. Ronnow. Applied Optics **33** (34), 7908 (1994).
- Rop67 R. C. Ropp. J. Opt. Soc. Amer. **57**, 213 (1967).
- Sch92 W. V. Schaik and G. Blasse. Chem. Mater. **4** (2), 410 (1992).

- Sch93 I. Schnitzer and E. Yablonovitch, *Appl. Phys. Lett.* **63** (16), 2174 (1993).
- Sea97 C. H. Seager, W. L. Warren, and D. R. Tallant. *J. Appl. Phys.* **81** (12), 7994 (1997).
- She98 L. E. Shea. *Interface* **7** (2), 24 (1998).
- Sho98 S. Schkhovets, R. Goldhahn, V. Cimalla, T. S. Cheng, and C. T. Foxon. *J. Appl. Phys.* **84** (3), 1561 (1998).
- Sin90 R. K. Singh and J. Narayan. *Phys. Rev. B* **41** (13), 8843 (1990).
- Sin98 R. K. Singh and D. Kumar. *Mat. Sci. Engineering* **R22** (4), 113 (1998).
- Smi65 H. M. Smith and A. F. Turner. *Appl. Opt.* **4**, 147 (1965).
- Smi98 R. T. Smith. *Information Display* 2/98, 12 (1998).
- Sri99 A. Srivastava, V. Cracium, J. M. Howard, and R. K. Singh. *Appl. Phys. Lett.* **75** (19), 3002 (1999).
- Swa96 H. C. Swart, J. S. Sebaschian, T. A. Trottier, S. L. Jones, and P. H. Holloway. *J. Vac. Sci. Tech.* **A13**, 1697 (1996).
- Swa99 H. C. Swart, A. P. Greeff, P. H. Holloway, G. L. and P. Berning. *Appl. Surf. Sci.* **140** (1-2), 63 (1999).
- Sze81 S. M. Sze. *Physics of semiconductor devices*. Wiley, New York, 7-60 (1981).
- Tan85 L. E. Tannas, Jr. *Flat panel displays and CRTs*. Van Nostrand Reinhold, New York (1985).
- Tan98 S. Tanimizu, *Phosphor handbook*, edited by S. Shionoya and W. M. Yen. CRC, Boca Raton, FL, 141-200 (1998).
- The85 D. Theis and R. Wengert. *J. Electrochem. Soc.* **132** (10), 2507 (1985).

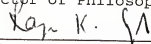
- Top79 A. S. Toporetz. Sov. J. Opt. Technol. **46** (1), 35 (1979).
- Tro91 W. J. Tropf and M. E. Thomas. *Handbook of optical constants of solids II*. Academic, New York, 1079 (1991).
- Tro96 T. A. Trottier, H. C. Swart, S. L Jones, J. S. Sebastian, and P. H. Holloway. J. SID 4/4, 351 (1996).
- Tro97 T. A. Trottier. Ph.D. Dissertation, University of Florida (1997).
- Uem98 S. Uemura, T. Nagasako, J. Yotani, and T. Shimojo. SID98 Tech. Dig. **39**, 1052 (1998).
- Ura80 K. Urabe. Jpn. J. Appl. Phys. **19**, 885 (1980).
- Vec99 A. Vecht, C. Gibbons, D. Davies, X. Jing, P. Marsh, T. Ireland, J. Silver, A. Newport, and D. Barber. J. Vac. Sci. Technol. B **17**(2), 750 (1999).
- Wal88 P. M. B. Walker. *Chambers science and technology dictionary*. Chambers & Cambridge University Press, Cambridge, 141 (1988).
- Wes90 G. A. West and K. W. Beeson. J. Mater. Res. **5** (7), 1573 (1990).
- Wei98 B. L. Weiss, A. Badzian, L. Pilione, T. Badzian, and W. Drawl. J. Vac. Sci. Tech. B **16**, 681 (1998).
- Wic64 K. A. Wickersheim and R. A. Lefever. J. Electrochem. Soc. **111**(1), 47 (1964).
- Wil90 C. Wild, N. Herres, and P. Koidl. J. Appl. Phys. **68** (3), 973 (1990).
- Wil93 C. Wild, P. Koidl, W. Muller-Sebert, H. Walcher, R. Kohl, N. Herres, R. Rocher, R. Samlenski, and R. Brenn. *Diamond and Related Mater.* **2**, 158 (1993).
- Xu 95 Xianfan Xu. J. Appl. Phys. **77** (12), 6715 (1995).

- Yac90 B. G. Yacobi and D. B. Holt. *Cathodoluminescence microscopy of inorganic solids*. Plenum, New York, 1 (1990).
- Yam98 H. Yamamoto. *Phosphor handbook*, edited by S. Shionoya and W. M. Yen. CRC, Boca Raton, FL, 113-121 (1998).
- Yoo97 J. S. Yoo and J. D. Lee. *J. Appl. Phys.* **81** (6), 2810 (1997).
- Yos98 T. Yoshioka and M. Ogawa. *Phosphor handbook*, edited by S. Shionoya and W. M. Yen. CRC, Boca Raton, 683-726 (1998).

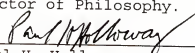
BIOGRAPHICAL SKETCH

Kyu-Gong Cho was born on February 10, 1963, in Bu-Yeo, Korea. He moved to Seoul, the capital of Korea, when he was 5 years old, and grew up there. He received his bachelor of arts degree from Korea Military Academy and became a second lieutenant in the Army of the Republic of Korea in March 1986. He served in the army as a platoon leader and an ammunition management officer for three years after graduation. He then entered graduate school at the University of Surrey (Guildford, U.K.) in October 1989, and completed his master of science degree in materials in November 1991. He continued his service in the army until July, 1996 as the ordnance company commander and the ammunition officer of the 1st Division of the army, followed by duties as a K-1 tank maintenance instructor and computer-based training program development officer of the Technical School of the army. He moved to the University of Florida, Gainesville, Florida, in the fall of 1996 to begin his studies for the degree of doctor of philosophy in the field of materials science and engineering with specializations in electronic materials.

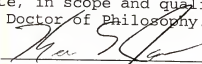
I certify that I have read this study and that in my opinion it conforms to acceptable standards of scholarly presentation and is fully adequate, in scope and quality, as a dissertation for the degree of Doctor of Philosophy.


Rajiv K. Singh, Chair
Professor of Materials
Science and Engineering

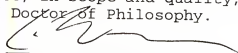
I certify that I have read this study and that in my opinion it conforms to acceptable standards of scholarly presentation and is fully adequate, in scope and quality, as a dissertation for the degree of Doctor of Philosophy.


Paul H. Holloway
Professor of Materials
Science and Engineering

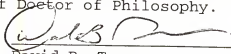
I certify that I have read this study and that in my opinion it conforms to acceptable standards of scholarly presentation and is fully adequate, in scope and quality, as a dissertation for the degree of Doctor of Philosophy.


Kevin S. Jones
Professor of Materials
Science and Engineering

I certify that I have read this study and that in my opinion it conforms to acceptable standards of scholarly presentation and is fully adequate, in scope and quality, as a dissertation for the degree of Doctor of Philosophy.


Eric D. Wachsman
Associate Professor of
Materials Science and
Engineering


I certify that I have read this study and that in my opinion it conforms to acceptable standards of scholarly presentation and is fully adequate, in scope and quality, as a dissertation for the degree of Doctor of Philosophy.


David B. Tanner
Professor of Physics

This dissertation was submitted to the Graduate Faculty of the College of Engineering and to the Graduate School and was accepted as partial fulfillment of the requirements for the degree of Doctor of Philosophy.

May 2000

fr


M. Jack Ohanian
Dean, College of Engineering

Winfred M. Phillips
Dean, Graduate School